IMPLEMENTATION AND VALIDATION OF A COMPUTATIONAL MODEL OF THE FELINE FORELIMB

A Dissertation
Presented to
The Academic Faculty

by

Ramaldo S. Martin

In Partial Fulfillment
of the Requirements for the Degree
Doctor of Philosophy in the
School of Electrical and Computer Engineering

Georgia Institute of Technology

December 2013

IMPLEMENTATION AND VALIDATION OF A COMPUTATIONAL MODEL OF THE FELINE FORELIMB

Approved by:

Dr. T. Richard Nichols, Advisor
School of Applied Physiology
Georgia Institute of Technology

Dr. Patricio Vela
School of Electrical and Computer Engineering
Georgia Institute of Technology

Dr. Thomas Burkholder
School of Applied Physiology
Georgia Institute of Technology

Dr. Magnus Egerstedt
School of Electrical and Computer Engineering
Georgia Institute of Technology

Dr. Lena Ting
Department of Biomedical Engineering
Georgia Institute of Technology

Dr. Pamela Bhatti
School of Electrical and Computer Engineering
Georgia Institute of Technology

Date approved: September 19, 2013

ACKNOWLEDGEMENTS

I would first like to thank my family for supporting me from afar all throughout my time here in the US. I would like to thank my lab-mates during my time here - Chris, Irrum, Gareth, Mark, Claire, Victoria, and Inez for helping me with experiments and the presentation of my work. I especially thank Dr. Nate Bunderson for the Neuromechanic platform and model, without which this work would not have been possible. Thank you Bill Goolsby for doing a top-notch job setting up the equipment, particularly the robotic arms. I would like Dr. Thomas Burkholder for allowing me the use of his lab, doing me the great favor of sharing his scientific knowledge and invaluable critiques, and essentially being a second co-advisor. I would like to thank Dr. Patricio Vela for agreeing to be my ECE co-advisor, and Dr. Lena Ting, Dr. Magnus Egerstedt, and Dr. Pamela Bhatti for taking of your valuable time to be on my committee and read my thesis. Last, but certainly not least, I would like to thank my advisor Dr. Richard Nichols for welcoming me into his lab (again), and always being ready to discuss and give me precious advice as I progressed through my research. You have done far more for me than you know.

TABLE OF CONTENTS

LIST OF TABLES

LIST OF FIGURES

SUMMARY

Postural control incorporates multiple neural and mechanical systems at various levels of the motor control system, yet the question of how all these systems interact remains unanswered. This dissertation describes development of a biologically based, three-dimensional mathematical model of the forelimb of the domestic cat that integrates skeletal anatomy, muscular architecture, and neural control. Previous work has shown that muscle architecture profoundly affects its function. However, even though the forelimbs of quadrupeds contribute to posture and locomotion differently from hindlimbs, most models of quadruped motion are based upon hindlimb mechanics. The proposed work consists of three main steps: (1) architectural and anatomical characterization, which involves acquisition of muscle attachment data, measurement of whole muscle and muscle fiber properties, and estimation of limb kinematic parameters; (2) model development and implementation, wherein the data will be integrated into a mathematical model using special-purpose software; and (3) model validation, including verification of model estimates against experimentally obtained measurements of muscle moment arms, and prediction of limb kinetics, namely end-point forces arising from perturbations to the limb. It was found that the forelimb does indeed possess structure, particularly at the shoulder and antebrachium, that allows for more diverse movements. The neural wiring in these regions is more complex than in the hindlimb, and there exists substantial muscular structure in place for non-sagittal motion and object suppression and retrieval. Other results showed that the kinematics of the limb alone produce a restorative response to postural disturbance but that the magnitude is reduced, indicating that neural input acts

as a modulatory influence on top of the intrinsic mechanism of limb architecture. Furthermore the model demonstrated many of the essential features found in the experiments. This study represents the implementation of the first forelimb model of the cat incorporating mechanical properties and serves as a key component of a full quadruped model to explore posture and locomotion.

CHAPTER 1

1.1 Introduction

The ability to stand, walk, and carry out the various other motor tasks of daily life requires the stabilization of the body's center of mass in the face of self-imposed and external perturbations, that is, the maintenance of posture. The study of postural control, specifically how the neuromusculoskeletal system is able to accomplish this task, has the ability to transform many lives and areas of research. In the United States alone there are close to 2 million people living with amputations, mostly due to vascular disease and trauma. Progress in limb replacement technology is hampered by the fact that individuals lack sensation distal to the amputation, thereby hindering their ability to maintain posture. Movement disorders, including Parkinson's disease and dystonia can severely impair balance and coordination and has a debilitating effect on individuals' quality of life. Balance control in robotics is a thriving area of research mainly for its application in mobility over uneven terrain in inhospitable environments. Understanding of motor function, and more specifically postural control, is essential to addressing the issues in each of these areas.

Within nature, structure has been shown to be closely related to function, whether it be at the level of cells, tissues or organs. In order to study this structure-function relationship and motor control many groups have used the domestic cat as the standard model [1-10]. Within this model, however, most research has focused on the hindlimb, even to the extent that essentially four hindlimbs [11, 12], or struts [13] for forelimbs are used in research. This does not help us fully understand how the neuromusculoskeletal system operates, especially in light of the fact that the forelimb has a greater functional

repertoire than the hindlimb (including turning, prey capture and manipulation). In fact, it has been shown that cats use a somewhat different postural strategy in the forelimbs from the hindlimbs in the horizontal plane [4, 8, 9, 14]. In addition, during locomotion, the forelimb uses 11 muscle synergies to the hindlimb's 7 [6]. Furthermore, the forelimb has more complex neural wiring across the shoulder and wrist that span anatomical groups [5, 15]. Therefore, in order to study the wider repertoire of motor behavior, the forelimb is of equal or greater importance. Thus, it is imperative that an examination be made of the structural aspects of forelimb and how they relate to functional ones.

To be able to tease apart the various aspects of motor behavior, a musculoskeletal model of the forelimb was be constructed. Models are useful (i) to conduct experiments which are too difficult, costly, or unethical to carry out directly; (ii) to be able to reduce the number of animal experiments, and (iii) to design suitable biological experiments and to rule out inappropriate ones. To determine model accuracy, calibration and testing against experimentally derived parameters or outcome was be required. **Thus, the objective of this research was to implement, parameterize and experimentally validate the first physiologically based, mathematical model of the cat forelimb as a first step in studying motor function.**

The milestones, as well as a summary of what each entailed, were as follows:

1. **Architectural and anatomical characterization**

   - Acquisition of muscle attachment data
   - Measurement of whole muscle and muscle fiber properties
   - Estimation of limb kinematic parameters

2. **Model development and implementation**

   - Integration of physiological data into a mathematical model using special-purpose software.

3. **Model validation**

   - Verification of model estimates against experimentally obtained measurements of passive limb properties (i.e. muscle moment arms).

   - Prediction of limb kinetics, namely end-point forces arising from perturbations to the limb.

1.2 Origin and History of the Problem

Motor behavior depends on proper control of the musculoskeletal system. This depends not only on the anatomical attributes of the skeletal and musculotendon complex, but also on the interaction of these structures via neural pathways with various systems, including those of the somatosensory, namely proprioceptive and cutaneous signals [16-18], vestibular [19], and visual [20]. The level of involvement of each of these systems in motor control is less clear. Some researchers have claimed involvement of supraspinal control subsuming those of mechanical and reflex [21-23], and others have reported that postural regulation receives contributions from spinal circuits [4, 24]. As a means of exploring the underlying mechanisms of the separate roles of these systems in motor function, musculoskeletal modeling and mechanical analysis techniques can have been applied [25-30]. Models, which require knowledge of musculotendon anatomy and

contraction dynamics [31-34], allow one to more closely examine the various relationships among, and actions of, the diverse systems in carrying out motor tasks.

1.2.1 Neural pathways and muscle receptors

Motor behavior depends on a complex interaction of limb anatomy, visual, vestibular, somatosensory and supraspinal systems [20]. Within the realm of postural studies, substantial research has been carried out to determine the influence of each of these systems. In a seminal experiment, intact cats were trained to stand quietly on a platform while the surface was shifted in multiple directions in the horizontal plane [8, 9]. The cats' corrective response, termed the Force Constraint Strategy, was such that each hindlimb produced a ground-reaction force, in one of two directions, with amplitude modulated to the direction of perturbation. Electromyographic recordings, which represent muscle activation patterns, demonstrated that the postural response is tuned to the direction of the supporting surface perturbation. It has been claimed that postural responses are determined by proprioceptors projecting to supraspinal centers, rather than from spinal reflexes [35]. Supporting evidence of cortical control comes from studies of human soleus muscle responses during support surface perturbations that indicated corticospinal involvement during the late phase of stance control [23].

Vestibular receptors detect acceleration of the head in both gravitational and inertial reference frames [19]. The otolith organs of the vestibular system sense linear acceleration produced by translation (horizontal, vertical, or lateral movement), the direction of the gravitational acceleration, and body tilt, which helps in setting a spatial vertical reference. The semicircular canals detect rotational acceleration associated with

motion in a curved path. The vestibulo-ocular system's capacity for precisely coordinated large scale movements and fine motor control is limited owing to its location in the head, the movement of which is independent of that of the rest of the body. Experiments performed in cats indicated the vestibular loss affect the scaling but not the direction of the muscular responses to translational perturbations [36]. Furthermore, the vestibulo-ocular reflex is quite slow and insufficient to account for observed short latency responses to postural disturbances [37, 38].

Cutaneous receptors, which are found in three principal varieties, namely mechanoreceptors, thermal receptors, and nociceptors [39], are situated in or near the junction of the dermis and the epidermis. Postural regulation [40] makes the most use of mechanoreceptors, particularly those that respond to skin movement. In experiments investigating postural responses to rotation and translation, it was proposed that the cutaneous receptors may be responsible for the directional tuning of the automatic response for maintaining balance [41]. However, later experiments in which cutaneous feedback was abolished indicated that that, similar to the vestibulo-ocular system, cutaneous receptors affected the gain but not the direction of the response [42].

Muscle spindles are made of both muscular and sensory components. Spindles contract via specialized, cells with striated areas at its ends called intrafusal muscle fibers. The central regions are non-contractile. There are two main types of these multi-nucleated intrafusal fiber: nuclear bag and nuclear chain [43]. The nuclear bags are further categorized as static, because they respond to slow steady changes in muscle length, and dynamic, which respond to rapid changes in muscle length. Intrafusal fibers are embedded in the core of and oriented in parallel with the main extrafusal fibers of

muscles. Sensory information is recorded by (i) large-diameter (12-20 um) group Ia, myelinated primary sensory fibers, which innervate all the intrafusal fibers; and (ii) smaller-diameter (6-12 um) group II, myelinated secondary sensory fibers that innervate the chain fibers and static bag only. Motor input, in contrast to the large-diameter alpha motor neurons that innervate the extrafusal muscle fibers [44], is provided by two types of small-diameter gamma motor neurons. While static gamma motor neurons make connections with the static bag and chain fibers, dynamic bag fibers are innervated only by dynamic motor neurons. Ia afferent enters the dorsal spinal cord, crosses the intermediate zone, and forms a monosynaptic connection with an alpha motor neuron in the ventral horn, which in turn innervates the same muscle containing the activated muscle spindle. Ia afferents encode both change in length and change in velocity, with a discharge frequency that is directly proportional to the extent of spindle stretch. Group II afferents, however, predominantly encode stretch. Muscle spindles have been implicated in providing input on leg stance width, as well as information on perturbation direction and velocity, to the central nervous system so that it can make appropriate adjustments to the disturbances [45].

The Golgi tendon organ (GTO), which consists of a capsule innervated by a group Ib axon, lies in series with the muscle, at the musculotendon junction [46]. The Ib fiber is a large diameter afferent (12-20um), comprised of an unmyelinated, branched network within the capsule that is entwined with collagen fibers of the tendon. The afferent leaves the capsule as a single myelinated nerve and enter the spinal cord through the dorsal root where it synapses at a variety of alpha motor neurons innervating the homonymous muscle. Unlike the spindle afferent, the GTO's connection is not monosynaptic, but first

makes an intermediate synapse with an interneuron, which in turn synapses with the alpha motor neurons. The tendon organ nerve fibers within the capsule are mechanoreceptors, which sense the pressure exerted by stretching of the tendon owing to increased muscle tension during active contraction of extrafusal muscle fibers [46]. The response rate of discharge of these Ib sensory mechanoreceptors is directly related to the force applied [47, 48]. It has been suggested that group I fibers determine the triggering on postural responses to perturbations since there were significant delays following their removal [49]. Moreover, patients suffering from diabetic peripheral neuropathy, in which there is somatosensory loss, have a diminished ability to regulate the magnitude of torque in response to postural disturbances, indicating a role for these receptors in scaling of postural response magnitude [50].

Some the aforementioned research [4, 36, 42] has shown that loss of supraspinal, namely the cortex and vestibulo-ocular, and cutaneous inputs only affect the magnitude of the postural response to translational disturbance but not its direction. This leaves only somatosensory, spinal reflex pathways (such as spindles, and maybe joint receptors) and limb architecture (including intrinsic mechanical properties like inertia, viscoelastic properties of muscle, skeleton, fascia, ligaments) as necessary and sufficient parameters for producing the directional response.

1.2.2 Mechanical Analysis: Stiffness

Interaction with the environment often involves compensation of a limb for instabilities so as to maintain posture. The question of which hierarchical levels of the musculoskeletal system are involved and their specific contributions remains an

unresolved issue. The continuous feedback of muscle proprioceptors (muscle spindles, Golgi tendon organs and cutaneous receptors) through spinal pathways has been thought to provide a mechanism of stiffness regulation [4, 51]. In this scenario, movement of the supporting surface would generate shear forces on the paws eliciting cutaneous receptor discharge, and stretching of some muscles and their tendons causing spindle and Golgi tendon discharge. All of these would be integrated spinally to elicit an appropriate corrective response. This stiffness regulation has been posited to contribute to the control of posture by the neuromusculoskeletal system [29, 52].

The stiffness is a measure of the force response of an object with respect to a displacement of the object. The determination of stiffness was performed under the assumption that the neuromusculoskeletal system is mostly spring-like in nature [30]. Thus, for perturbations in the sagittal plane about a reference position, the force response is directly proportional but at varying angles of direction. The behavior is represented by the following equation:

$$\begin{bmatrix} F_x \\ F_z \end{bmatrix} = \begin{bmatrix} K_{xx} & K_{xz} \\ K_{zx} & K_{zz} \end{bmatrix} \begin{bmatrix} dx \\ dz \end{bmatrix} \quad or \;\; F = K\, dx\,,$$

where F_x and F_z are the horizontal and vertical components of the force response, dx and dz are the corresponding components of the given perturbation, and K_{xx}, K_{xz}, K_{zx}, and K_{zz} the elements of the stiffness tensor. The stiffness tensor can be calculated by a least-square regression of the force and displacement. Algebraically, a system is spring-like if its curl is zero. The curl is calculated as the difference between the off-diagonal terms of the stiffness tensor, K_{zx} and K_{xz}.

The tensor describes what has been referred to as a stiffness ellipse (Figure 1.1), which is produced by multiplying the displacement vectors by the stiffness tensor, and can be characterized in several ways.

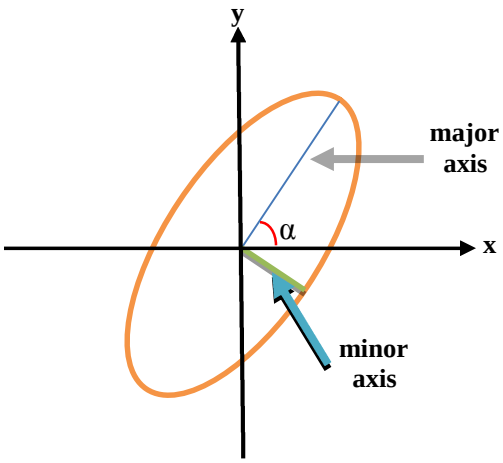

Figure 1.1: Stiffness Ellipse. Representation showing the major (K_{max}) and minor (K_{min}) axes and the angle, α, of the major axis with the horizontal axis.

The long/major axis of each ellipse gives the direction of displacement for which the restoring forces are maximal while the short/minor axis gives the direction of displacement for which the restoring forces are minimal. The maximum (K_{max}) and minimum (K_{min}) stiffness can be obtained by the eigenvalues of the stiffness tensor. The angle of the major axis with the x-axis (α), the stiffness orientation, can be calculated from the eigenvectors. The shape index represents the level of anisotropy of the stiffness ellipse. A higher shape index corresponds to greater anisotropy. The shape index is calculated from the ratio of K_{max} to K_{min}.

The stiffness matrix can be divided into symmetric, K_S, and antisymmetric, K_A, components as follows:

$$K_S = \frac{K + K'}{2} \quad , \quad K_A = \frac{K - K'}{2},$$

where K' represents the transpose of K. In a spring-like system the stiffness matrix is symmetric, that is $K_{xz} = K_{zx}$. This is due to the fact that, since the curl is zero, the symmetric component is the same as the stiffness matrix itself, i.e. $K_S = K$. The antisymmetric component, K_A, like the curl is equal the zero. The curl is, in fact, a quantification of the level of asymmetry in the system. Therefore, the symmetric matrix is a representation of the spring-like characteristic of the stiffness while the antisymmetric matrix is a representation of the curl component. The magnitude of the curl forces can then be compared to those of the symmetric component to evaluate the level of non-spring-like behavior. The ratio of the curl to the smallest (K_{min}) and largest (K_{max}) eigenvalues gives the values Z_{max} and $Z_{min,}$ respectively. Non-spring-like behavior can be measured by a parameter referred to as Z_{mean}, a geometric mean of Z_{max} and Z_{min} [29]. Z_{mean} is calculated by the following equation:

$$Z_{mean} = \sqrt{\frac{|K_A|}{|K_S|}} \ ,$$

where | | represents the determinant. Because the muscle is assumed to be spring-like, antisymmetry indicated by a non-zero curl could only be as a result of asymmetric neural feedback gain between muscles (Hogan, 85).

1.2.3 Musculotendon Anatomy and Contraction Dynamics

At the gross level, skeletal muscle is comprised of fascicles, which are bundles of muscle fibers. A group of these fibers, together with the motor neuron that innervates them, constitute a motor unit, the smallest system that can be physiologically activated

[53]. Activation initiates changes within the sarcomeres, the fundamental force-generating unit of the muscle fiber (Figure 1.2). The sarcomere consists of thin and thick filaments called actin and myosin, respectively. Contraction takes place when actin and myosin slide past each other via the action of the myosin heads or cross-bridges [32, 54]. At an optimal overlap between actin and myosin, the sarcomere is at its optimal length and produces its maximum possible force. Below that length, the actin filaments begin to overlap and interfere with cross-bridge motion, thereby reducing the force output. At lengths greater than optimal, fewer cross-bridges are formed and so the force-generating potential of the muscle is diminished.

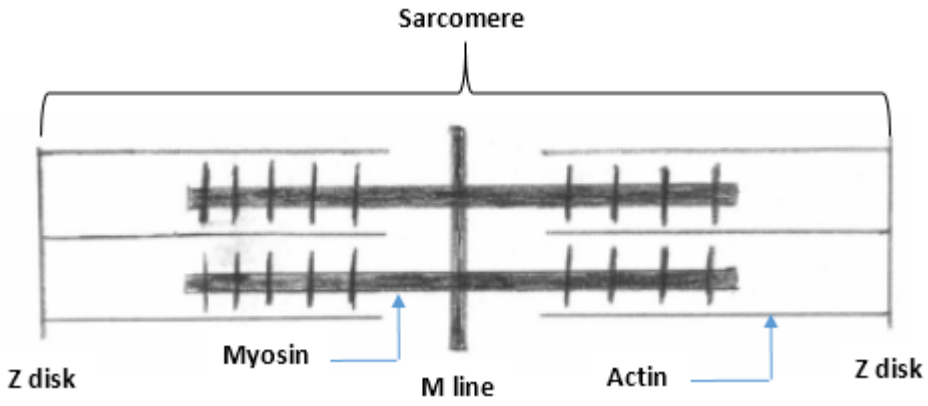

Figure 1.2: Sarcomere structure.

The same behavior occurs at lower levels of activation, with correspondingly reduced force-producing capacity. At no activation, passive elastic structures within the muscle produce a resistive, tensile force when stretched beyond the relaxed state. This force-length relationship at various activation levels (stimulation frequencies), including at no activation (passive) and the total force at maximum activation, are illustrated in Figure 1.3 [55-57].

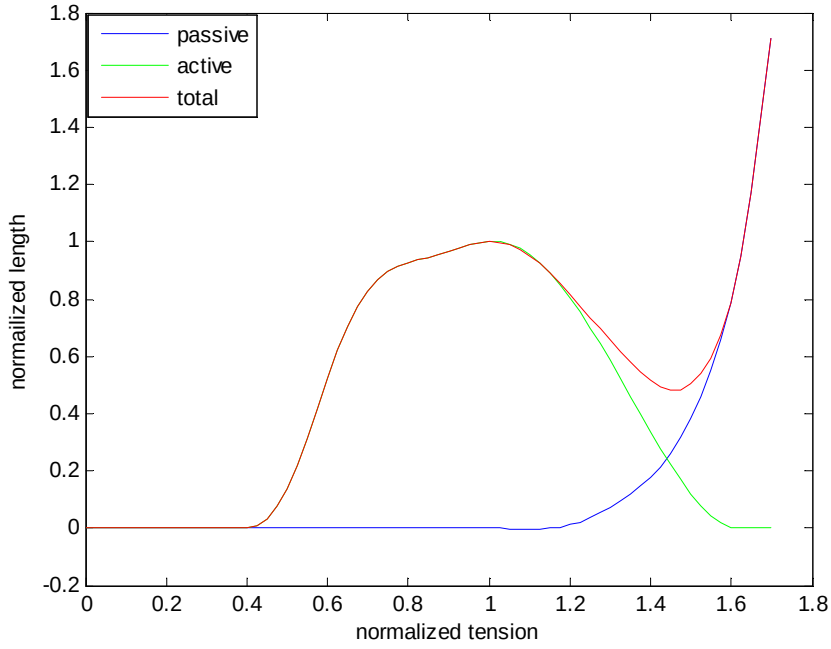

Figure 1.3: Normalized force-length curves.

The force produced by a muscle is also a function of its velocity. During shortening, or concentric contraction, of a muscle activated at high frequency, the force produced is less than that of isometric (zero velocity) contractions. As the shortening velocity increases, fewer crossbridges are able to attach themselves, and so the force decreases (Figure 1.4). In eccentric or lengthening contractions, the muscle acts as if to resist lengthening, and the force generated exceeds that produced in isometric contraction [58]. At lower stimulation rates, however, the tension at lower velocities does not drop as much as during high stimulation rates leading in some cases to the isometric tension being higher than that at both lengthening and shortening contractions.

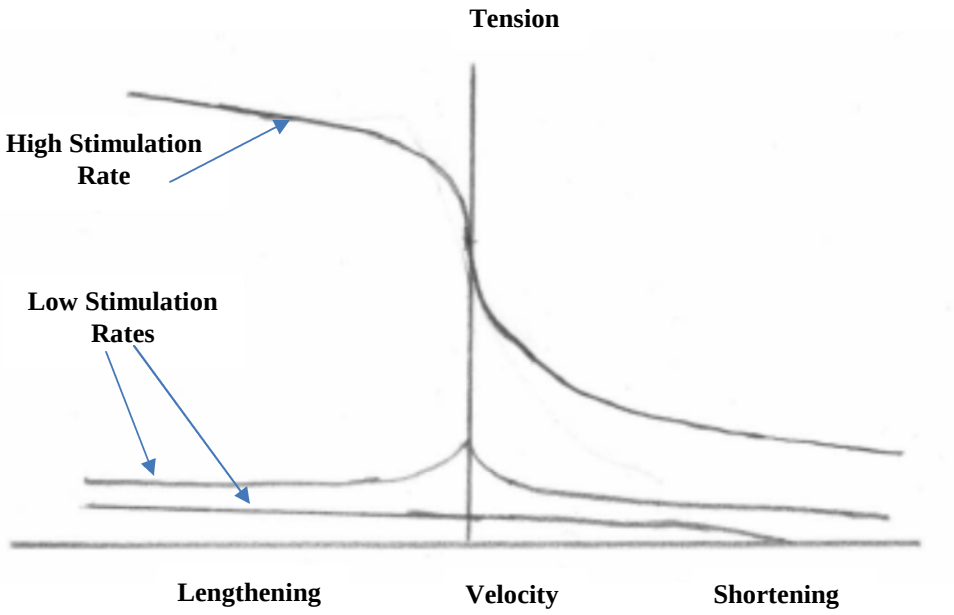

Figure 1.4: Muscle fiber force-velocity curve.

Electrical stimulation sufficient to produce an action potential causes in influx of calcium ions intracellularly, which leads to a muscle twitch. The same input, introduced after the muscle has completed relaxed, produces the same muscle response and force profile. If the neural input is supplied before the muscle force response has fully decayed, however, the still available calcium ion is supplemented by a further influx, resulting in a higher force response than the first twitch [59]. The same phenomenon is observed if successive inputs are applied at sufficiently short time intervals. The increase in force diminishes, however, at each successive step, eventually reaching a plateau. This state is known as tetany and is the means by which a muscle can produce various levels of force.

Muscle actuation is influenced by muscle architecture and fiber type [60, 61]. Based on histochemical properties, muscle fibers have been classified as having three

types. Type I, also known as slow-twitch, oxidative fibers, generally have the smallest diameters, the longest contraction times, and the highest frequency of recruitment. Type IIa, or fast oxidative glycolytic, fibers are larger than type I, have shorter contraction times, and are active less frequently. Lastly, type IIb, or fast-twitch, glycolytic, fibers have the shortest contraction times, the largest diameters, and are active only when high force is needed. Force is generated and modulated according to the recruitment of muscle units, as well as the change in firing rate of neural input to motor units. Motor units are recruited according the Henneman size principle [62]. The small-diameter, fatigue-resistant, slow twitch units are recruited first, followed by the fast-twitch, fatigue-resistant units, and finally by the large-diameter fast, fatigable fibers.

Muscle contractile properties are affected by muscle architecture properties, such as muscle mass, fascicle length, and pennation angle. Large-volume muscles possess large numbers of fibers, particularly of the large diameter variety, to produce high forces, but at a greater metabolic cost. Long fascicles, which indicate a high number of sarcomeres in series, have a higher maximum shortening velocity than short fascicles. However, the fiber length does not affect the intrinsic force-velocity characteristic of the muscle. Fibers arranged parallel to the line of force can achieve maximum force from the muscle. Pennate fibers, arranged at angles askew to the line of force, tend to lower the maximum force obtained. However, a pennate arrangement allows more fibers to be packed into the muscle. This increased packing results in a greater physiological cross-sectional area, the sum of the areas in each fiber, of the muscle. The force-generating capacity of a muscle is proportional to its physiological cross-sectional area, so higher pennation generally leads to higher force-production capability. The combination of

these characteristics can produce diverse effects. Muscles with long fibers are adapted for high-velocity contraction as well as force production over a large range of motion. Short, pennate fibers (large PCSA), as well as the action of eccentric contraction, are metabolically economical for force production [63]. Muscle volume, which predicts metabolic cost, is minimized by having short fibers with fewer sarcomeres in series. In short, muscles are structurally-specialized to meet their functional demands. To generate the necessary propulsive forces, the limb possesses muscles with large PCSA, and so large force-generating capacity. Much of this mass is maintained close to the trunk, with the distal limb muscle being replaced by as much tendon as possible to decrease rotational and energy cost effects on the swinging limb.

Any force generated by the muscle is transmitted through the tendon to the limbs. The tendon, composed of an aponeurosis (portion internal to the muscle), and an external tendon, is a passive, viscoelastic element made of collagen fascicles arranged approximately parallel to each other. The tendon strain is defined as the ratio of the tendon extension to its resting, or slack length. When it is slack, the tendon will not carry any load. At low strain beyond the slack length, the tendon exhibits a nonlinear force-strain relationship. At greater strain beyond approximately 1.2%, the force-strain relationship becomes linear. At maximum force (Figure 1.5), a tendon will produce a strain of about 3.3% [57].

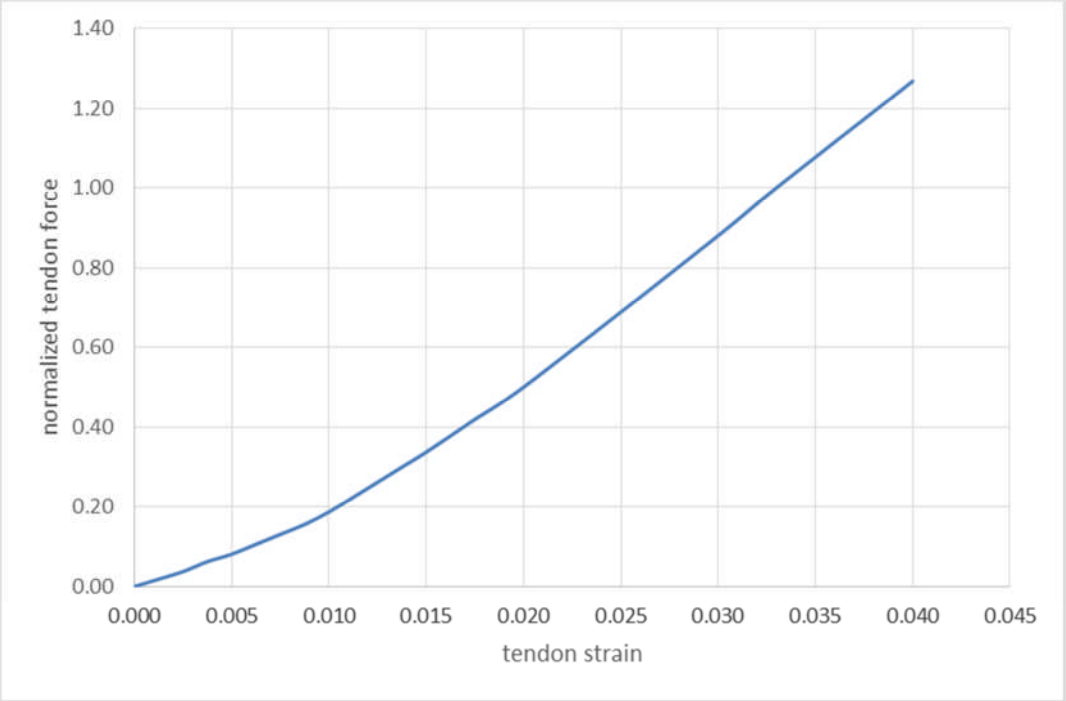

Figure 1.5: Normalized tendon force-strain curve. The tendon force is normalized by the optimal muscle force.

1.2.4 Neuromusculoskeletal Modeling

Neuromusculoskeletal models aim to estimate and predict kinetics, that is, the forces and torques experienced by the system under static and dynamic conditions.

1.2.4.1 Modeling of Muscle Force

A musculotendon Hill model is composed of an elastic or viscoelastic tendon in series with a muscle fiber (Figure 1.6), the latter of which has a parallel arrangement of a contractile and elastic element (Figure 1.6). The force produced by the active or contractile element can be represented by the function

$$F^m(t) = a(t)F(v)F(l)F_o^m,$$

where $F^m(t)$ is the muscle-fiber force, $a(t)$ the muscle activation, $F(v)$ the normalized velocity-dependent fiber force, $F(l)$ the normalized length-dependent fiber force, and F_o^m

the maximum isometric muscle-fiber force. Thus, the model makes use of the force-length and force-velocity relationships and the activation dynamics to estimate the force generated by each muscle.

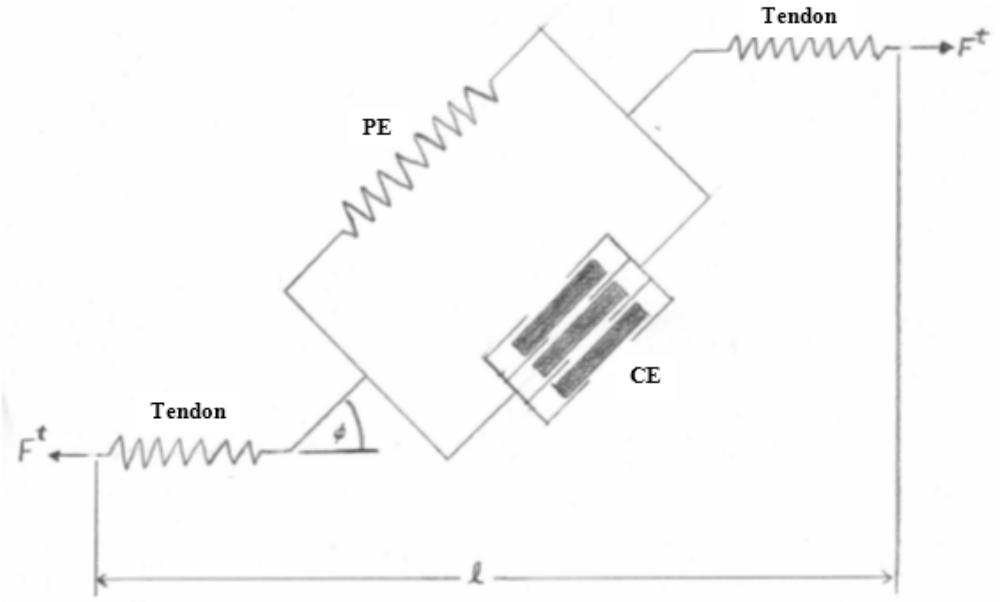

Figure 1.6: Hill-type muscle model with tendon. The muscle fiber is in series with the tendon at a pennation angle of α. This muscle is composed of a force-generator (contractile element, CE) and spring (passive parallel elastic component, PE).

Modeling the force-velocity relationship involves the use of a pair of equations, one for concentric and the other for eccentric. The first is as follows:

$$(F^m + a)(v^m + b) = (F_o^m + a)\, b,$$

where F^m is the tensile force, F_o^m the optimal force, and v^m the muscle shortening velocity [31]. The equation describes a hyperbola with asymptotes at $F^m = -a$ and $v^m = -b$.

The portion of the force-velocity relationship corresponding to eccentric contraction is described as follows:

$$F^m = F_E^m F_o^m - (F_E^m - 1)\frac{F_o^m\, b' + a' v^m}{b' - v^m}.$$

a' and b' are the equivalent eccentric contraction values to a and b, and F_E^m is the coefficient, usually between 1.1 and 1.8, that sets the limit for the maximum muscle force [64].

Most tendons are assumed to be elastic [57] and the normalized force-strain curve (Figure 1.5) is scaled by the maximum active muscle force and the tendon slack length.

The force on the tendon is modulated by the pennation angle, the angle between the muscle fibers and the tendon (Figure 1.6), using the equation

$$F^t = F^m \cos(\propto),$$

where F^t is the tension in the tendon, F^m the muscle force and $\propto$ the pennation angle. The pennation angle only begins to have a significant effect on muscle force at values exceeding 20 degrees.

All these parameters are usually integrated into a musculoskeletal model. Although equations can be used for the force-length-velocity relationships, an alternate strategy employed involves explicitly constructing a lookup table of values through which a spline can be fit.

Although both mechanistic and phenomenological models have drawbacks, some of which were cited earlier, the latter exhibits superior performance for the type of study proposed [65].

1.2.4.2 Activation Dynamics

A neural command to the muscles can be inferred by recording their electromyogram (EMG) signals. The greater the number of motor units activated the larger the EMG signal. As an input parameter, the magnitude of EMG is problematic because it may vary with motor unit size, muscle temperature, electrode placement in the

muscle, amplifier gain, or any number of other factors. Thus, in biomechanical modeling, the EMG magnitude is usually converted to a parameter called muscle activation, which ranges from 0 to 1. One method of transforming EMG to muscle activation is to normalize it by the peak EMG of the maximum voluntary contraction (MVC) [66]. Another process is to solve a differential equation that relates the EMG to the neural activation [57].

1.2.4.3 Parameter Integration and Considerations

A musculoskeletal model includes information such as limb geometry, the kinematics of the joints, and line of muscle force-propagation [27]. The limb geometry and joint kinematics are important for estimation of moment arms or musculotendon lengths. Physiological joints are only approximations of the revolute or spherical joints of engineering and so have uncharacteristic rotations or translations. This means that the joint centers are not fixed and, hence, the moment arms are not constant, but change as a function of the joint angle.

Modeling the musculotendon unit as a straight line from origin to insertion can pose problems. In certain cases this will result in the modeled unit passing through a bone rather than wrapping around it. In extreme cases, it may cause the musculotendon unit to change its action, that is, acting as a flexor instead of an extensor or vice versa.

Since most of the functions describing force-generating capability are normalized, certain physiological parameters are employed to fully characterize the muscle model. These parameters include the maximum muscle force, the optimal fiber length, the tendon slack length, and the pennation angle. Another parameter, the maximum fiber shortening

velocity may also be required. Alternatively, it can be calculated as a ratio of the optimal fiber length and the timescale for muscle activation.

Studies across various species indicate that the forelimb is quite distinct from the hindlimb. Indeed, it has been found that various animals employ diverse strategies, and thus possess differing muscular adaptations, to fulfill their postural and locomotory requirements. Goslow et al. [67] showed that the dog uses a strut or spring mechanism depending on the task. During trotting and galloping the extensors undergo eccentric contraction, as required for elastic energy storage on landing, followed by concentric contraction as it propels itself forward. Williams et al. [68] examined the same characteristics in dogs bred for speed, greyhounds. It was found that proximal bi-articular muscles triceps brachii longus and biceps brachii show specialization for strut-like stiffening for support and in dynamic control. Due to stiff tendons, distal muscles do not perform elastic energy storage and recovery [68]. The hare uses its forelimb as a strut, exhibiting little elastic storage capacity and may merely support and deflect the body while the hindlimb provides the propulsive force [69]. Therefore, limb structure is less specialized as it also employs its limbs for digging and manipulation. In the horse, the large volume pelvic limbs generate large forces and the long-fascicled thoracic limbs produce smaller forces over a large range of motion [70-73]. The pelvic limb functions mainly in propulsion while the thoracic performs weight support with the distal limb functioning as a 'biological spring' through elastic storage and release.

These studies would suggest that an implementation of the forelimb is required to more clearly understand the mechanisms of posture and locomotion. As such, our objective is to analyze the anatomy and muscle architecture in detail. We hypothesize

that the forelimb has a structure that allows for some functions, such as turning or manipulation, that are distinct from those of the hindlimb. Second, the data must be input into a musculoskeletal modeling platform that allows visualization of limb and muscle geometries and permits manipulation of the model parameters such as joint angles and muscle activations. Musculoskeletal models give us the ability to examine the role of separate systems in regulating various capabilities of the musculoskeletal system by looking at the effect of the assumptions made as to the structure of the various systems, as well as the impact their inclusion or exclusion of the behavior. This can enable us to gain insight into the control mechanisms in a potentially faster and less expensive manner. As the model becomes more complex, it could be used to predict outcomes of experiments that might be intractable, or to reduce the number of required experiments. As such, a mathematical model serves as an important research tool.

1.3 Current Research Problem

A musculoskeletal model such as has been described is only as accurate as the anatomical data. Using physiological data the model parameters must be calibrated but not over-fit [25, 26, 28, 74, 75]. This is so that the model can then be utilized with unfamiliar data, without further parameter adjustment, to predict the outcome of novel tasks. Researchers have implemented three-dimensional, anatomical, musculoskeletal, computational models [25, 26, 28, 75], to further understand the role of muscles in postural regulation. The Burkholder and Nichols model [25, 26], which is based on a cat hindlimb, describes the action of 32 musculotendon units, with 7 degrees of freedom: 3 at the hip, 2 at the knee and 2 at the ankle. This model thus employed musculoskeletal

architecture (without need for higher/supraspinal control) as the sole basis for predicting the pulling directions of and endpoint forces generated by various muscles during perturbations to the endpoint, the results of which have been experimentally corroborated [4, 76, 77].

This experiment involves the measurement of endpoint muscle forces in response to a perturbation. Macpherson [9] proposed that supraspinal input was required to produce the force constraint strategy. However, the decerebrate cat was found to produce the tuned muscular responses of force constraint without visual and vestibular feedback [78]. Furthermore, muscle spindle responses in anaesthetized cats were also appropriately tuned [79]. Hence, our objective was to revisit the question of whether neural input - specifically spinal reflexes - was required for force constraint, or were architectural factors sufficient. With this in mind, we examined the responses in both anaesthetized (referred to in this document as **passive)** and un-anaesthetized (referred to as **active**) states. We hypothesize that the limb architecture will be sufficient to generate the force constraint behavior.

Much of the research examining postural strategy in cats has focused on the horizontal plane, wherein the forelimb does not display a strong force constraint strategy [9]. However, a large proportion of the cat's response occurs in the vertical plane. Therefore, our objective was to extend the research on postural strategy to the sagittal plane. We hypothesized that the animal would display a stronger force constraint behavior in the sagittal axis than it does in the horizontal axis.

In experiments investigating arm posture in humans Mussa-Ivaldi et al. [30] demonstrated that the major axis of stiffness was along the line from the endpoint, or

hand, to the base pivot point, or shoulder, and re-directed itself based on posture. To verify this behavior, and determine the effect of state (passive or active) we examined the stiffness response for the limb in two different positions: one that represented the cat in an extended standing posture and another in a crouched posture.

Last, the limb and joint parameters such as length, centers of rotation, and moment arms of the model will be calibrated based collected experimental data, and the calibrated model validated for its ability to correctly predict all the essential features observed in an experimental task.

CHAPTER 2:

MUSCLE ARCHITECTURE REFLECTS FUNCTIONAL DEMANDS

2.1 Introduction

Postural stability and locomotion depend on proper actuation of limb segments by the muscles, the functional properties of which are influenced by architecture and phenotype [60, 61]. Forelimb function and structure are dramatically different from those of the hindlimb [67, 80-84], and these differences may influence the pattern of architectural specialization. Primary limb functions include weight support, propulsion, turning and manipulation, but the contributions of the fore- and hind-limbs to these tasks is not symmetric. During postural support tasks, the feline forelimb stayed fixed and extended, acting mainly as vertical struts, while the hindlimbs provide more dynamic responses to perturbation [7, 85]. In many species, locomotion can be segmented into a braking phase dominated by the forelimbs and a propulsive phase with power produced by the hindlimbs [8, 9, 86, 87]. Turning during high speed locomotion is an important part of prey pursuit and requires large lateral force production. Turning can be controlled either by forelimb placement [88, 89], or by the direction of hindlimb force production [90]. The cat appears to execute much finer-grained level of control over forelimb than the hindlimb during locomotion, suggesting that they rely on the forelimbs [6]. The cat forelimb is also used for manipulation tasks such as foraging and prey capture [5, 81], tasks that require greater diversity of motion than gait, including powerful flexion of the

paw [81]. The greater functional diversity of the forelimbs over the hindlimbs may be reflected in greater architectural complexity.

Muscle architecture properties, such as muscle mass, fascicle length, physiological cross-sectional area (PCSA), and pennation angle, describe the arrangement of contractile tissue within the muscle and the relationship between intrinsic contractile performance and extrinsic muscle function. PCSA, indicative of sarcomeres in series, is proportional to maximal isometric tension [91]. For muscles with identical fiber types, maximum shortening velocity and range of motion are directly proportional to fascicle length and the number of sarcomeres in series [92, 93]. Muscles with long fascicles are described as adapted for high-velocity contraction, while muscles with short fascicles are often described as adapted for isometric force production [63]. Pennated fascicles, arranged at an angle to the line of force, allow more fascicles to be packed into the muscle increasing the physiological cross-sectional area at the cost of reducing fascicle length.

Muscles are structurally-specialized to meet their functional demands. The contractile properties of scup muscle vary systematically with the local kinematics of swimming [94] . The frog semimembranosus seems to be structured to provide maximal power during jumping [95]. Anti-gravity and propulsive muscles in the hindlimb have much greater force-generating capacity than their antagonists [61]. Much of this mass is concentrated proximally to decrease rotational and energy cost effects on the swinging limb [96]. On the other hand, structural specializations may not contribute directly to muscle function, but may reflect other anatomical constraints. For example, Burkholder

et al. [60] reported that pennation angle was highly conserved within functional groups, but had very little influence on contractile performance.

This study was based on the hypothesis that muscle architecture will reflect the functional demands. Because of its role in locomotion, the forelimb was expected to show some of the same patterns as the hindlimb: a proximo-distal gradient in muscle mass to minimize the metabolic cost per stride [96], and specialization of the anti-gravity muscles to possess greater force-producing capacity and shorter fascicles than their antagonists. The unique mechanics of foraging and prey capture, like supination and flexion of the antebrachium and greater capacity for bone-mediated force transmission were expected to reduce the apparent specialization, particularly of elbow flexors and extensors.

Although the domestic cat has been a powerful model system for the study of neurological mechanisms, much of this work has focused on the hindlimb. Mechanical models of the hindlimb have helped to highlight powerful neuromechanical interactions, such as the role of biarticular muscles, the importance of cross-joint coordination, and the role of local proprioception in shaping global limb mechanics. No such model of the forelimb exists. Given the unique structure and functions of the forelimb, unique control processes may be required. Data collected during this study of structure, and its relation to function, form the basis of a mathematical model of the forelimb.

2.2 Material and Methods

The right forelimb was harvested from six female, adult cats (*Felis domesticus*) weighing 4.5-5.5 kg (Liberty Research, Inc., Waverly, NY). These animals had been sacrificed as part of unrelated studies involving only the hindlimbs. All research was conducted in compliance with Georgia Institute of Technology IACUC protocols for the study of vertebrates and adhered to the legal requirements of the United States of America. The limb was skinned, disarticulated at the scapula, mounted in a rigid external frame in a stance-like posture, and fixed in 4% paraformaldehyde for 3-4 weeks.

The origin, insertion, and via points of each of each muscle (Table 2.1) was recorded using an electronic stylus (MicroScribe MX, Solution Technologies, Inc., MD). Muscle point recording for each specimen was performed over the course of several weeks, with the limb being stored in phosphate buffered saline (PBS) at 4°C between measurements. Each point was digitized on at least three separate sessions. During each digitization session, the limb was mounted within the workspace of a digitizer, and the stylus was positioned at each muscle origin, insertion and via point (centroid for broad attachments), and its location recorded. Repeated measurements of calibration points indicate that this system has a reproducibility of ±2mm. Each muscle follows a unique path between origin and insertion. In many cases, this was a reasonably undistorted, straight line. In those cases, such as biceps brachialis, only muscle origin and insertion were recorded. In cases where the path of a muscle makes a distinct change in direction the location of these intermediate via points was also recorded. In addition to muscle points, reference points on the immobilization frame were recorded to permit registration

of successive measurements. After at least 3 recordings of each point on a muscle, the muscle was carefully removed to expose the deeper tissue.

Muscles from four of these specimens were cleaned of excess fat and connective tissue and used for architectural measurements. Muscle mass was measured using an analytical balance (Mettler Toledo, Inc., Columbus, OH), length with dial calipers, and pennation angle with a goniometer. Muscles were then digested for 2-4 days in 5% nitric acid. Fascicles of approximately 100 fascicles were dissected from three separate parts of each muscle and mounted on slides with Permount. The lengths of the dissected fascicles were measured with dial calipers, pennation angle with a goniometer, and sarcomere lengths (Appendix) were measured using the laser diffraction technique [97].

These measured properties were used to calculate derived architectural parameters. Sarcomere number was given as the ratio of fascicle length to sarcomere length. Physiological cross-sectional area (PCSA) was calculated as:

$$PCSA = \frac{m\, cos \propto}{l\, \rho},$$

where m is the muscle mass, α is the pennation angle, l is the fascicle length and ρ is muscle density (1.056 g/cm^3, [98]). Optimal muscle and fascicle length were determined by normalizing to optimal sarcomere length (2.43 μm) [99]. The calculations were as follows:

$$Sarc.\# = \frac{FL}{SL},$$

$$Optimal\ FL = Sarc.\# \times 2.43\mu m,$$

$$FL\ ratio = \frac{FL}{ML},$$

$$Optimal\ ML = \frac{Optimal\ FL}{FL\ ratio},$$

where FL represents the fascicle length, Sarc. # the number of sarcomeres, SL the sarcomere length, and ML the muscle length.

Moment arms for select wrist and elbow muscles were determined in four separate animals from tendon excursion during joint rotation [100, 101]. Eight forelimbs (4 left, 4 right) were skinned and disarticulated from cat cadavers. The limb was immobilized in a frame, using 2 mm Steinman pins through the ulna and radius for measurement of wrist moment arms, or through the humerus for measurement of elbow moment arms. Sutures were attached to the distal tendon, routed along the corresponding muscle, wrapped around a potentiometer (Novotechnik U.S. Inc., Southborough, MA), and held under 6 N tension by a suspended mass. Joint positions were measured using a dual axis electro-goniometer (Biometrics Ltd., Ladysmith, VA). To stabilize the goniometer connection to the paw, a flat rectangular plate was set on the dorsal surface of the distal limb and wrapped in fast-setting plaster bandage (BSN Medical Inc., NC), and the goniometer taped to this surface. The proximal end of the goniometer was fixed to the immobile proximal limb. The elbow was assumed to have a single degree of freedom, and the non-flexion angle changes (<8°) were discarded. Outputs from the potentiometers and goniometer were digitized at 250 Hz while the distal limb segment was manipulated through its range of motion. Special attention was paid at the wrist to avoid supination/pronation about the radio-ulnar joint while maximizing both flexion/extension and radial/ulnar deviation. The excursion versus joint angle data were fit with stepwise polynomial regression [102] and differentiated to obtain the moment arm curves.

Muscles were assigned to functional groups based on attachments and previous descriptions [103, 104]. In the case of bi-functional muscles, the muscle was assigned to the group for which it had the larger apparent moment arm. Comparisons between the functional groups of muscles were made for each architectural property using one-way analysis of variance (Statview 4.0, Abacus concepts, Inc., Berkeley, CA), and, in the case of a significant statistical value ($p<0.05$), a Fisher's protected least significant difference (PLSD) post-hoc test performed between pairs of functional groups.

2.3 Results

Qualitatively, the cat forelimb is more complex than the hindlimb, with substantially more and denser connective tissue and compartmentalization. The forelimb possesses many complex, multi-pennate, muscles, unlike the more fusiform, uni-pennate muscles typically found in the hindlimb. In addition, muscles of the forelimb tend to have shorter external tendons, with fibers found to insert nearly to the distal joint. Architectural properties for the 29 muscles are shown in Table 2.1. They are classified by functional group and vertically arranged from proximal to distal. The naming convention used is Crouch [103], but other nomenclature has referred to palmaris longus as flexor digitorum superficialis, to epitrochlearis as tensor fasciae antebrachii, and to flexor digitorum superficialis as interflexorius [16].

Muscle size, measured by mass or PCSA, demonstrated a proximal-distal gradient (Figure 2.1). Although muscle mass varied significantly among functional groups ($p < 0.0001$), with the greater mass concentrated in the proximal limb and smaller mass in the distal limb, there was substantial diversity within the functional groups. For example, the

shoulder adductors (7.8±10.7 g) were the third largest muscle group, but include the diminutive coracobrachialis (0.31±0.04 g). The proximal shoulder extensor, shoulder adductor, and elbow extensor groups were significantly larger than the distal supinator (0.86±0.16 g), pronator (1.86±0.29 g), wrist extensor (1.70±0.93 g) and wrist abductor (1.82±0.27 g) groups, while the intermediate muscles could not be statistically resolved from either extreme.

Variance within each group is large, and in the distal limb the wrist flexors FCU and FDP and the wrist extensor ECR are at least 50% larger than their in-group counterparts, suggesting that the specific function of these muscles places greater demand on them. This intragroup variation was greater in PCSA and prevented statistical resolution of any systematic differences between functional groups. The calculated physiological cross-sectional area ranged from 0.08±0.03 to 10.25±1.19 cm^2 (Table 2.1) with a proximo-distal gradient (Figure 2.1b) that qualitatively appeared more clearly defined than that of the muscle mass. The shoulder extensors and adductors had numerically largest PCSAs (5.94±1.34 cm^2 and 5.29±7.02 cm^2, respectively), roughly 3 times that of the majority of muscle groups. The force-generating capacity of summed functional groups differed more clearly ($p < 0.0001$). Although no difference in PCSA could be resolved between anti-gravity muscle groups and their antagonists, and the ratio of combined anti-gravity to antagonist PCSA (Figure 2.2) was 5:4 for the shoulder muscles, there was a strong antigravity bias at the distal joints, approximately 4:1 at the elbow and 5:2 at the wrist. This supports the hypothesis that the weight-bearing functional group would possess greater force-producing capacity, although this is not reflected in homogeneous or systematic specialization of functional group members.

Table 2.1. Architectural properties of forelimb muscles classified by anatomical groups (±S.D.)

Muscle	Abbr	Muscle Mass (g)	Optimal Muscle Length (mm)	Optimal Fascicle Length mm)	Pennation Angle (deg)	PCSA (cm2)	Summed PCSA (cm2)
Shoulder Flexor							
Acromiodeltoideus	ACD	2.79±0.47	59.06±15.15	13.03±2.85	31±14	2.04±0.6	
Spinodeltoideus	SPD	3.54±1.01	72.11±4.14	32.94±3.52	1±1	1.01±0.4	4.75
Teres Major	TMA	8.47±1.36	84.69±2.62	46.05±5.7	7±5	1.7±0.38	
Shoulder Extensor							
Supraspinatus	SPS	17.23±1.84	86.11±4.24	27.2±5.64	6±3	5.94±1.33	5.94
Shoulder Adductor							
Coracobrachialis	CCB	0.31±0.04	30.99±12.04	11.03±7.23	0±0	0.34±0.25	10.59
Subscapularis	SSC	15.37±1.8	78.26±5.1	13.71±1.53	26±6	10.25±1.19	
Shoulder Abductor							
Infraspinatus	INF	13.15±1.7	78.91±4.91	18.36±3.09	15±10	6.62±1.07	7.32
Teres Minor	TMI	0.93±0.22	32.21±4.89	12.49±3.77	12±8	0.7±0.16	
Elbow Flexor							
Biceps brachii	BBI	5.85±0.98	81.03±8.67	25.09±7.55	10±10	2.27±0.81	
Brachialis	BRA	3.47±0.35	88.64±6.01	32.4±4.41	10±4	0.99±0.22	3.34
Brachioradialis	BRR	0.8±0.21	136.65±12.45	89.59±9.12	0±0	0.08±0.03	
Elbow Extensor							
Epitrochlearis	EPI	1.95±0.51	66.54±8.51	30.06±3.64	0±0	0.59±0.16	
Triceps brachii longus	TBG	22.89±3.93	93.05±8.08	23.86±7.1	13±11	9.2±2.75	13.85
Triceps brachii medialis	TBM	5.55±0.38	83.79±7.87	29.25±3.78	11±4	1.75±0.21	
Triceps brachii lateralis	TBL	9.01±2.19	78.12±5.58	36.82±5.07	8±3	2.31±0.84	
Forearm Pronator							
Anconeus	ANC	2.04±0.13	56.56±8.8	20.11±2.48	19±5	0.94±0.13	2.37
Pronator Teres	PRT	1.62±0.28	51.36±12.28	11.46±3.48	22±4	1.43±0.73	
Forearm Supinator							
Supinator	SUP	0.86±0.16	39.22±3.89	7.59±2.65	18±4	1.09±0.31	1.09
Wrist Flexor							
Flexor Carpi radialis	FCR	1.26±0.17	83.4±15.73	14.3±2.31	6±1	0.85±0.14	
Flexor Carpi Ulnaris	FCU	4.01±0.32	104.01±2.64	11.11±1.06	11±2	3.3±0.31	
Flexor digitorum profundus	FDP	9.27±2	103.91±6.13	21.54±2.75	7±12	3.97±1.07	10.77
Flexor Digitorum Superficialis	FDS	0.18±0.05	29.1±4.34	5.85±2.19	3±3	0.29±0.07	
Palmaris Longus	PAL	2.61±0.55	101.81±22.22	10.93±1.43	14±6	2.36±0.61	
Wrist Extensor							
Extensor carpi radialis	ECR	4.03±0.53	98.28±19.4	40.25±27.75	11±6	0.69±0.64	
Extensor Carpi Ulnaris	ECU	1.78±0.17	99.32±8.29	10.46±1.43	11±9	1.57±0.23	
Extensor digitorum communis	EDC	1.99±0.17	85.76±3.67	22.47±6.69	5±4	0.85±0.21	4.21
Extensor digitorum lateralis	EDL	1.22±0.12	88.47±5.17	14.24±5.97	10±5	0.85±0.23	
Extensor pollicis longus	EPL	0.55±0.07	86.14±8.11	20.99±6.03	1±1	0.25±0.08	
Wrist Abductor							
Abductor pollicis longus	APL	1.82±0.27	92.55±5.33	11.04±2.8	11±6	1.43±0.25	1.43

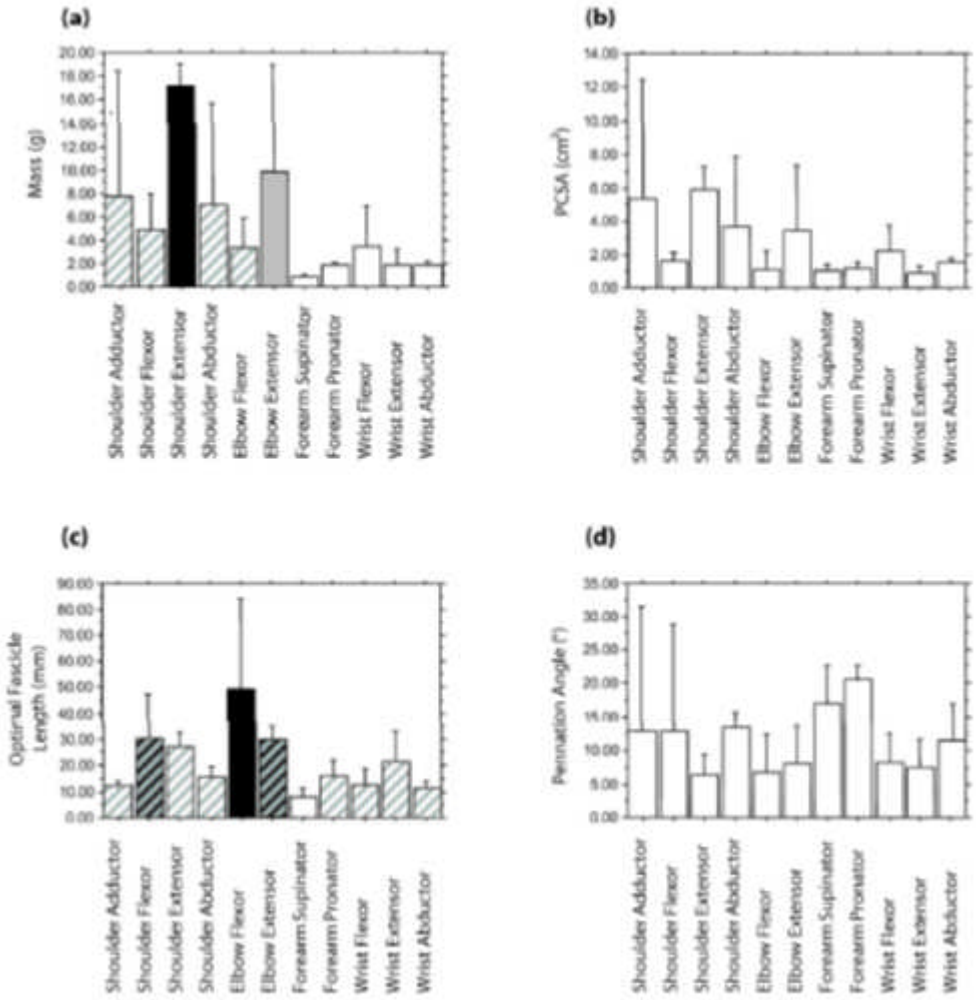

Figure 2.1. Histograms showing (a) the average mass, (b) the average physiological cross-sectional area (PCSA), (c) optimal fascicle length, (d) pennation angle, of each functional group. The bars represent 1 standard deviation. Bars sharing a common color (black: high, grey medium, open low) were statistically indistinguishable ($p > 0.05$).

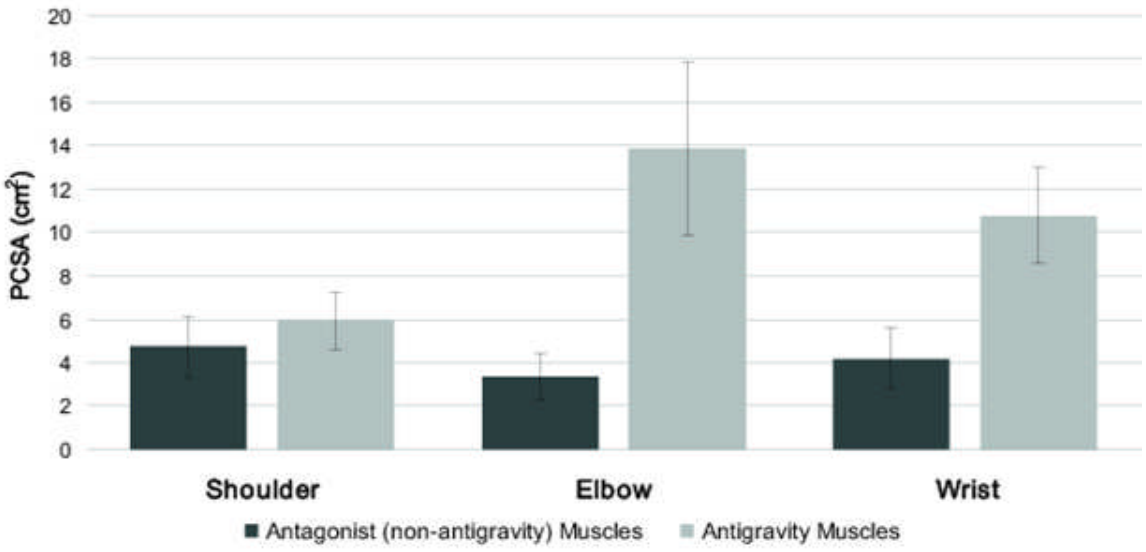

Figure 2.2. Combined PCSA. The combined PCSAs of anti-gravity muscles and their respective antagonists are compared across the shoulder, elbow, and wrist joints.

Fascicle length also varied substantially within the nominal functional groups, ranging from 5.85±2.19 to 89.6±9.1 mm (Table 2.1), with the elbow flexor brachioradialis (BRD) being substantially longer than the rest. Fascicle length of the anti-gravity shoulder extensors was 27.2±5.6 mm, and of the shoulder flexors 30.7±14.7 mm (Figure 2.1c). Because of the BRD, fascicle length of the elbow flexors (49.0±35.3 mm) was significantly greater than all other groups, including the elbow extensors, which averaged 30.0±5.3 mm ($p=0.06$). Antigravity wrist flexors were also numerically shorter than their counterparts (12.7±6.0 vs. 20.5±13.8 mm), although the small number of muscles in these groups prevent statistical resolution. The muscles with longer fascicles tended to be the more proximal flexors and extensors. The average fascicle lengths, however, are generally similar in the forelimb (78.1±25.8 mm) and the hind limb (84.1±22.9 mm).

The pennation angle ranged from 0 to 31° (Table 2.1) and showed the largest variability across muscles and functional groups, with variance ranging from 0% to 170%. This variability prevented statistical resolution of any systematic differences, although supinators and pronators had numerically greater pennation angles than forearm flexors and extensors (Figure 2.1d). There was a tendency for all muscles with actions out of the sagittal plane (abductors, adductors, pronators and supinators) to exhibit higher pennation angles. The exception to this phenomenon was the shoulder flexor group. However, this may be accounted for by the fact that the acromiodeltoideus and spinodeltoideus are also involved in shoulder abduction [103].

Moment arms reveal a bias towards antigravity function, with the elbow extensor (Figure 2.3) and wrist flexion and ulnar deviation (Figure 2.4) moment arms greater than their antagonists. At the elbow (Figure 2.3), the moment arms of Biceps Brachii (BBI) and Triceps Brachii Longus (TBG) follow the sinusoid expected from their simple path, and the mean maximum moment arm of TR is 153± 8% that of BBI. Wrist flexor moment arms varied substantially through the range of motion, with greatest moment arms at full wrist extension (Figure 2.4a), and decreased as flexion angle increased. Wrist extension moment arms were nearly constant through the range of motion. The deviation moment arms of ECR and FCU decreased slightly with ulnar deviation (Figure 2.4b), while those of ECU and FCR remained constant. The maximum moment arms of BBI and TBG, occurring approximately midway between their ranges, are large. The fiber length to moment arm ratio of BBI (3.1) is twice that of TBG (1.5) meaning that it can achieve greater ranges of motion necessary for rapid elbow flexion.

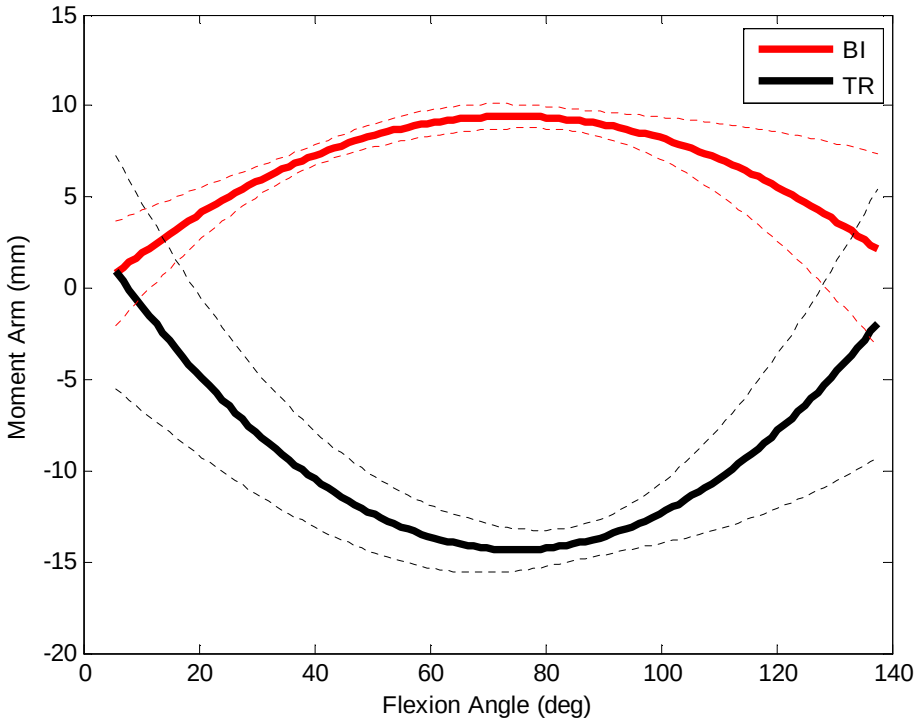

Figure 2.3. Average moment arm (±SD) of elbow flexion-extension motion. The bands represent the mean moment arms with corresponding standard deviations across all 8 specimens.

(a)

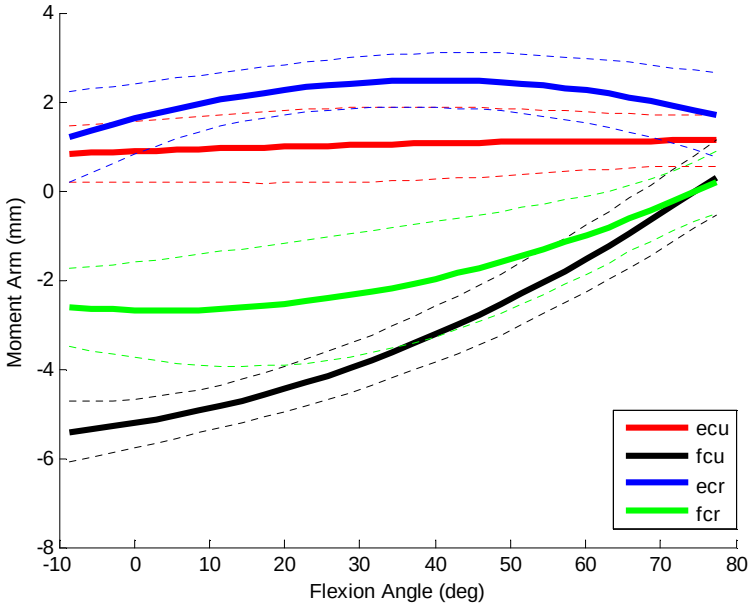

(b)

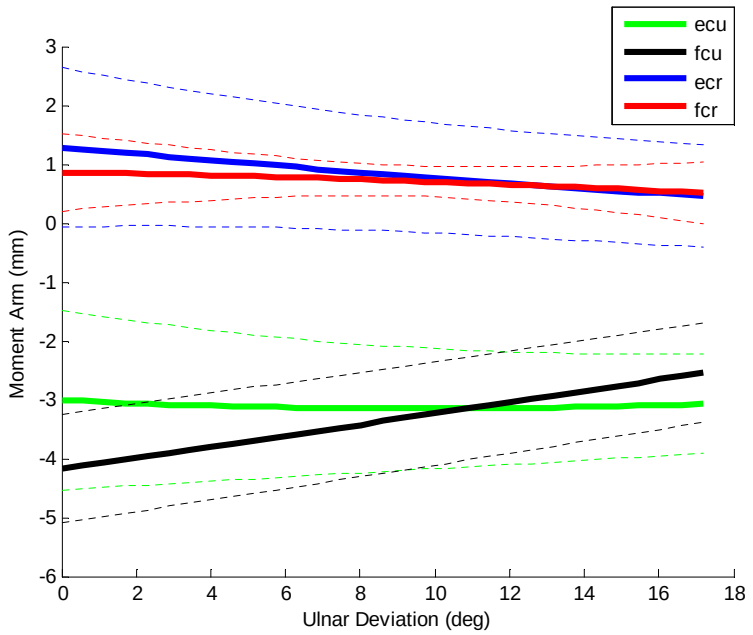

Figure 2.4. Average moment arm (±SD) of wrist (a) flexion-extension motion; (b) radio-ulnar motion. The bands represent the mean moment arms with corresponding standard deviations across all 8 specimens.

2.4 Discussion

Attachments, architecture and moment arms were measured for muscles of the domestic cat forelimb. These data were examined for evidence of functional specializations analogous to those reported in hindlimbs, and serve as the foundation for a computational model presented in the next chapter. A comparison with corresponding data for the hindlimb revealed that, although the general proximal-distal gradient of muscle size was preserved, the muscles of forelimb functional groups displayed much greater heterogeneity.

Studies performed on the ankle joint of the cat [105] demonstrated a somewhat sinusoidal relationship for muscles with large moment arms in the flexion-extension plane, similar to what was observed in the elbow muscles in this study. The other muscles possessed moment arm / joint angle slopes that were fairly flat or shallowly positive without crossing the moment arm axis. Similar behavior was again observed for the wrist muscles. However, inversion-eversion and adduction-abduction plots of ankle moment arms showed negative slopes crossing the neutral positions on both axes. This behavior, which was not observed in the wrist, provided intrinsic stability to the limb [105]. While the wrist muscles studied may not actively work to stabilize the limb, the FCU in particular does decrease its moment arm in ulnar deviation, thereby helping to decrease the available torque at the joint. In contrast with the ankle, this action may not actively stabilize the limb, but it does decrease its instability. Thus, the ankle behavior in the hindlimb is different from that of the wrist in the forelimb. Interestingly, the behavior observed in the wrist has been shown in experiments involving the human wrist [101]. In both cat and human wrists, the ECR, FCR and ECU muscles showed little to no change

while the FCU exhibited decreasing moment arm with increasing ulnar deviation. In neither case did the moment arms cross the neutral axes. However, the behaviors differed in flexion. The cat's wrist flexors decrease their moment arm thereby decreasing instability and the extensors remain unchanged. In the human wrist, the flexors increase their moment arms and the extensors decrease theirs, effectively increasing instability. It is the action of muscle force and tendon compliance which help generate torque profiles that, in some cases, promote stability [101]. This flexion-extension difference between the wrists may be due to the different limits of the joints under question. While the unconstrained human wrist has an approximately 90° range of motion in both extension and flexion, the cat forelimb only extends to about 10° past neutral position. This anatomical restriction may influence moment arm behavior.

Role in Locomotion

Some significant architectural differences were also noted between forelimb and hindlimb that affect locomotion. Previous work examined the same characteristics in the greyhound [68], dogs specialized for straight-line sprinting. This specialization was inferred from an equal distribution of muscle mass between the forelimbs and hindlimbs and from distal tendons too short and stiff to contribute to elastic energy storage. Unlike the greyhound, the forelimb mass in the cat is just over 60% of the hind limb, with distal tendons shorter than the hindlimb's, indicating a bias for power production from the hindlimb and a tendency towards a stiffer, more strut-like forelimb. The extensor-flexor balance at equivalent forelimb and hindlimb joints also favors limb extension and propulsive forces more strongly in the hindlimb. Considering the shoulder and knee as

functionally equivalent [82], the tension generating capacity of the flexors and extensors are similar for the shoulder and for the knee (Figure 2.5).

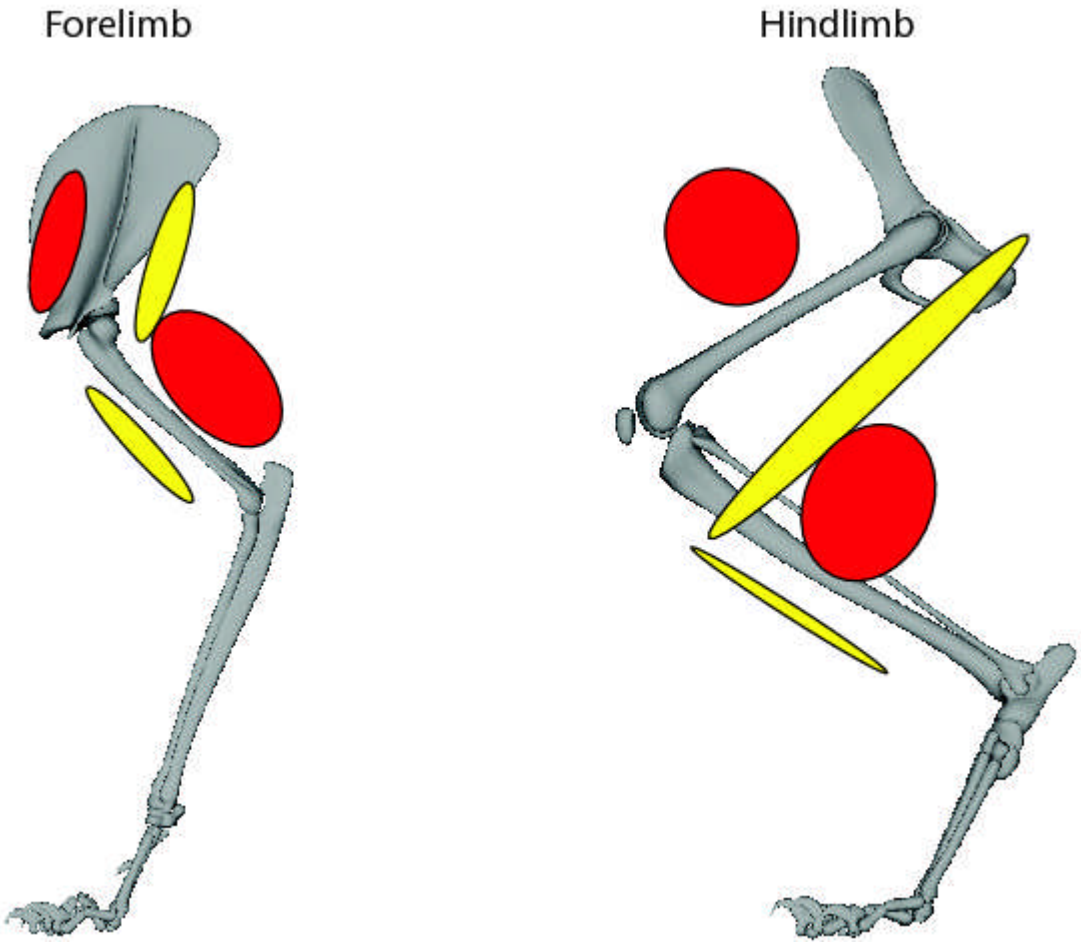

Figure 2.5. Comparison of forelimb and hindlimb functional capacity. Each ellipse area represents the sum of functional group PCSA from the present study or from Sacks & Roy [61]. The length of the bone-directed axis represents the average fascicle length from that group. For semitendinosus, proximal and distal fascicle lengths were added; for the elbow flexors, the length is a mass-weighted fascicle length average, to minimize distortion due to the unique brachioradialis.

The total PCSA of the shoulder flexors is 80% of that of the extensors and total PCSA of the knee flexors essentially the same as that of the knee extensors. In contrast, the total PCSA of the elbow flexors is only 24% of that of the elbow extensors, and total PCSA of the ankle flexors only 15% of that of the ankle extensors. At the elbow the average moment arm of the flexors is 66% of the extensors, and the average moment arm of the ankle flexors is 39% of that of the extensors. It is important to remember that the most powerful shoulder muscles originate from the spine and ribs and were excluded from this analysis. The similarities of PCSA between antagonists at the shoulder and knee reflect the demands for rapid acceleration and deceleration of the limbs in both directions during locomotion. The greater PCSA, longer moment arms of antigravity muscles at the elbow and ankle, and shorter distal limb tendons support the functions of weight support and limb stiffness.

Role in Turning

The muscles with the greatest force-generating capacity in the shoulders are not the extensors or flexors, as one would expect if propulsion was the main purpose. The most powerful muscles are the adductor subscapularis (308 N) and abductor infraspinatus (199 N), suggesting an adaptation for out of plane motion as would be needed to initiate turning. Note that the stopping power of the elbow extensor triceps brachii longus (270N) falls between these two, but is closer to that of the adductor, which has been related in comparative studies in the hare to that animal's capacity for rapid turning [69]. While the adductors and abductors initiate the turning and stabilize the limb in the non-sagittal plane, the equally massive triceps longus stabilizes the limb vertically and

prevents it from collapsing under the influence of the high ground reaction forces produced during this sudden action. Studies in the cheetah [106], have indicated that this animal possesses high mass (relative to their counterparts) digital flexors capable of digging into the ground to facilitate the task of performing high-speed maneuvers. The specific muscles cited, palmaris longus and flexor digitorum profundus, are also high PCSA muscles in the cat (2.36±0.61 cm^2 and 3.97±1.07 cm^2, respectively).

Role in Manipulation

Apart from directional changes, the forelimb also performs manipulatory tasks such as reaching. As a group the wrist flexors are second in force-generation (323 N) only to the elbow extensors (415 N), two-thirds of which is provided by TBG. Not only would this be useful for assisting in braking, but also in subduing prey (pronation and wrist flexion), as well as drawing them in (supination and wrist flexion). The flexor carpi ulnaris possesses a PCSA of 3.3±0.31 cm^2, and so can generate forces comparable to the aforementioned palmaris longus and flexor digitorum profundus. These wrist flexors, together with the pronators and supinators, permit the cat to carry out these manipulation tasks, which can be included as part of the overall goal of target reaching. Muscle synergies based on muscles being active during the same period were obtained during a target reaching task in cats [107]. Synergy 1 represented the raising of the paw from the surface and involved the shoulder flexors teres major and spinodeltoideus and the forearm pronator muscle pronator teres. Synergy 2 involved limb flexion carried out by shoulder flexor acromiodeltoideus and elbow flexor brachialis. Synergy 3 was the transport of the limb towards the target and involved the shoulder flexor

acromiodeltoideus, elbow flexor and forearm supinator brachioradialis and wrist extensor extensor carpi radialis. Synergy 4 represented the preparation for contact with the target and was produced by shoulder flexor spinodeltoideus, elbow flexor and forearm supinator brachioradialis and wrist extensors extensor carpi radialis, extensor digitorum longus and extensor digitorum communis. Synergy 5 reflected the target press and involved the elbow extensor triceps brachii longus and wrist flexor palmaris longus. An analysis by mass (Figure 2.6a) reveals a significant use of massive muscles during the limb lift (Synergy 1) and target press (Synergy 5). When initially examined from the point of view of PCSA (Figure 2.6b), high power muscles are active during four of the five synergy stages. However, high PCSA muscle use is most prominent during target press (Synergy 5), less so during flex and transport (Synergy 2,3) in which acromiodeltoideus played the main role, and even less so limb lift (synergy 1). Taken together with the mass results, the most massive and highest force generating muscles are employed during target press. The large muscles employed in limb lift and transport have lower PCSAs, indicating that these stages do not require as much power, and as a consequence, lower metabolic cost to produce. An analysis by optimal fascicle length (Figure 2.6c) reveals a clear, significant use at the end of transport and preparation for contact (Synergy 3, 4). The prominent muscles were brachioradialis, an elbow flexor and wrist supinator, and extensor carpi radialis, a wrist extensor. This result would suggest a need for quick but small forearm supination and extension of the paw as the limb closes in on the target.

Finally, examination of pennation angle (Figure 2.6c) also demonstrates a clear, significant use of the highly pennate acromiodeltoideus during the flex and transport phase (Synergy 2,3). This result suggests that this muscle, not the most massive and not

used to provide speed, may actually be playing a role in providing stability of the shoulder during transport.

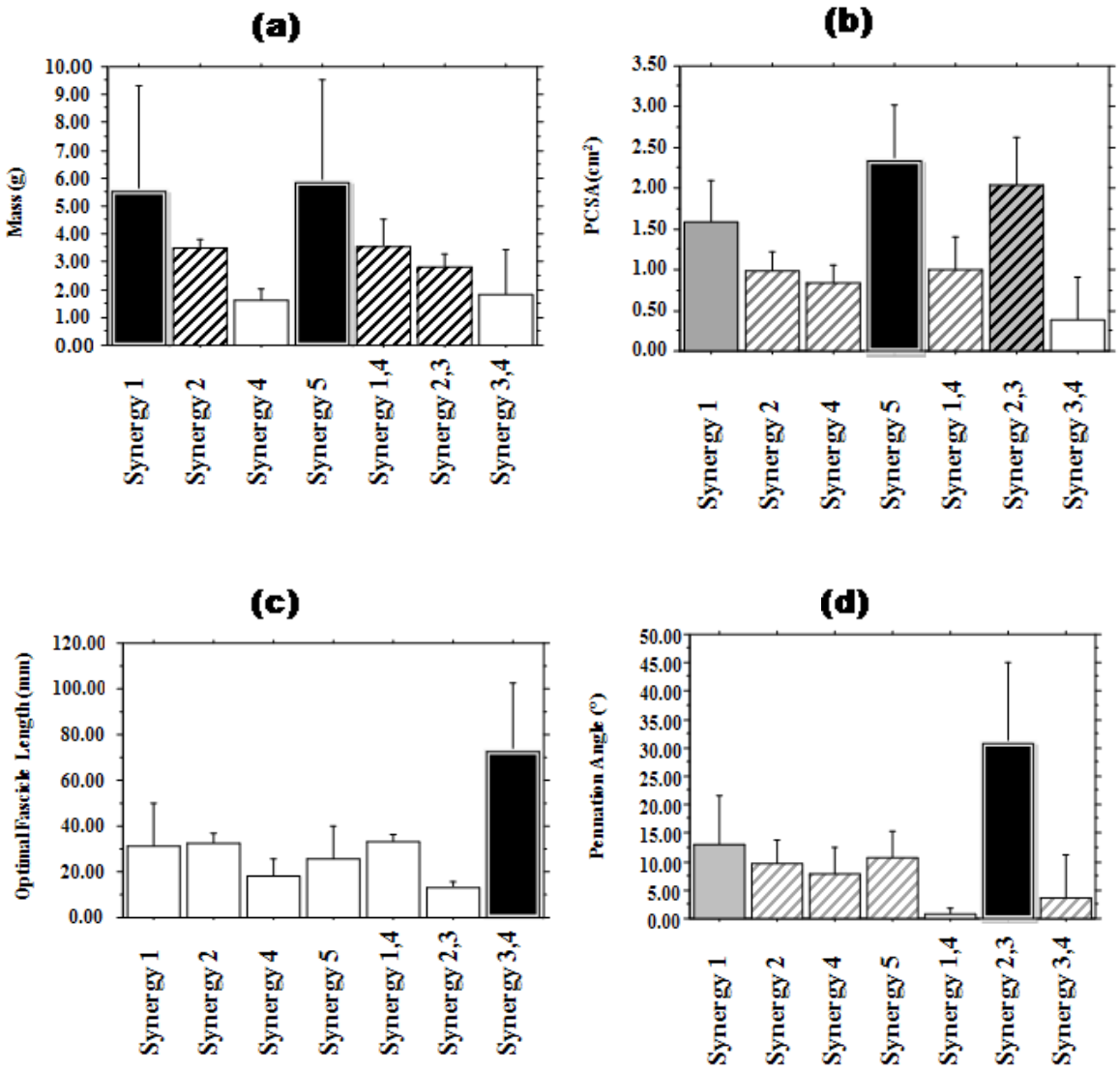

Figure 2.6: Histograms showing (a) the average mass, (b) the average physiological cross-sectional area (PCSA), (c) optimal fascicle length, (d) pennation angle, by synergies during reaching (Yakovenko et al. 2006). The bars represent 1 standard deviation. Bars sharing a common color (black: high, grey medium, open low) were statistically indistinguishable ($p > 0.05$).

Taken together, the analysis indicates that (i) the cat uses massive, but not necessarily highest metabolic cost muscles to lift the limb; (ii) maintains the shoulder stable as it flexes the elbow and begins to transport the limb toward the target; (iii) quickly turns and extends the wrist as the limb approaches the target; and (iv) engages large, powerful muscles (elbow extensor and wrist flexors) to press down on the target.

Possible Neural Correlates of Function

The basis for the forelimb's extended repertoire of movements as compared to the hindlimb has been posited to be the difference in neural wiring between the forelimb and hindlimb. While the hindlimb has simple, balanced bi-directional Ia connections restricted architecturally according to agonist-antagonist groups and functionally by flexion extension, the forelimb has more complex neural wiring, across the shoulder and wrist, that span functional groups [5, 15]. This allows the nervous system to take advantage of the muscles that perform similar but slightly varied actions, owing to their mechanical advantage, to provide the greater flexibility of movement that is required in manipulatory tasks. For example, in a food retrieval task in which EMGs were recorded [5], it was found that the extensor carpi ulnaris performed the task of wrist and digit extension, along with extensor carpi radialis and extensor digitorum communis, at the termination of retrieval. It later is dissociated from the other two muscles and forms a synergy with triceps medialis and its flexion-extension antagonist flexor carpi ulnaris during paw placement. Of special note are Ia projections from most of the elbow muscles as well as wrist extensors and flexors like ECR and FCR onto the forearm muscles supinator and pronator teres. The muscles provide powerful supination and pronation –

rotation of the forearm about its long axis – motions which the hindlimb is essentially incapable of performing. In the distal limb SUP and PRT are highly specialized, low-mass muscles with short, highly pennated fascicles that provide high forces needed for prey retrieval and suppression, respectively.

In summary, the musculoskeletal anatomy and moment arms of the cat forelimb have been quantified. These results have been compared to those of the hindlimb, as well as other species, to establish functional implications. In the forelimb, functional grouping is not the principal organizing structure. The limb does retain some of that specialization insofar as the neural and muscle architecture of the elbow joint being similar to that found in the hindlimb. However, even this correspondence is present in a diminished form. Although the proximo-distal gradient with respect to muscle mass is conserved in the forelimb, it has been found to be less specialized for the role of propulsion as is the case of the hindlimb. Indeed, it has been found that the greater heterogeneity of the architecture of the forelimb confers greater flexibility of motion that is manifested in its ability to initiate directional change and manipulate objects or prey.

CHAPTER 3:

MUSCULOSKELETAL MODEL IMPLEMENTATION

3.1 Introduction

Biomechanics, in part, aims to understand how the architecture and geometry affect motor function. However, the experiments required to fully explore the desired systems and their interactions may not be possible [108, 109]. Musculoskeletal models have been developed to address this issue. Computational models have been used, among other things, to determine joint torques generated during a specified task [28], in clinical gait analysis [110] and in orthopedics [111] with the goal of assessing treatment options. The domestic cat has been a mainstay of biomechanics research for many years [4, 8, 9, 61, 105, 112], but the use of a model can help to advance the studies of motor behavior. To date, only a hindlimb model has been constructed [26] and, given that it has been demonstrated that there are structural and functional differences present in the forelimb, a corresponding computational model needs to be constructed.

In choosing implement any model, the constraints that one wishes to impose on the system needs to be addressed. A rigid body represents an idealization of a solid body in that the body does not expand nor contract, bend nor fracture when acted upon by an external force [113, 114]. Since the effects of deformation do not have to be modeled the analysis of the body's motion is simplified. A rigid body can translate and rotate in three-dimensional space and so possesses six degrees of freedom. The movement can be described by a set of three non-coplanar 'basis' vectors. Reference frames define these basis vectors within Cartesian space and so set the basis vectors mutually perpendicular

to each other. The reference frame can be external to the body or attached to it, in which case it moves with the body.

Translation can then be described by a vector with respect to the xyz reference frame. Rotation transforms a body from one basis set to another, and a body's new orientation can be described by its rotation about the x, y and z axes. These rotations can be represented in the form of matrices, where the rotation about x (R_x), y (R_y) and z (R_z) is given by

$$R_x(\theta) = \begin{bmatrix} 1 & 0 & 0 \\ 0 & \cos\theta & -\sin\theta \\ 0 & \sin\theta & \cos\theta \end{bmatrix}, R_y(\theta) = \begin{bmatrix} \cos\theta & 0 & \sin\theta \\ 0 & 1 & 0 \\ -\sin\theta & 0 & \cos\theta \end{bmatrix}, R_z(\theta) = \begin{bmatrix} \cos\theta & -\sin\theta & 0 \\ \sin\theta & \cos\theta & 0 \\ 0 & 0 & 1 \end{bmatrix}.$$

Euler rotations are commonly used to represent the orientation of a rigid body [113]. Essentially, rotation of a body through the sequence z-y-x about the angles $\alpha, \beta, and\ \gamma$ respectively can be obtained by the following:

$$R = R_x(\gamma)R_y(\beta)R_z(\alpha).$$

Euler angles and rotation matrices possess orthonormal properties that facilitate biomechanical analyses [114]. The rows and columns of orthonormal matrices are each normal, that is, they have a vector magnitude of 1. Furthermore the row and columns are mutually orthogonal. These attributes confer additional properties on rotation matrices, namely that a rotation matrix is equal to its transpose and the matrix inverse is also equal to the transpose. These attributes are useful in algorithms to determine kinematics [115, 116].

The rigid bodies comprising the cat forelimb are connected by physical structures that constrain their relative motion. It is common practice to model these constraints as mathematically rigorous constraints on the equations of motion, which reduces segmental

modeling to discovering the kinematic constraints that allow sufficiently accurate mimicry of observed motions.

The goal of this study is to implement a three-dimensional musculoskeletal model of the cat forelimb, utilizing a rigid body frame onto which a muscle model, incorporating kinematic and muscle architecture data, is attached. Particular use is made of moment arm measurements to further refine and validate the model.

3.2 Theory

3.2.1 Limb Kinematics

To mathematically determine the kinematic parameters, there are several methods available for calculation of joint centers and hence segment lengths [115, 117-119]. Each of these methods requires *a priori* definition of the kinematic structure connecting the rigid bodies. We explored a few for our task.

The first method, which will be referred to as Reuleaux method [120, 121], consists of the transformation of the sensor (position of marker connected to body) coordinates of one segment into the reference frame of the other link. The motion of the sensors would, depending of the type of joint, produce arcs or surfaces to which mathematical parameters could be fit to obtain the centroid or axis of rotation. The bone lengths can then be inferred as the inter-axis distance.

The second method, referred to as statistical estimation, utilizes an extended Kalman filter to estimate the global position and orientation of the limb and its joint angles [118]. The algorithm also uses the motion capture data to estimate the limb

lengths and motion capture marker positions and orientations. All quantities that are to be estimated are represented as state variables.

The third method, named articular surface fitting [122], attempts to perform a least-squares fit of geometric shapes such as spheres or cylinders to 3D point data. This uses our assumption that the anatomical joints can be described as being spherical or hinge in nature.

3.2.2 Modeling

The model platform employed, Neuromechanic, is a simulated physical environment designed to analyze and test the control of biomechanical systems [123]. Neuromechanic employs rigid body equations of motion, various muscles models, and multilayer neural networks, to determine, among other parameters of interest, muscle and joint states, and system stability. The platform is an on-going developmental project being implemented by Dr. Nate Bunderson, a post-doctoral fellow, in our research laboratory, and Jeff Bingham, a collaborating graduate student.

Using Neuromechanic [123], a skeletal model was constructed using rigid body mechanics. The model was composed of 5 rigid body segments (scapula, humerus, ulna, radius, and paw) with 7 degrees of freedom across 4 joints. There were 3 dofs at the shoulder (spherical joint), 1 at the elbow (hinge), 1 between the radius and ulna (hinge), and 1 at the wrist (hinge). This last consisted of a spherical joint at the radius with a 2 dof constraint imposed at the ulna to paw joint.

Once the skeletal frame was defined, the actuation model design was chosen. The type of muscle model used depends heavily on the scientific or engineering goal one

wishes to accomplish. Within the biomechanics field two types have become prominent: biophysical models and phenomenological models.

Biophysical models are those based on the attachment and detachment of myosin cross-bridges to actin [124, 125]. The most prevalent of these are the Huxley-type models [125], which attempt to determine the fraction of an assumed fixed number of active, independent cross-bridges that are bonded to actin at a given time and with a specific range of cross-bridge displacement. The models are attractive because they are mathematical descriptions of the sliding filament theory, the current theory of how muscles contract [126]. Thus, they connect the chemistry, mechanics and structure of muscle in order to estimate the forces in cross-bridges [33, 127-129]. Biophysical models tend to be employed in the movement studies to predict the coordination of muscles during the performance of a task based on energy minimization principles [130-132]. The muscle dynamics, however, require the integration of multiple differential equations, which carries a high computational cost when one wants to model multi-muscle forces. The models also usually involve the incorporation of many parameters that are difficult to ascertain experimentally [133]. Furthermore, they do not incorporate history-dependent properties such as the enhancement of a stimulated muscle's force if the muscle has just been stretched or the force depression if the muscle was shortened [134].

Phenomenological models represent an alternative implementation of studying muscle behavior. Unlike biophysical models, they do not attempt to explain the processes underlying muscular energetics, but seek to reproduce the external behavior in response to some input [133]. One type, employed in multiple-muscle models, is the

Hill-type model [31]. Models of this type contain two core elements: (i) a "series-elastic element" that relates the muscle length to the instantaneous muscle force and (ii) a "contractile element" that relates the muscle's instantaneous speed of shortening and lengthening to the instantaneous muscle force, thereby characterizing the system's external behavior There is considerably more data available for the few parameters required by the model [133], which is generally used to determine how the force generated by single muscles affect the entire musculoskeletal system [135]. This muscle model uses only one differential equation per muscle, making it more computationally tractable. However, the equation treats the muscle activation, force-length and force-velocity characteristics of muscles as independent parameters, and so fails to capture the interaction dynamics common at low activation rates. Furthermore, it does not accurately depict history-dependent effects [136] nor yielding [51]. In addition, it does not incorporate a physiological mechanism, such as cross-bridge energetics, as the Huxley models do. In spite of this, Hill models have been shown to describe, both qualitatively and quantitatively, the force response of muscle undergoing stretch [57, 65]

Distribution-Moment models are an approach which seeks to approximate the cross-bridge formulations in order to yield more computationally tractable solutions [137]. The model maintains its biophysical soundness by retaining the Huxley model and including calcium-activation dynamics and electrical stimulation models. It has been shown to produced macroscopic properties such as force and stiffness, and has displayed good agreement with experimental data such as the force-velocity relation in response to constant velocity shortening or stretch [34]. However, the model is still much more complex than the Hill-type with non-linear equations requiring the measurement of

chemical, mechanical, structural and thermodynamic parameters for each muscle. Furthermore, simplifying assumptions such as non-pennate fibers that cross the entire length of the muscle and uniform sarcomeres restrict the use of the model [138].

Continuum or constitutive models are another type of phenomenological model, which are based on the relationships between the stresses and strains (constitutive relations) of a particular material [139]. Continuum models seek to compensate for the limitations of one-dimensional models in modeling complex muscle behavior within a three-dimensional framework that depends on the activation level, fiber strain and strain rate [140], and are based on the concept that muscles transfer forces in both longitudinal and transverse directions [141, 142]. In fact, muscle fiber behavior has been described as transversely isotropic in that its constitutive properties are symmetric about the long axis (fiber direction) [143]. This knowledge is useful in simplifying the relational matrix describing the stress-strain properties and so facilitates analysis. Because continuum models, unlike Hill-type or biophysical models, are three-dimensional they can be used to more fully represent the complex geometry of muscles [144], and to simulate surgical procedures (Keeve et al 98) and impact biomechanics [145]. . Different muscles may perform differently during a task [146, 147] and so the separate muscles of a system must be characterized. Characterization of such a material requires testing of the tissue under longitudinal extension, transverse extension, and longitudinal shear. Progress is hampered, however, by the dearth of experimental studies examining the material properties of skeletal muscle tissue [148, 149]. Additionally, as a type of phenomenological model, it does not incorporate information at the cellular level and so suffers the same issues as the Hill-type model in this regard. Furthermore, continuum

model are unable to fully address shifts in the mechanical output owing to physiological changes e.g. fatigue [135].

The goal is to eventually explore behaviors such as postural stability and locomotion and how they may be affected by phenomena such as length and force feedback, as well as influences imposed by the spinal and supraspinal complexes. This aim falls within a more macroscopic or system scope than a microscopic or physiological one and so the use of the Hill-type model is appropriate. This muscle model does not explain the processes of muscle contraction dynamics involving cross-bridge energetics, but may provide future insight at a system level incorporating whole muscle mechanics and neural behavior.

The musculotendon complex was designed using a variation of a Hill model [57], composed of an inelastic tendon in series with a muscle fiber. The muscle fiber has a parallel arrangement of a contractile and elastic element. The force produced by an individual muscle can be represented by the function

$$F^m(t) = \cos\varphi\ (\ a(t)F_a(\dot{l})F_a(l) + F_p(l) + \ \eta\frac{\dot{l}}{v_0^m})\ F_o^m,$$

where $F^m(t)$ is the muscle-fiber force, φ the pennation angle, $a(t)$ the muscle activation, $F_a(\dot{l}\ )$ the normalized active velocity-dependent fiber force, $F_a(l)$ normalized active length-dependent fiber force, $F_p(l)$ the normalized passive length-dependent fiber force, η the passive damping coefficient, $\dot{l}$ the fiber shortening velocity, v_0^m the maximum shortening velocity, and F_o^m the maximum isometric muscle-fiber force. Thus, the model makes use of the force-length and force-velocity relationships and the activation dynamics to estimate the force generated by each muscle.

The 29 muscles examined during the previous phase of experiments were incorporated and positioned point to point (origin, via, insertion) in accordance with their recorded attachments. Briefly, parameters such as muscle mass, muscle length and pennation angle were directly measured from cadaver dissections. Fiber length and sarcomere length were used to derive attributes such as the optimal fiber length and the physiological cross-sectional area (PCSA) [61], from which maximum contractile force was calculated [150]. The active force-length, passive force-length, and active force-velocity curves [55, 57, 58] were modeling by interpolated splines. Furthermore, moment arms, which vary with angle, were calculated as the ratio of tendon excursion to the joint angle, both obtained using the tendon displacement method [100].

3.3 Methods

3.3.1 Architectural and Anatomical Characterization

The right forelimb was harvested from six female, adult cats (*Felis domesticus*) weighing 4.5-5.5 kg (Liberty Research, Inc., Waverly, NY). These animals had been sacrificed as part of unrelated studies involving only the hindlimbs. All research was conducted in compliance with Georgia Institute of Technology IACUC protocols for the study of vertebrates and adhered to the legal requirements of the United States of America. The limb was skinned, disarticulated at the scapula, and 2 mm Steinman bone pins inserted into the scapula, humerus, ulna, radius and paw. In four of these specimens reflective marker triads were mounted on each of the bone pins (Figure 3.1). Using a Vicon motion-capture system (Vicon Motion Systems, CO, USA), kinematic data were obtained as the limb was manipulated in 3-D space, with special

attention paid to moving each joint. Data were collected at 100 Hz during 4-6 trials of approximately 10 seconds for each specimen. Data were post-processed by labeling the markers during each data frame. Some data sets were excluded if markers from segments were obscured and thus not recorded by the motion capture system. In addition, in some trials, single joints were moved while the others were held motionless. Only the joints moved in isolation were used for later kinematic analysis.

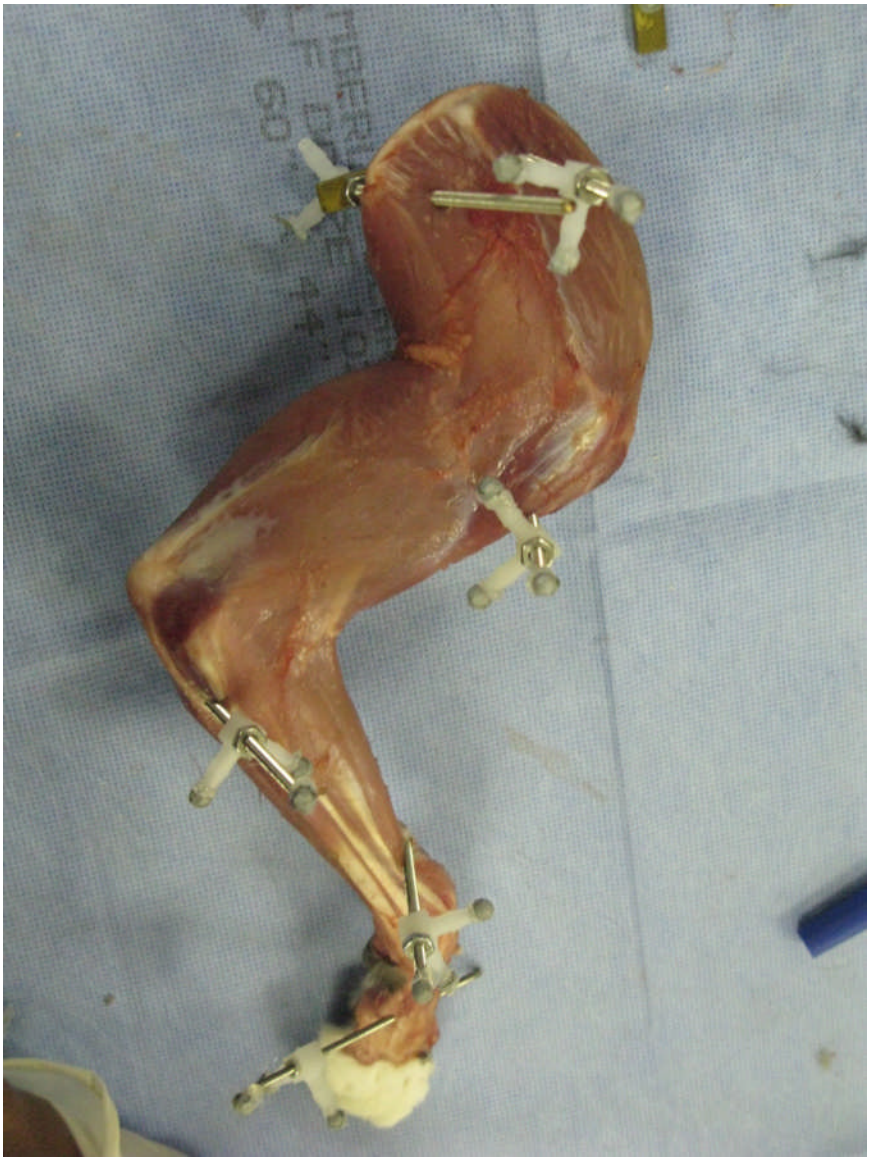

Figure 3.1: Bone pins and reflective marker triads.

All six specimens were immobilized in a stance-like position using a framework of brass bars attached to the bone pins (Figure 3.2). To further stabilize the structure, the limb was fixed by immersion in 4% buffered paraformaldehyde for 2-4 weeks. Following chemical fixation, the limb was rinsed in phosphate buffered saline and stored in the same solution at 4º C during digitization. To record anatomical data, each specimen was suspended on a rigid stand within the workspace of a 5-axis digitizer (Microscribe MX, Solution Technologies, Oella, MD). Anatomical data, such as muscle origin, insertion and via points, were obtained using a 5-axis Microscribe digitizer. For broad attachment points, the center was taken. The location of bone pin ends and the kinematic triads were recorded.

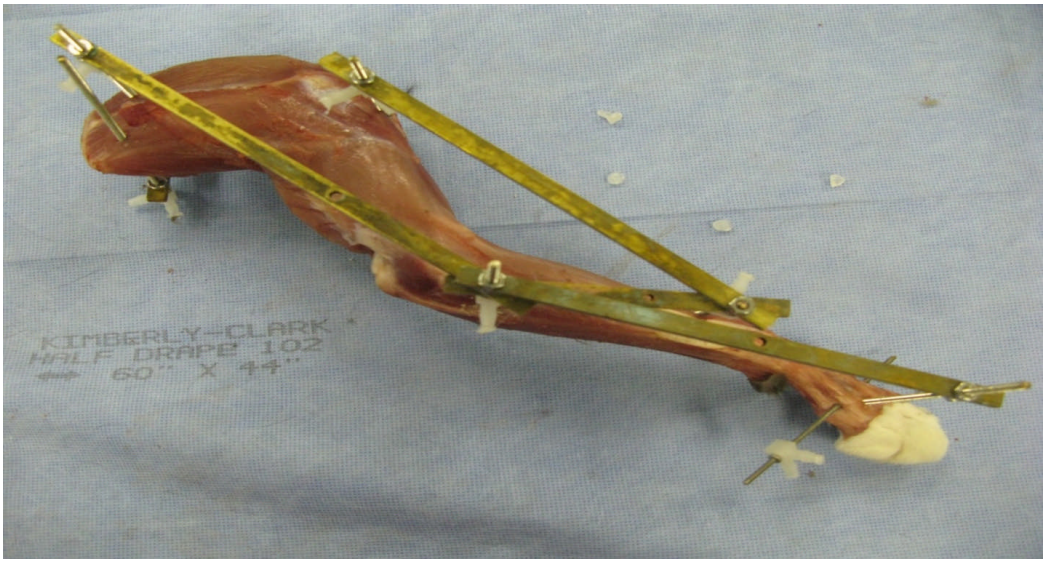

Figure 3.2: Stabilizing crossbar framework.

The position of each POI was recorded at least 5 times, with the specimen removed from the suspension frame between recordings. Because superficial muscles obscured the POI of deeper muscles, superficial muscles were carefully dissected after

their attachments were fully recorded. In a typical specimen, complete recording of all muscle POI required 6-8 layers of dissection, resulting in 30-40 digitizing sessions. Because the location and orientation of the specimen in the digitizer coordinate system was not consistent between digitizing sessions, a specimen-specific coordinate system was derived from the bone pin reference points. These points are consistent and measured in each digitizing specimen, and were used to define an equiform transformation [116] to align sessions to a common coordinate system. Repeated recordings of each POI were averaged within this common coordinate system to determine the per-specimen data set. Later analysis revealed that some of the markers had shifted position during the transfer from the motion capture experiments to the digitization leading to kinematics that were not consistent with the anatomy. These data were excluded from further analysis.

Bony landmarks were also recorded, with the specimen being re-positioned in the suspension frame before each of the 5 recording sessions. These landmarks are reference points on the animal's skeleton that can be used in situating the model-reconstructed muscles, and in making inter-specimen analyses. They include the caudal and ventral angles of the scapula, acromion process, humerus greater tubercle, medial epicondyle, lateral epicondyle, olecranon process, radial head, ulna styloid process, radio-ulnar space, radial styloid process, base of first toe, medial metacarpophalangeal joint, and lateral metacarpophalangeal joint (Figure 3.3a&b). Because these points were recorded along with the markers, they can be reconstructed, by equiform transformation, with their corresponding muscles. Furthermore, the registration

of these points allowed us to combine the multiple specimens into a single average forelimb.

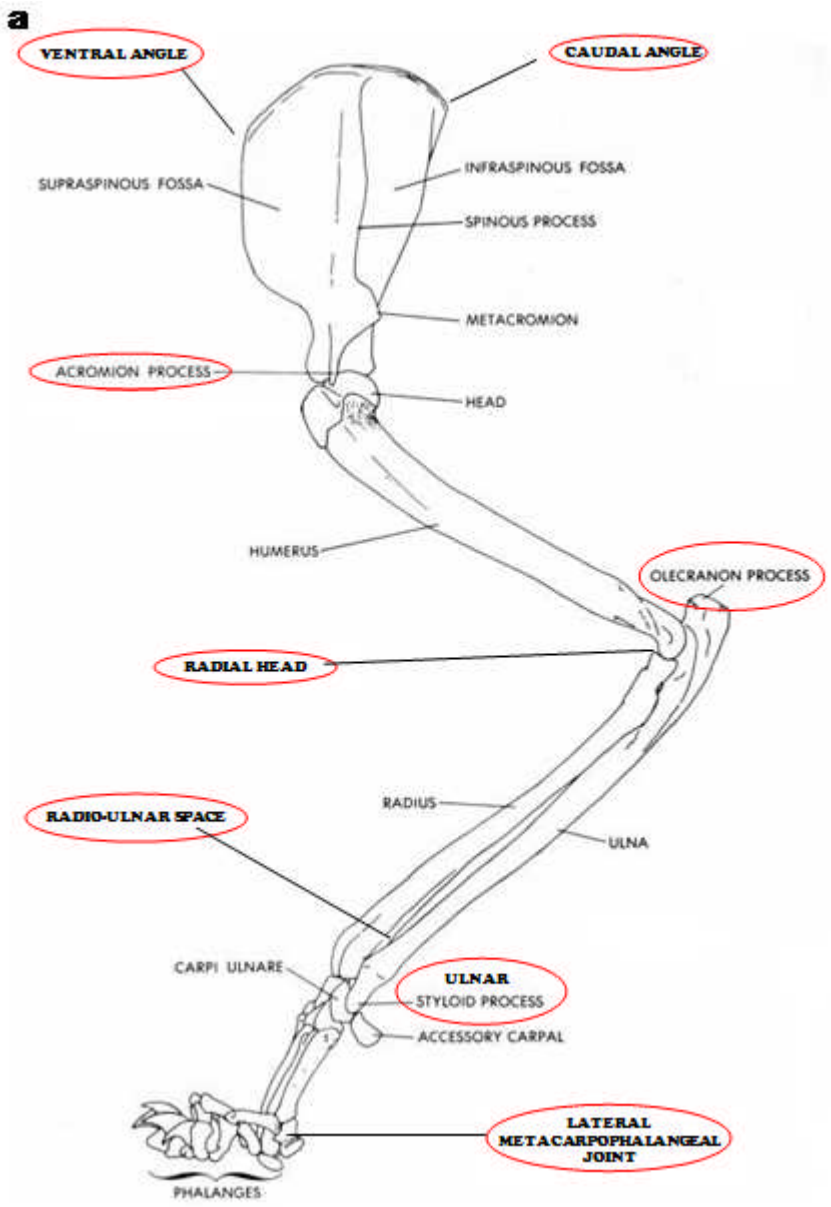

Figure 3.3a. Skeletal anatomical points. (a) Lateral view. Encircled names indicate the points for which the positions were recorded.

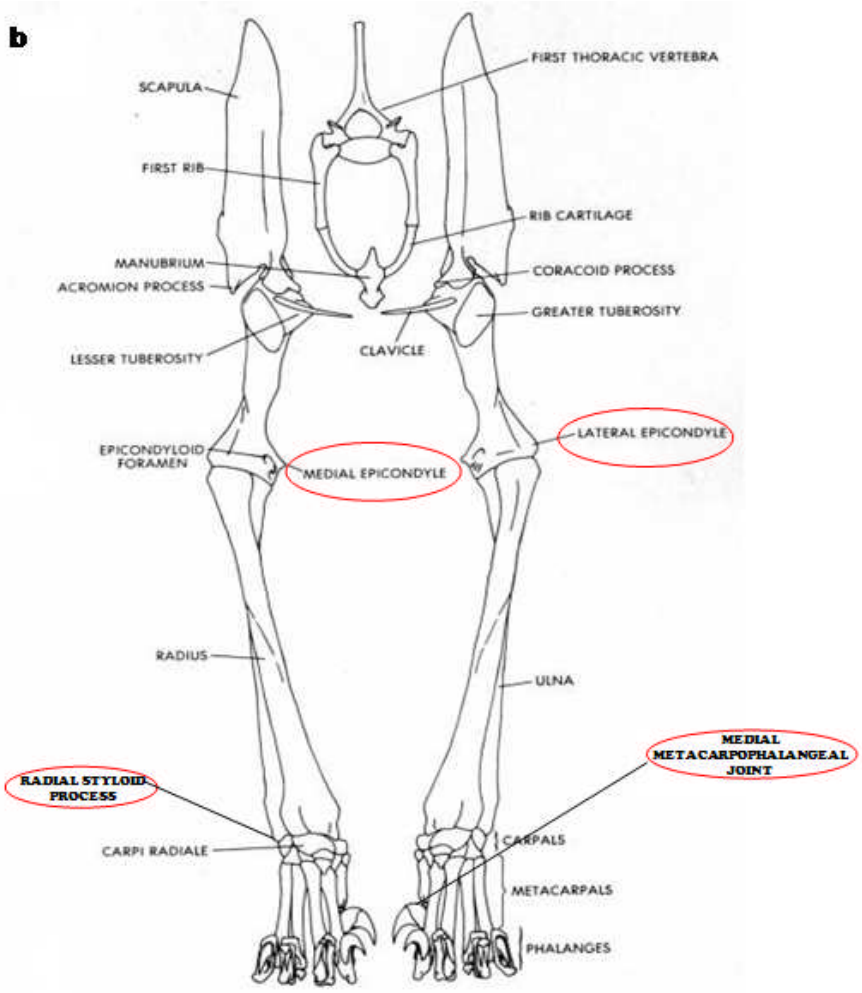

Figure 3.3b. Skeletal anatomical points. (b) Frontal View. Encircled names indicate the points for which the positions were recorded.

3.3.2 Limb Kinematics

3.3.2.1 Statistical Estimation

The algorithm requires a description of the system in the form of a kinematic tree, which is then mapped to matrix. The kinematic tree consists of segments connected via joints. The segments can be actual limb segments, 'dummy' segments that allow for combination of basic joints, or 'virtual' segments such as sensors. Joints represent the spatial transformation from the parent's reference frame to that of the child. There are four type of joints described : (1) Sliding (S), which is 1 degree of freedom translation, (2) Translation (T), for 3D translation, (3) Hinge (H), for rotation about a specific axis, and (4) Rotation (R) about any axis. Figure 3.4 displays the forelimb as a structure of linked rigid bodies (right) and the corresponding kinematic tree (left). The segments of the tree are enclosed in rectangular boxes and the joints within circles. With respect to the joints the letters represent the aforementioned joint types and any subscript the specific direction.

The kinematic tree is then transformed into table (Table 3.1) form. Parent Segment is ancestor or segment from which current segment originates. Joint Type is the transformation from which segment originates. The code is defined from the corresponding number given in the joint type description. Sensor Type is the classification of the sensor and the code which gives the transformation/dof of the sensor. This also uses the joint type code to describe the degree of freedom. Joint Axis represents the axis through which confined joints (H, S) operate, where x – 1; y – 2; z – 3.

Joint Category defines whether the joint is a varying (1) or constant (2) parameter. To illustrate, if we examine the elbow joint, which was defined as a hinge joint, and the

axis of rotation was chosen as the z-axis, then the angle about this axis is a varying parameter while the angles about the x- and y-axes are constant parameters. The numbered codes to the right of each entry in the table constitute the elements of an Nx5 matrix (where N is the number of segments) that is given as input to the supplied algorithm [118].

Initial standard deviations for position and angle states that are allowed to vary and those that remain constant are specified by the programmer. The same is done for the position and angle drift states, that is, how quickly the states are expected to change, as well as the sensor noise standard deviation. These are used by the algorithm to make covariance matrices.

The drift and sensor noise covariances do not change throughout the algorithm. The initial position covariance, however, represents the first prior, which is used, along with the sensor values to get the posterior or new value for the covariance. Thus the value one chooses for the constant values is particularly important since it expresses the confidence in the estimate. Making the value too large, however, will allow the algorithm the make large changes based on little data. Thus, for our example of the elbow, since we have initial measures for our constant parameters, we could make the initial covariance small in comparison to that of the variable parameter. As the algorithm updates these parameters in an attempt to better fit the data it will constrain the constant humerus length and rotations about x and y so that they vary very slowly from time step to time step. In contrast, the variable z-axis angle will be allowed to vary much more in order to provide a better fit. The lengths of the segments were measured, with vernier calipers, to get the necessary initial estimates (Table 3.2).

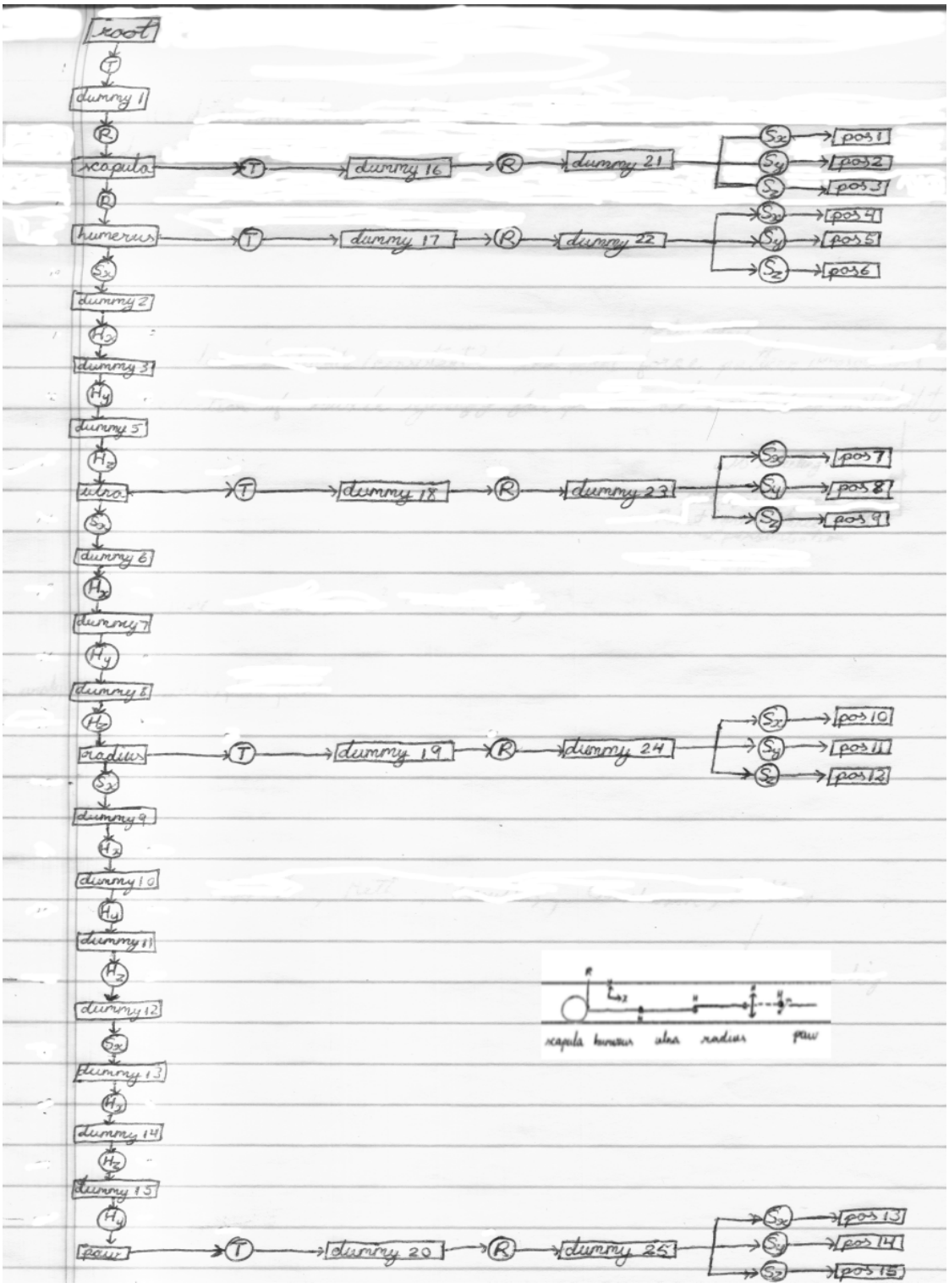

Figure 3.4: Kinematic Tree. The kinematic tree illustrates the definition of the segments and joints of the model limb displayed on the right.

Table 3.1: Tabular representation of kinematic tree and its characteristics.

Segment Name (#)	Parent Segment	Joint Type	Sensor Type	Joint Axis	Joint Category
root (1)	none (0)	none (0)	none (0)	none (0)	none (0)
dummy 1 (2)	root (1)	T (2)	none (0)	none (0)	varying (1)
scapula (3)	dummy 1 (2)	R (4)	none (0)	none (0)	varying (1)
humerus (4)	scapula (3)	R (4)	none (0)	none (0)	varying (1)
dummy 2 (5)	humerus (4)	S (1)	none (0)	x (1)	constant (2)
dummy 3 (6)	dummy 2 (5)	H (3)	none (0)	x (1)	constant (2)
dummy 5 (7)	dummy 3 (6)	H (3)	none (0)	y (2)	constant (2)
ulna (8)	dummy 5 (7)	H (3)	none (0)	z (3)	varying (1)
dummy 6 (9)	ulna (8)	S (1)	none (0)	x (1)	constant (2)
dummy 7 (10)	dummy 6 (9)	H (3)	none (0)	x (1)	constant (2)
dummy 8 (11)	dummy 7 (10)	H (3)	none (0)	y (2)	constant (2)
radius (12)	dummy 8 (11)	H (3)	none (0)	z (3)	varying (1)
dummy 9 (13)	radius (12)	S (1)	none (0)	x (1)	constant (2)
dummy 10 (14)	dummy 9 (13)	H (3)	none (0)	x (1)	constant (2)
dummy 11 (15)	dummy 10 (14)	H (3)	none (0)	y (2)	constant (2)
dummy 12 (16)	dummy 11 (15)	H (3)	none (0)	z (3)	varying (1)
dummy 13 (17)	dummy 12 (16)	S (1)	none (0)	x (1)	constant (2)
dummy 14 (18)	dummy 13 (17)	H (3)	none (0)	x (1)	constant (2)
dummy 15 (19)	dummy 14 (18)	H (3)	none (0)	z (3)	constant (2)
paw (20)	dummy 15 (19)	H (3)	none (0)	y (2)	varying (1)
dummy 16 (21)	scapula (3)	T (2)	none (0)	none (0)	constant (2)
dummy 17 (22)	humerus (4)	T (2)	none (0)	none (0)	constant (2)
dummy 18 (23)	ulna (8)	T (2)	none (0)	none (0)	constant (2)
dummy 19 (24)	radius (12)	T (2)	none (0)	none (0)	constant (2)
dummy 20 (25)	paw (20)	T (2)	none (0)	none (0)	constant (2)
dummy 21 (26)	dummy 16 (21)	R (4)	none (0)	none (0)	constant (2)
dummy 22 (27)	dummy 17 (22)	R (4)	none (0)	none (0)	constant (2)
dummy 23 (28)	dummy 18 (23)	R (4)	none (0)	none (0)	constant (2)
dummy 24 (29)	dummy 19 (24)	R (4)	none (0)	none (0)	constant (2)
dummy 25 (30)	dummy 20 (25)	R (4)	none (0)	none (0)	constant (2)
pos 1 (27)	dummy 21 (26)	S (1)	pos (2)	x (1)	constant (2)
pos 2 (28)	dummy 21 (26)	S (1)	pos (2)	y (2)	constant (2)
pos 3 (29)	dummy 21 (26)	S (1)	pos (2)	z (3)	constant (2)
pos 4 (30)	dummy 22 (27)	S (1)	pos (2)	x (1)	constant (2)
pos 5 (31)	dummy 22 (27)	S (1)	pos (2)	y (2)	constant (2)
pos 6 (32)	dummy 22 (27)	S (1)	pos (2)	z (3)	constant (2)
pos 7 (33)	dummy 23 (28)	S (1)	pos (2)	x (1)	constant (2)
pos 8 (34)	dummy 23 (28)	S (1)	pos (2)	y (2)	constant (2)

Table 3.1 continued

pos 9 (35)	dummy 23 (28)	S (1)	pos (2)	z (3)	constant (2)
pos 10 (36)	dummy 24 (29)	S (1)	pos (2)	x (1)	constant (2)
pos 11 (37)	dummy 24 (29)	S (1)	pos (2)	y (2)	constant (2)
pos 12 (38)	dummy 24 (29)	S (1)	pos (2)	z (3)	constant (2)
pos 13 (39)	dummy 25 (30)	S (1)	pos (2)	x (1)	constant (2)
pos 14 (40)	dummy 25 (30)	S (1)	pos (2)	y (2)	constant (2)
pos 15 (41)	dummy 25 (30)	S (1)	pos (2)	z (3)	constant (2)

Table 3.2: Segment Lengths. Bone lengths were measured with vernier calipers for all specimens.

Specimen	Scapula	Humerus	Radius	Paw (mcp 3)
Cat 1	66.53	94.85	88.40	30.88
Cat 2	72.57	103.87	93.00	35.88
Cat 3	72.22	101.60	93.52	32.32
Cat 5	72.78	100.51	90.60	32.70
Cat 6	73.09	100.70	93.96	35.32
Cat 7	70.38	95.56	90.65	32.90

3.3.2.2 Reuleaux Method

The algorithm, which was originally developed for planar motion, states that if two points each attached to a rigid body are in motion relative to each other, the center of rotation is the point of intersection of the bisectors of the translation vectors defined by each point's original and final positions [120, 121]. This model assumes that two bodies are connected by a single, rotational degree of freedom. Generalized to 3-dimensional space, the determination of axes of rotation is the intersection of the planes normal to the translation vectors [117, 120]. This model assumes that two bodies are connected by purely rotational degrees of freedom, and requires the investigator to determine whether

that connection has one, two, or three degrees of freedom. In our case, we have chosen to model the shoulder as a spherical joint and the others as revolute joints.

3.3.2.3 Articular Surface Fitting

This method fits surfaces rather than points. It was implemented because surface with low curvature were encountered, which caused the Reuleaux method to diverge. The surface fitting method described here is supposed to be robust against divergence caused by decreasing curvatures. Thus, it was expected that it would produce equal or better results than the Reuleaux method.

Given three-dimensional points p_i, for i=1, ..., m, that define a surface s, one can define a function, d, as the "true" distance of any point $p_i \in R^3$ from that surface [122]. The supposition is then made that

$$d(s, p_i) = \frac{g - h^2}{2h} \tag{2.1}$$

where g and h are two positive continuously differentiable functions dependent on s and $p_i \in R^3$. If $d(s,p_i)=0$ then the surface goes through all the points. For experimental data, one can find the least-square fit by minimizing $\sum_{i=1}^{m} d(s, p_i)^2$.

Sphere Fitting

To fit a spherical surface s, the 'true' distance of any point p to the surface of the sphere is given as

$$d(s, p_i) = \frac{k}{2}(|p|^2 - 2\rho\langle p, n\rangle + \rho^2) + \rho - \langle p, n\rangle,$$

where 1/k is defined as the sphere radius, ρn is the closest point of the sphere to the origin that is not its center, n is parameterized in polar coordinates as

$$n = (\cos\varphi \sin\theta\,, \sin\varphi \cos\theta\,, \cos\theta),$$

and $\langle p, n\rangle$ is the dot product of p and n. Once these parameters are found, via non-linear optimization, the center can be found as

$$center = \left(\rho + \frac{1}{k}\right) n.$$

Cylinder Fitting

The distance function for a right circular cylinder is given as follows:

$$d(s, p_i) = \frac{k}{2}(|p|^2 - 2\rho\langle p, n\rangle - \langle p, a\rangle^2 + \rho^2) + \rho - \langle p, n\rangle,$$

where, again, 1/k is defined as the sphere radius, ρn is the closest point of the cylinder to the origin, with |n| = 1, a is the direction of the cylinder axis, and n is perpendicular to a ($\langle n, a\rangle = 0$). As in the case of the sphere, non-linear optimization to determine these parameters yields the solution for the center as

$$center = \left(\rho + \frac{1}{k}\right) n.$$

Having obtained these kinematic and anatomical parameters, we were now in a position to computationally reconstruct the musculoskeletal structure of the limb**.**

3.3.3 Model Development and Implementation

A coordinate system based on the marker triad of the parent was created per parent-child set of data for each kinematic trial and each cat. The child data was then transformed into the parent's coordinate system for the sequence of marker points. For perfect hinge and spherical joints, the transformed child's points lie on arcs and shells, respectively. The measured points were fit to arcs or shells as appropriate and the joint center and direction (for hinge joints) of the best fit were found. Using the kinematic

markers the joint information was transformed into the digitized data set (i.e. point collected with the Microscribe). Equiform transformations [116] were applied to all points (joint centers and muscle points) to align, as closely as possible, data from the different cats to a common reference frame. The mean of the points were subsequently calculated to obtain an "average cat", which was then assembled into a Neuromechanic file format along with architectural property data. Using the digitized bony landmarks the bone file polygons were aligned with the muscles. The inertia was estimated from the polygons of the bone files. During the anatomical digitization, a via point was not measured for the brachioradialis muscle. This resulted in a muscle that projected outside of the body of the limb, which would result in a very large and erroneous moment arm. To eliminate this issue, a via point for this muscle was added in the model. This was chosen as the intersection of the initial line of action from the origin and the final line of action leading to the insertion, which placed the via point ~5mm anterior to the brachialis insertion.

Subsequent modifications were made to optimize the joints based on the data. The elbow joint location and direction was allowed to vary within the bounds ±5mm and ±5° to obtain the best match with experimental data. The radial-ulnar joint direction was permitted to deviate by ±4° to get the best fit for the wrist moment arms in supinated and pronated postures. The wrist joint location and direction was allowed to vary within ±5mm and ±10° to obtain best agreement with experimental data. To obtain a more physiological range of muscle responses, the limb was put into four postures that matched data from a locomoting cat [151] and the tendon slack length adjusted so that the maximum fiber length to resting length ratio in any of the Prilutsky postures is 1.05

[152]. Length feedback gains were then incorporated using data obtained from Ia monosynaptic recordings [153].

3.4 Results

3.4.1 Limb Kinematics

A time course of the performance of the statistical estimation algorithm is shown in Figure 3.5a. This time course is actually the motion capture frame number as the algorithm updates its parameters. It is reconstructing the limb lengths, which are constant parameters with which it was initialized (Table 3.2). Since the initial variance on the constant parameters were not set to zero, but a small value (e.g. 1), the constants are still allowed to slowly vary as it converges to the optimal values. It will also vary (slowly) as the more rapidly changing variable parameters are adjusted to more closely fit the data.

In this scenario the humerus is within 5mm of the length. The ulna is approximately 20mm too long, and the radius, a component of which is attached at the radio-ulnar joint (radius 1) and another attached to the wrist joint (radius 2), are more than 50 mm too short. It is expected that the distance between the joint centers may differ somewhat from the actual measured bone lengths. Taking the humerus as an example, because the measurements were made at the condyles and the centers of rotation would actually be within the core of the condyles, the axis-to-axis length may be shorter by up to 10 or 15mm. The radius, on the other hand, possesses no such protrusions and so would be expected to produce a length close to that found using joint centers.

The coordinates of the Vicon measured positions, as well as the algorithm estimate, are shown for two marker triads (Table 3.3). Errors on the order of 10s of cm

are observed. Attempts were made to correct the problem by using this "training" data to initialize a new data set or by concatenating multiple trials to allow the algorithm more time to fit the data (Figure 3.5b&c). Just after time point 134, which was then end of the initial data set, there were discontinuities experienced for the constant parameters and the values at the end of the run are different from those of the first training set. Table 3.4 shows the mean squared errors between the centroid of the markers at time points surrounding the discontinuity at 134. The errors suddenly decrease but then gradually increase again. These errors demonstrated that statistical algorithm failed in the reconstruction of the limb.

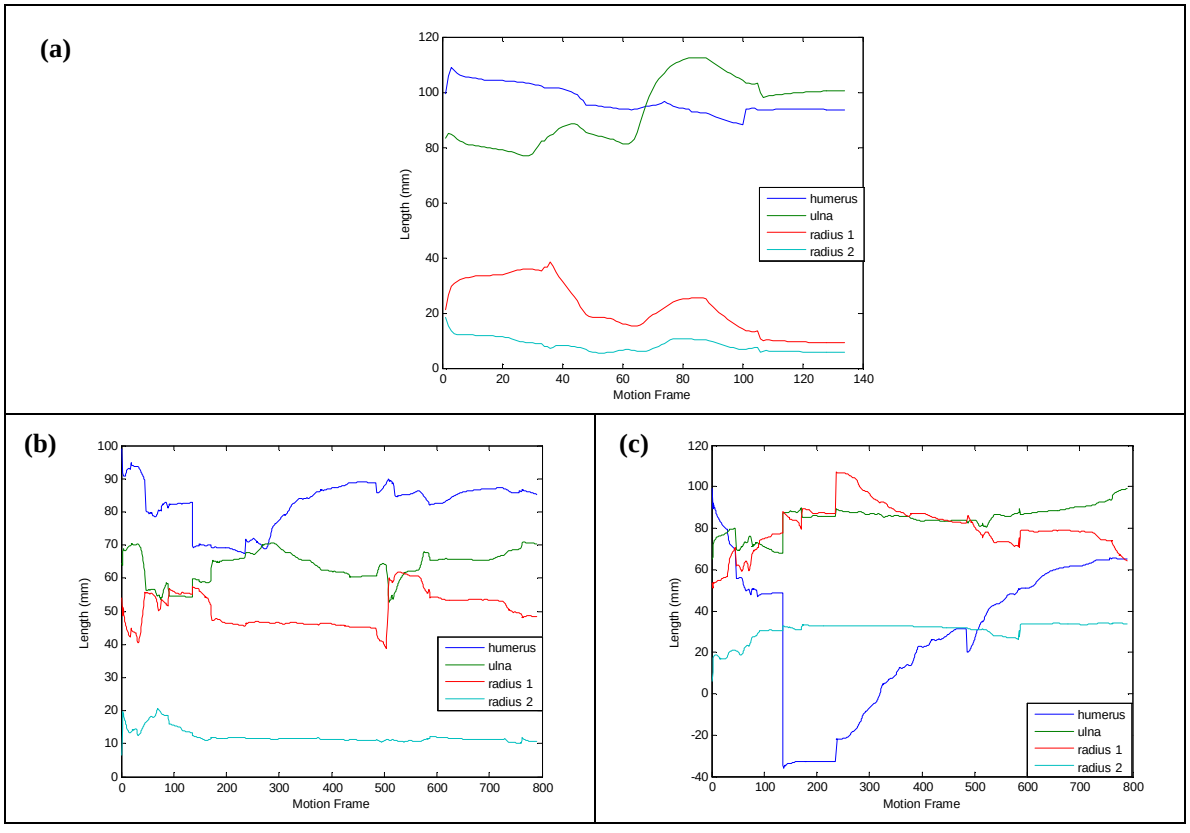

Figure 3.5: Iterations of statistical estimation algorithm. (a) Progression of fit for limb segments. (b) and (c) Progression of fits for concatenated data.

Table 3.3: Example of positions of raw data and statistical algorithm estimates over sequential frames.

	Data MKA			Data MKB			Fit MKA			Fit MKB	
X (mm)	Y (mm)	Z (mm)	X (mm)	Y (mm)	Z (mm)	X (mm)	Y (mm)	Z (mm)	X (mm)	Y (mm)	Z (mm)
-68.5	312.7	248.8	-26.9	307.0	257.0	-18.1	-26.7	8.2	27.0	11.3	38.0
-75.9	318.3	252.6	-35.3	315.5	265.1	-18.0	-27.0	7.8	27.3	11.0	37.5
-94.8	355.2	245.8	-60.9	358.5	270.7	-17.6	-30.4	7.0	28.2	10.6	37.2
-94.8	354.4	243.9	-61.0	358.1	269.8	-19.1	-30.3	9.9	31.1	4.8	41.5
-94.6	354.3	242.7	-60.8	357.9	268.6	-20.6	-29.9	11.7	30.5	1.4	42.2
-94.0	353.3	243.0	-60.0	356.7	268.6	-20.6	-30.4	12.2	30.5	1.5	41.6
-93.8	353.3	243.2	-59.7	356.6	268.7	-20.6	-30.5	12.5	30.3	1.4	41.2
-93.4	353.4	243.6	-59.2	356.7	269.0	-20.6	-30.6	12.8	30.2	1.4	41.0
-93.0	353.3	244.1	-58.7	356.5	269.2	-20.6	-30.6	13.1	30.1	1.3	40.9
-92.7	352.8	244.5	-58.2	356.0	269.4	-20.5	-30.6	13.4	30.0	1.3	40.8
-92.6	352.2	244.8	-57.8	355.4	269.5	-20.5	-30.6	13.6	29.9	1.3	40.8
-92.2	352.0	245.0	-57.4	355.0	269.4	-20.5	-30.6	13.8	29.8	1.3	40.7
-91.9	351.7	245.1	-56.7	354.5	268.6	-20.5	-30.6	14.0	29.8	1.2	40.7
-91.6	351.4	245.3	-56.2	354.3	268.7	-20.5	-30.5	14.1	29.7	1.2	40.7
-91.3	351.0	245.6	-56.1	353.8	269.6	-20.6	-30.5	14.2	29.6	1.2	40.7
-91.1	350.3	245.9	-55.9	353.2	269.6	-20.6	-30.5	14.3	29.6	1.2	40.7
-91.0	349.8	246.0	-55.7	352.7	269.8	-20.6	-30.5	14.4	29.5	1.2	40.7
-90.8	349.4	246.2	-55.4	352.2	269.8	-20.5	-30.4	14.5	29.5	1.2	40.7
-90.5	349.3	246.4	-55.2	352.1	269.9	-20.6	-30.4	14.5	29.5	1.2	40.7
-90.2	349.2	246.6	-54.5	351.9	270.0	-20.6	-30.4	14.6	29.4	1.2	40.7
-89.6	349.1	247.1	-53.8	351.8	270.1	-20.6	-30.4	14.7	29.4	1.1	40.7
-89.2	348.9	247.4	-53.2	351.3	270.0	-20.6	-30.4	14.7	29.4	1.1	40.7
-88.7	348.7	247.7	-52.7	351.3	270.4	-20.6	-30.3	14.8	29.4	1.1	40.7
-88.4	348.7	248.0	-52.3	351.0	270.3	-20.6	-30.3	14.8	29.3	1.1	40.7
-88.1	348.5	248.2	-52.0	350.9	270.5	-20.7	-30.3	14.8	29.3	1.1	40.7
-87.9	348.4	248.4	-51.8	350.7	270.5	-20.7	-30.3	14.8	29.3	1.1	40.7
-87.7	348.5	248.6	-51.5	350.6	270.6	-20.7	-30.2	14.8	29.3	1.1	40.7
-87.5	348.4	248.7	-51.3	350.8	271.0	-20.7	-30.2	14.9	29.3	1.1	40.7
-87.3	348.4	248.9	-50.9	350.7	271.0	-20.7	-30.2	14.9	29.2	1.0	40.7
-86.9	348.1	249.2	-50.5	350.3	270.8	-20.7	-30.2	14.9	29.2	1.0	40.7
-86.5	348.2	249.4	-49.9	350.6	271.1	-20.8	-30.2	14.9	29.2	1.0	40.8
-85.6	347.8	250.1	-48.8	350.3	271.4	-20.7	-30.2	15.0	29.2	1.1	40.7
-139.5	294.8	241.3	-110.6	302.4	271.2	-23.6	-35.4	15.1	29.8	1.2	41.0
-136.7	297.0	242.7	-106.5	306.1	271.5	-23.7	-35.6	15.1	29.8	1.2	41.0
-133.8	299.8	244.4	-102.9	309.6	271.7	-23.7	-35.6	15.1	29.7	1.2	41.0
-131.7	302.4	245.7	-99.6	311.9	271.5	-23.6	-35.7	15.1	29.7	1.3	41.0

Table 3.4: MSE between the centroid of the markers.

Time Point	Marker A	Marker B	Marker C	Marker D	Marker E	Marker F
114	452.7	430.1	375.3	324.5	221.9	183.4
115	452.4	429.2	375.1	324.7	222.2	183.9
116	452.1	429.0	374.9	324.4	222.5	184.3
117	451.7	429.0	374.7	324.9	222.7	183.9
118	451.2	428.5	374.4	324.3	222.8	184.2
119	450.8	428.1	374.9	323.8	223.5	184.2
120	450.5	427.7	373.8	323.7	222.6	184.4
121	450.3	427.6	374.5	323.6	222.8	184.6
122	450.3	427.4	373.5	323.6	223.1	184.6
123	450.3	427.2	374.3	323.7	223.1	184.9
124	450.2	426.7	374.2	324.3	223.0	185.2
125	450.1	426.8	374.2	323.6	223.0	185.1
126	450.1	426.4	374.2	323.7	223.0	185.5
127	450.0	426.4	374.1	323.6	223.1	185.4
128	450.0	426.2	374.1	323.6	223.0	185.2
129	450.0	426.1	374.1	323.7	223.2	185.3
130	450.0	426.4	374.0	323.8	223.2	185.6
131	450.0	426.3	374.2	324.0	223.5	185.8
132	449.9	425.8	374.2	324.5	223.6	186.2
133	449.9	426.1	374.3	324.4	223.9	186.5
134	449.8	425.7	374.2	320.1	224.5	187.7
135	416.7	404.2	339.9	283.8	206.7	153.0
136	418.5	405.8	342.1	286.4	208.3	154.3
137	421.0	407.3	344.2	288.9	210.3	156.6
138	423.3	407.9	346.0	290.4	211.3	157.9
139	424.1	409.3	349.0	294.1	213.0	160.3
140	425.4	409.3	349.5	295.0	214.5	162.0
141	426.5	408.6	350.4	296.2	215.6	164.2
142	428.4	409.9	351.5	297.9	217.8	166.4
143	431.4	410.6	354.0	302.6	219.7	170.3
144	436.9	411.1	357.5	308.7	223.8	177.5

Reuleaux and Surface Fit Methods

Figures 3.6 and 3.7 demonstrate examples of fits of the Reuleaux method to Vicon-measured sensor data at the shoulder and elbow. Tables 3.5 and 3.6 are the corresponding data points. The same data is shown for the surface fitting method in figures 3.8 and 3.9, along with their corresponding tables 3.7 and 3.8. The data in this case show excellent overlap with most of the errors < 1mm between each of the axes of the coordinates.

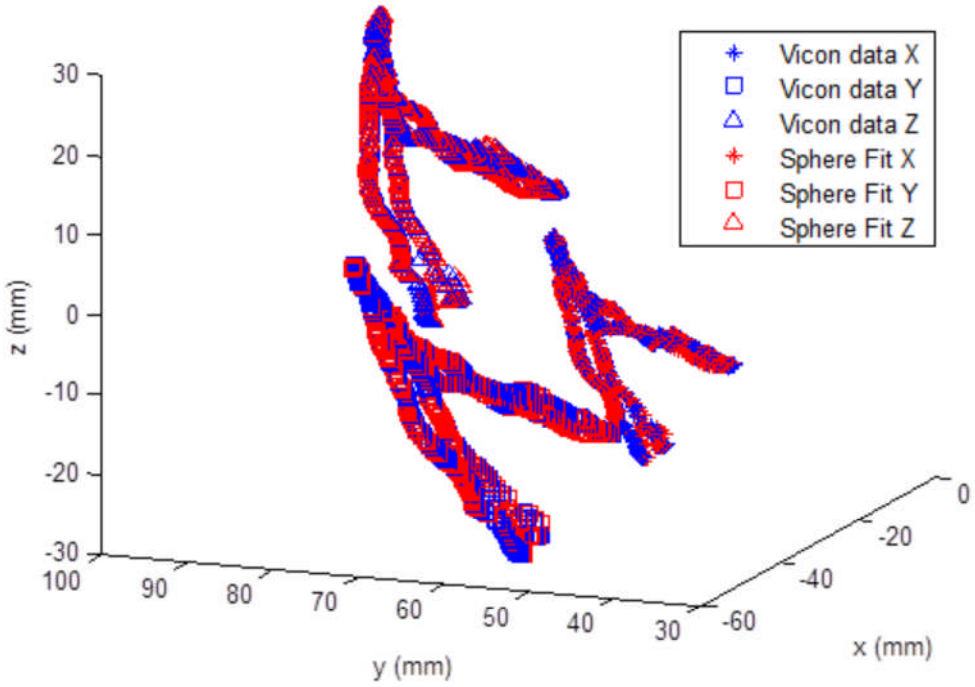

Figure 3.6: Reuleaux Fits for a Spherical Joint. Positions for a sample trial of the measured and Reuleaux fit coordinates of the three markers at the shoulder joint.

Table 3.5: Example of positions of raw data and Reuleaux estimates over sequential frames at the Shoulder Joint.

	Data MKA			Data MKB			Fit MKA			Fit MKB	
X (mm)	Y (mm)	Z (mm)	X (mm)	Y (mm)	Z (mm)	X (mm)	Y (mm)	Z (mm)	X (mm)	Y (mm)	Z (mm)
-21.5	-38.0	-30.6	61.5	74.3	79.8	-21.3	-37.9	-30.4	61.4	74.2	79.7
-21.6	-38.2	-30.8	61.4	74.2	79.7	-21.5	-38.1	-30.6	61.3	74.1	79.6
-21.7	-38.3	-30.9	61.3	74.1	79.6	-21.5	-38.2	-30.7	61.2	73.9	79.5
-21.9	-38.5	-31.1	61.1	73.9	79.4	-21.7	-38.3	-30.9	61.0	73.7	79.3
-22.1	-38.8	-31.4	61.0	73.7	79.3	-21.9	-38.6	-31.2	60.9	73.5	79.1
-22.2	-39.0	-31.6	60.9	73.5	79.1	-22.0	-38.8	-31.4	60.7	73.3	79.0
-22.3	-39.1	-31.7	60.8	73.4	79.1	-22.1	-38.9	-31.6	60.7	73.2	78.9
-22.4	-39.2	-31.9	60.7	73.2	78.9	-22.2	-39.1	-31.7	60.6	73.0	78.8
-22.5	-39.4	-32.0	60.6	73.0	78.8	-22.3	-39.2	-31.9	60.5	72.9	78.7
-22.6	-39.5	-32.3	60.5	72.8	78.7	-22.5	-39.4	-32.1	60.4	72.7	78.6
-22.8	-39.8	-32.5	60.3	72.6	78.5	-22.6	-39.6	-32.4	60.2	72.5	78.3
-22.8	-39.9	-32.7	60.2	72.4	78.3	-22.7	-39.7	-32.5	60.1	72.3	78.2
-22.9	-40.0	-32.8	60.1	72.3	78.2	-22.8	-39.9	-32.7	60.0	72.1	78.1
-22.9	-40.1	-32.9	60.0	72.1	78.1	-22.8	-40.0	-32.8	60.0	72.0	78.0
-23.0	-40.1	-33.0	60.0	72.0	78.0	-22.9	-40.0	-33.0	59.9	72.0	78.0
-23.2	-40.4	-33.3	59.8	71.8	77.8	-23.1	-40.3	-33.2	59.7	71.7	77.7
-23.3	-40.6	-33.5	59.7	71.6	77.6	-23.2	-40.5	-33.4	59.6	71.5	77.5
-23.4	-40.7	-33.6	59.5	71.4	77.5	-23.3	-40.6	-33.5	59.4	71.3	77.4
-23.6	-41.0	-33.9	59.4	71.2	77.3	-23.5	-40.8	-33.8	59.3	71.1	77.2
-23.7	-41.0	-34.1	59.3	71.1	77.2	-23.6	-40.9	-34.0	59.2	71.0	77.1
-23.8	-41.2	-34.3	59.2	70.9	77.0	-23.7	-41.1	-34.2	59.1	70.8	77.0
-23.9	-41.4	-34.5	59.0	70.7	76.9	-23.9	-41.3	-34.5	58.9	70.6	76.9
-24.2	-41.7	-34.8	58.8	70.5	76.7	-24.1	-41.6	-34.7	58.7	70.4	76.6
-24.4	-41.9	-35.0	58.8	70.3	76.6	-24.2	-41.7	-34.9	58.7	70.2	76.5
-24.5	-42.0	-35.2	58.6	70.0	76.4	-24.4	-41.9	-35.1	58.6	69.9	76.3
-24.7	-42.3	-35.6	58.5	69.7	76.2	-24.5	-42.2	-35.5	58.4	69.6	76.1
-24.8	-42.5	-35.9	58.3	69.5	76.0	-24.7	-42.4	-35.8	58.2	69.4	76.0
-25.0	-42.7	-36.1	58.1	69.3	75.9	-24.9	-42.6	-36.0	58.0	69.2	75.8

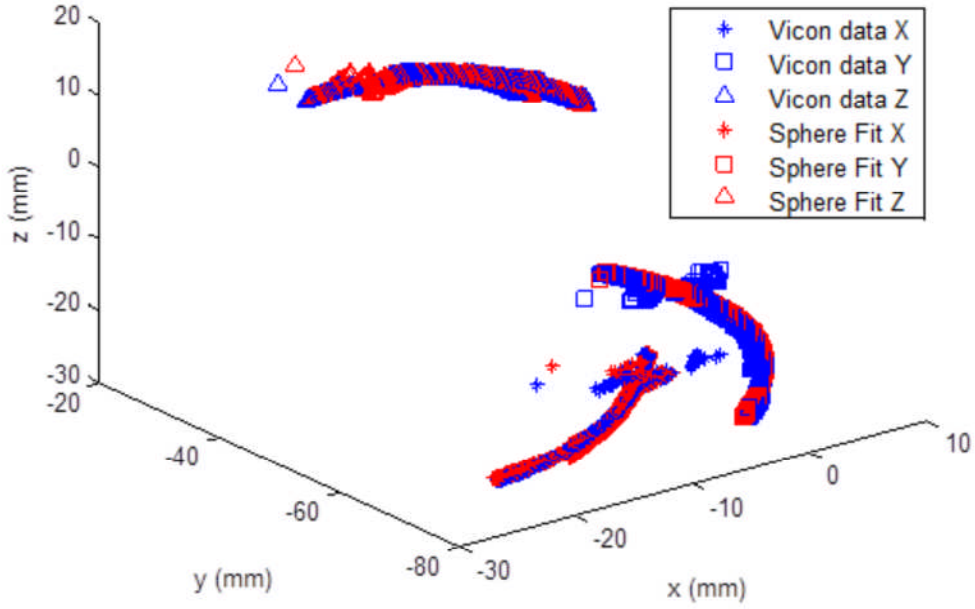

Figure 3.7: Reuleaux Fits for a Hinge Joint. Positions for a sample trial of the measured and Reuleaux fit coordinates of the three markers at the elbow joint.

Table 3.6: Example of positions of raw data and Reuleaux estimates over sequential frames at the Elbow Joint.

	Data MKA			Data MKB			Fit MKA			Fit MKB	
X (mm)	Y (mm)	Z (mm)	X (mm)	Y (mm)	Z (mm)	X (mm)	Y (mm)	Z (mm)	X (mm)	Y (mm)	Z (mm)
-18.9	1.7	-10.1	-77.1	-69.0	-54.9	-19.1	1.6	-10.2	-77.0	-69.0	-54.9
-18.7	1.8	-10.1	-77.0	-68.9	-54.8	-19.0	1.6	-10.3	-77.0	-68.8	-54.8
-18.7	1.9	-10.2	-77.0	-68.7	-54.7	-18.8	1.7	-10.4	-77.0	-68.7	-54.7
-18.5	1.9	-10.2	-77.0	-68.6	-54.6	-18.7	1.7	-10.4	-76.9	-68.5	-54.6
-18.3	2.0	-10.3	-77.0	-68.4	-54.5	-18.6	1.8	-10.5	-76.9	-68.3	-54.5
-18.3	2.1	-10.4	-77.0	-68.2	-54.4	-18.5	1.9	-10.6	-76.9	-68.2	-54.3
-18.2	2.1	-10.4	-76.9	-68.1	-54.3	-18.3	1.9	-10.6	-76.9	-68.0	-54.2
-18.0	2.2	-10.5	-76.9	-67.9	-54.2	-18.2	2.0	-10.7	-76.8	-67.9	-54.1
-17.9	2.2	-10.6	-76.8	-67.8	-54.0	-18.1	2.1	-10.8	-76.8	-67.7	-54.0
-17.8	2.3	-10.7	-76.8	-67.6	-53.9	-18.0	2.2	-10.8	-76.7	-67.5	-53.9

Table 3.6 continued

-17.7	2.3	-10.8	-76.7	-67.4	-53.8	-17.8	2.2	-10.9	-76.7	-67.4	-53.8
-17.6	2.3	-10.9	-76.7	-67.3	-53.7	-17.7	2.3	-11.0	-76.7	-67.3	-53.7
-17.6	2.3	-11.0	-76.7	-67.1	-53.6	-17.6	2.3	-11.0	-76.7	-67.1	-53.6
-17.5	2.3	-11.1	-76.6	-67.0	-53.5	-17.5	2.3	-11.1	-76.6	-67.0	-53.5
-17.6	2.3	-11.3	-76.5	-66.8	-53.4	-17.4	2.5	-11.2	-76.5	-66.9	-53.4
-17.4	2.4	-11.3	-76.5	-66.7	-53.3	-17.3	2.5	-11.2	-76.5	-66.7	-53.3
-17.2	2.5	-11.3	-76.5	-66.6	-53.2	-17.2	2.5	-11.3	-76.5	-66.6	-53.3
-17.1	2.5	-11.4	-76.4	-66.4	-53.1	-17.1	2.5	-11.3	-76.4	-66.5	-53.2
-17.0	2.6	-11.4	-76.4	-66.3	-53.1	-17.0	2.6	-11.4	-76.4	-66.3	-53.1
-16.9	2.6	-11.5	-76.4	-66.2	-53.0	-16.9	2.6	-11.4	-76.4	-66.2	-53.0
-16.8	2.6	-11.5	-76.3	-66.0	-52.8	-16.8	2.7	-11.5	-76.3	-66.0	-52.8
-16.7	2.8	-11.6	-76.3	-65.7	-52.7	-16.7	2.8	-11.6	-76.3	-65.7	-52.7
-16.6	2.8	-11.7	-76.2	-65.6	-52.5	-16.5	2.8	-11.6	-76.2	-65.6	-52.6
-16.4	2.8	-11.8	-76.1	-65.3	-52.4	-16.3	2.9	-11.8	-76.1	-65.3	-52.4
-16.3	3.0	-12.0	-76.0	-65.0	-52.2	-16.2	3.0	-11.9	-76.0	-65.0	-52.3
-16.1	3.0	-12.0	-76.0	-64.8	-52.1	-16.0	3.0	-12.0	-76.0	-64.8	-52.1
-15.9	3.0	-12.2	-75.9	-64.6	-52.0	-15.8	3.1	-12.1	-75.9	-64.6	-52.0
-15.9	3.0	-12.4	-75.9	-64.4	-51.9	-15.7	3.1	-12.2	-75.9	-64.4	-51.9

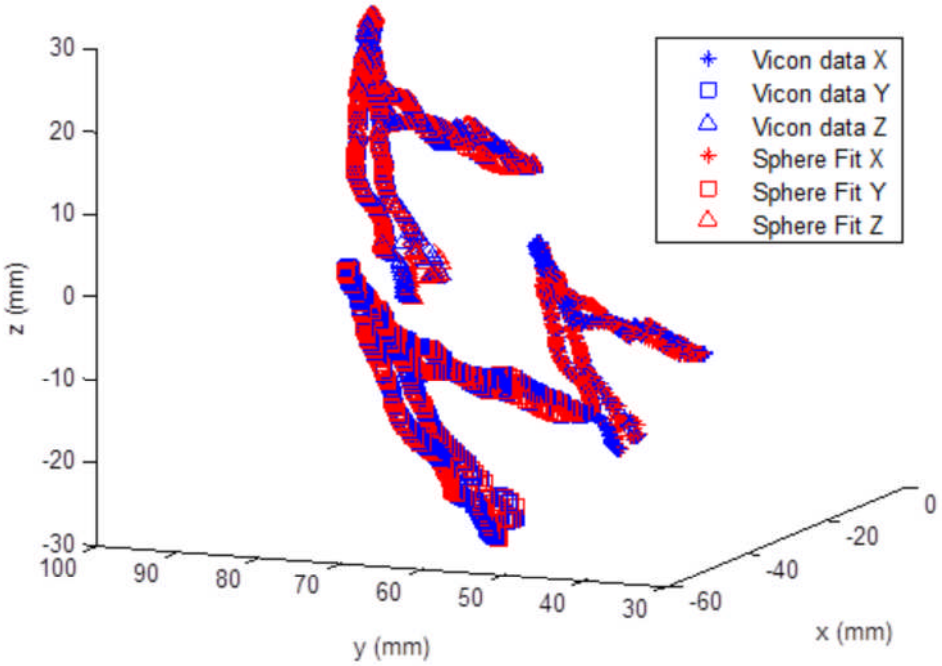

Figure 3.8: Articular Surface Fits for a Spherical Joint. Positions for a sample trial of the measured and articular surface fit coordinates of the three markers at the shoulder joint.

Table 3.7: Example of positions of raw data and Surface Fit over sequential frames at the Shoulder Joint.

	Data MKA			Data MKB			Fit MKA			Fit MKB	
X (mm)	Y (mm)	Z (mm)	X (mm)	Y (mm)	Z (mm)	X (mm)	Y (mm)	Z (mm)	X (mm)	Y (mm)	Z (mm)
-21.5	-38.0	-30.6	61.5	74.3	79.8	-21.3	-37.9	-30.4	61.4	74.2	79.7
-21.6	-38.2	-30.8	61.4	74.2	79.7	-21.5	-38.1	-30.6	61.3	74.1	79.6
-21.7	-38.3	-30.9	61.3	74.1	79.6	-21.5	-38.2	-30.7	61.2	73.9	79.5
-21.9	-38.5	-31.1	61.1	73.9	79.4	-21.7	-38.3	-30.9	61.0	73.7	79.3
-22.1	-38.8	-31.4	61.0	73.7	79.3	-21.9	-38.6	-31.2	60.9	73.5	79.1
-22.2	-39.0	-31.6	60.9	73.5	79.1	-22.0	-38.8	-31.4	60.7	73.3	79.0
-22.3	-39.1	-31.7	60.8	73.4	79.1	-22.1	-38.9	-31.6	60.7	73.2	78.9
-22.4	-39.2	-31.9	60.7	73.2	78.9	-22.2	-39.1	-31.7	60.6	73.0	78.8
-22.5	-39.4	-32.0	60.6	73.0	78.8	-22.3	-39.2	-31.9	60.5	72.9	78.7
-22.6	-39.5	-32.3	60.5	72.8	78.7	-22.5	-39.4	-32.1	60.4	72.7	78.6
-22.8	-39.8	-32.5	60.3	72.6	78.5	-22.6	-39.6	-32.4	60.2	72.5	78.3
-22.8	-39.9	-32.7	60.2	72.4	78.3	-22.7	-39.7	-32.5	60.1	72.3	78.2
-22.9	-40.0	-32.8	60.1	72.3	78.2	-22.8	-39.9	-32.7	60.0	72.1	78.1
-22.9	-40.1	-32.9	60.0	72.1	78.1	-22.8	-40.0	-32.8	60.0	72.0	78.0
-23.0	-40.1	-33.0	60.0	72.0	78.0	-22.9	-40.0	-33.0	59.9	72.0	78.0
-23.2	-40.4	-33.3	59.8	71.8	77.8	-23.1	-40.3	-33.2	59.7	71.7	77.7
-23.3	-40.6	-33.5	59.7	71.6	77.6	-23.2	-40.5	-33.4	59.6	71.5	77.5
-23.4	-40.7	-33.6	59.5	71.4	77.5	-23.3	-40.6	-33.5	59.4	71.3	77.4
-23.6	-41.0	-33.9	59.4	71.2	77.3	-23.5	-40.8	-33.8	59.3	71.1	77.2
-23.7	-41.0	-34.1	59.3	71.1	77.2	-23.6	-40.9	-34.0	59.2	71.0	77.1
-23.8	-41.2	-34.3	59.2	70.9	77.0	-23.7	-41.1	-34.2	59.1	70.8	77.0
-23.9	-41.4	-34.5	59.0	70.7	76.9	-23.9	-41.3	-34.5	58.9	70.6	76.9
-24.2	-41.7	-34.8	58.8	70.5	76.7	-24.1	-41.6	-34.7	58.7	70.4	76.6
-24.4	-41.9	-35.0	58.8	70.3	76.6	-24.2	-41.7	-34.9	58.7	70.2	76.5
-24.5	-42.0	-35.2	58.6	70.0	76.4	-24.4	-41.9	-35.1	58.6	69.9	76.3
-24.7	-42.3	-35.6	58.5	69.7	76.2	-24.5	-42.2	-35.5	58.4	69.6	76.1
-24.8	-42.5	-35.9	58.3	69.5	76.0	-24.7	-42.4	-35.8	58.2	69.4	76.0
-25.0	-42.7	-36.1	58.1	69.3	75.9	-24.9	-42.6	-36.0	58.0	69.2	75.8

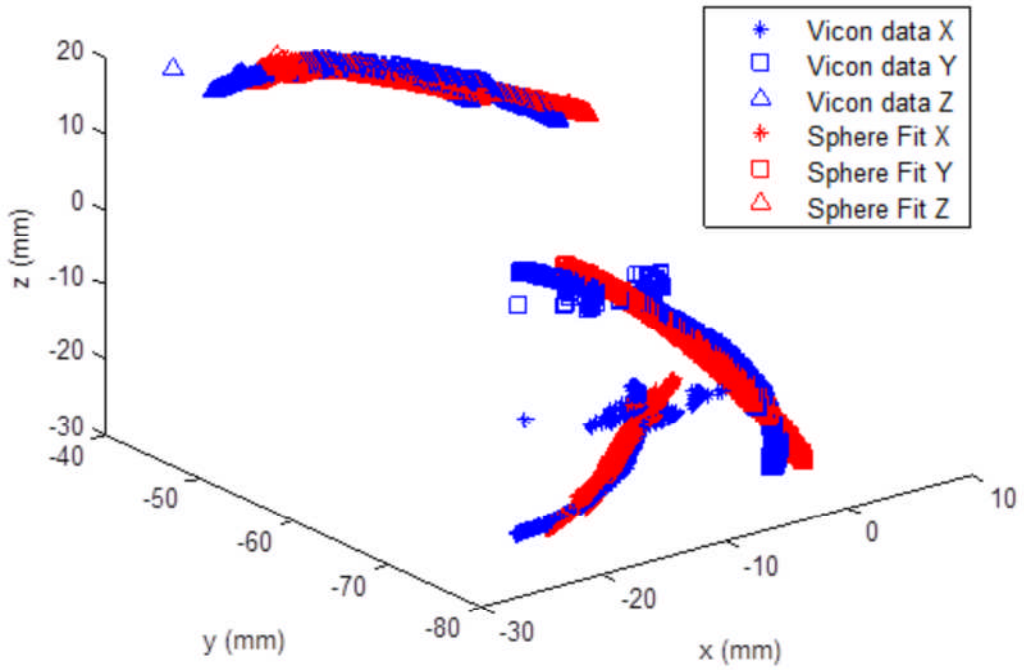

Figure 3.9: Articular Surface Fits for a Hinge Joint. Positions for a sample trial of the measured and articular surface fit coordinates of the three markers at the elbow joint.

Table 3.8: Example of positions of raw data and Surface Fit over sequential frames at the Elbow Joint.

	Data MKA			Data MKB			Fit MKA			Fit MKB	
X (mm)	Y (mm)	Z (mm)	X (mm)	Y (mm)	Z (mm)	X (mm)	Y (mm)	Z (mm)	X (mm)	Y (mm)	Z (mm)
-18.9	1.7	-10.1	-77.1	-69.0	-54.9	-19.9	0.8	-11.0	-77.0	-68.9	-54.8
-18.7	1.8	-10.1	-77.0	-68.9	-54.8	-19.8	0.8	-11.1	-76.9	-68.8	-54.7
-18.7	1.9	-10.2	-77.0	-68.7	-54.7	-19.7	0.9	-11.2	-76.9	-68.6	-54.6
-18.5	1.9	-10.2	-77.0	-68.6	-54.6	-19.6	0.9	-11.3	-76.9	-68.4	-54.5
-18.3	2.0	-10.3	-77.0	-68.4	-54.5	-19.5	0.9	-11.4	-76.8	-68.3	-54.4
-18.3	2.1	-10.4	-77.0	-68.2	-54.4	-19.4	1.0	-11.5	-76.8	-68.1	-54.3
-18.2	2.1	-10.4	-76.9	-68.1	-54.3	-19.3	1.0	-11.6	-76.8	-68.0	-54.1
-18.0	2.2	-10.5	-76.9	-67.9	-54.2	-19.2	1.0	-11.6	-76.7	-67.8	-54.0
-17.9	2.2	-10.6	-76.8	-67.8	-54.0	-19.1	1.1	-11.7	-76.7	-67.6	-53.9
-17.8	2.3	-10.7	-76.8	-67.6	-53.9	-19.0	1.2	-11.9	-76.6	-67.4	-53.8

Table 3.8 continued

-17.7	2.3	-10.8	-76.7	-67.4	-53.8	-18.8	1.2	-12.0	-76.6	-67.3	-53.7
-17.6	2.3	-10.9	-76.7	-67.3	-53.7	-18.7	1.2	-12.0	-76.5	-67.1	-53.6
-17.6	2.3	-11.0	-76.7	-67.1	-53.6	-18.7	1.2	-12.1	-76.5	-67.0	-53.5
-17.5	2.3	-11.1	-76.6	-67.0	-53.5	-18.6	1.3	-12.2	-76.4	-66.9	-53.4
-17.6	2.3	-11.3	-76.5	-66.8	-53.4	-18.5	1.4	-12.3	-76.4	-66.7	-53.2
-17.4	2.4	-11.3	-76.5	-66.7	-53.3	-18.4	1.3	-12.3	-76.3	-66.6	-53.2
-17.2	2.5	-11.3	-76.5	-66.6	-53.2	-18.3	1.4	-12.4	-76.3	-66.5	-53.1
-17.1	2.5	-11.4	-76.4	-66.4	-53.1	-18.2	1.4	-12.5	-76.3	-66.3	-53.0
-17.0	2.6	-11.4	-76.4	-66.3	-53.1	-18.1	1.4	-12.5	-76.2	-66.1	-52.9
-16.9	2.6	-11.5	-76.4	-66.2	-53.0	-18.1	1.5	-12.6	-76.2	-66.0	-52.8
-16.8	2.6	-11.5	-76.3	-66.0	-52.8	-18.0	1.5	-12.7	-76.2	-65.8	-52.7
-16.7	2.8	-11.6	-76.3	-65.7	-52.7	-17.9	1.6	-12.8	-76.1	-65.5	-52.5
-16.6	2.8	-11.7	-76.2	-65.6	-52.5	-17.8	1.6	-12.9	-76.0	-65.4	-52.4
-16.4	2.8	-11.8	-76.1	-65.3	-52.4	-17.6	1.6	-13.0	-75.9	-65.1	-52.3
-16.3	3.0	-12.0	-76.0	-65.0	-52.2	-17.5	1.8	-13.2	-75.9	-64.9	-52.1
-16.1	3.0	-12.0	-76.0	-64.8	-52.1	-17.3	1.7	-13.3	-75.8	-64.7	-51.9
-15.9	3.0	-12.2	-75.9	-64.6	-52.0	-17.1	1.8	-13.4	-75.7	-64.5	-51.8
-15.9	3.0	-12.4	-75.9	-64.4	-51.9	-17.0	1.8	-13.5	-75.7	-64.2	-51.7

The MSE of the measured points to the fitted surface was computed for each specimen for both the Reuleaux and articular surface fitting methods. The surface fit method (Table 3.10) performed better overall than the Reuleaux method (Table 3.9) with lower MSEs in all cases. Since the articular surface was touted to be more robust against low-convexity surfaces, this outcome was expected. Both methods showed large MSEs at the wrist, particularly at the axis for radio-ulnar deviation (Wrist 2). This is due to the fact that that joint has a small range of motion that make fits difficult, particularly with the Reuleaux method [121].

Table 3.9: Reuleaux Method performance. Mean squared error on the algorithm on data sets.

	Shoulder (mm^2)	Elbow (mm^2)	Radio-ulnar (mm^2)	Wrist 1 (mm^2)	Wrist 2 (mm^2)
Cat 3	2.24	162	279	2248	342200
Cat 5	0.027	35.4	2.06	33.8	8217
Cat 6	0.52	230	248	263070	800330
Cat 7	11.0	33.2	13.5	44.7	95.9

Table 3.10: Surface Fitting performance. Mean squared error on the algorithm on data sets.

	Shoulder (mm^2)	Elbow (mm^2)	Radio-ulnar (mm^2)	Wrist 1 (mm^2)	Wrist 2 (mm^2)
Cat 3	0.13	0.75	0.045	3.66	6361
Cat 5	0.022	2.60	0.0014	12.77	668
Cat 6	0.27	19.38	3.75	15.43	80564
Cat 7	0.26	0.33	0.044	0.49	513

Employing the better performance of the surface fit method, the kinematics and anatomical data of all the cats were transformed, into a prototypical 'average' cat. Table 3.11 shows the locations of all the points, including markers and bony landmarks. It is noted that while the variability is on the order of millimeters for many of the points in the x- and y-axes, they show a high variability (up to 6.7cm) in the z-axis. Particularly larger variability is also observed in muscles with large attachments (e.g. Teres major origin (tjo) or subscapularis origin (ssco)) than muscle with discrete attachment (e.g. extensor carpi radialis insertion (ecri)). Variability is also considerably small in the sagittal (x-y) plane of the cat.

Table 3.11: Point Locations (±S.D.) for 'Average' Cat

Point Name		mean position (cm)	
	X	Y	Z
usp	0.82±0.34	-0.04±0.18	6.42±2.45
uop	-0.29±0.16	4.41±1.72	-3.51±1.35
tno	0.15±0.13	-0.96±0.55	-10.43±3.98
tni	1.16±0.45	-2.97±1.13	-8.01±3.03
tmedo	0.2±0.39	-2.12±0.9	-7.12±2.78
tmedi	-0.73±0.41	3.94±1.94	-3.31±1.63
tlongo	-0.01±0.2	-2.08±0.86	-9.29±3.53
tlongi	-0.11±0.14	4.54±1.73	-3.59±1.37
tlato	0.73±0.3	-2.5±0.98	-7.9±2.99
tlati	0.45±0.21	4.11±1.56	-2.84±1.13
tjo	-0.74±0.38	1.97±0.92	-12.7±4.82
tji	0.12±0.18	-2.45±0.94	-6.52±2.48
svs	-0.25±0.25	-1.32±1.05	-14.97±5.67
spso	0.07±0.17	-1.74±0.76	-14.91±5.64
spsi	0.78±0.39	-4.41±1.68	-7.66±2.92
ssco	-0.55±0.28	-0.13±0.42	-14.3±5.43
ssci	-0.71±0.28	-3.36±1.29	-8.09±3.06
supo	0.88±0.37	2.55±1.17	-1.51±1.26
supi	0.74±0.58	1.49±1.09	0.23±1.04
sdo	1.04±0.48	-1±0.46	-12.18±4.68
sdi	1.08±0.42	-1.9±0.8	-6.86±2.63
sca	-0.8±0.35	2.27±0.9	-13.03±4.93
sa	1.4±0.56	-2.29±1.1	-9.26±3.51
rus	0.95±0.38	-0.79±0.41	5.62±2.16
rsp	0.01±0.33	-1.57±0.63	5.54±2.12
rh	0.96±0.45	3.08±1.29	-2.14±0.85
pto	-1.08±0.41	2.95±1.12	-2.66±1.02
pti	0.27±0.21	1.11±0.61	0.93±0.7
plo	-1.02±0.4	3.52±1.36	-2.6±1.02
plr	-0.18±0.17	-0.25±0.22	6.18±2.34
pli1	-0.9±0.37	-0.63±0.29	7.88±3.04
pli2	-1±0.4	-0.76±0.3	9.65±3.65
pli3	-0.55±0.25	-0.48±0.2	10.05±3.83
pli4	-0.2±0.18	-0.08±0.09	10.04±3.82
pli5	0.08±0.17	0.4±0.22	9.62±3.64
ifo	-0.19±0.15	1.17±0.52	-14.28±5.4

Table 3.11 continued

ifi	1.24±0.52	-3.48±1.33	-8.28±3.13
hme	-1.2±0.47	3.08±1.19	-2.47±0.96
hle	0.91±0.37	3.45±1.35	-2.79±1.07
hgt	0.84±0.39	-4.12±1.57	-7.84±3.04
ftb	-0.42±0.21	-1.22±0.62	6.53±2.55
fmmcp	-0.83±0.35	-1.76±0.7	9.25±3.56
flmcp	0.67±0.31	-0.15±0.36	9.29±3.57
fdso	-0.35±0.2	0.42±0.37	5.07±2
fdsi2	-1±0.38	-0.72±0.3	9.59±3.63
fdsi3	-0.57±0.24	-0.45±0.2	10±3.81
fdsi4	-0.24±0.12	-0.02±0.09	9.98±3.8
fdsi5	0.06±0.13	0.43±0.22	9.63±3.65
fdpo	-0.69±0.29	3.51±1.35	-2.37±0.96
fdpr	-0.13±0.19	-0.25±0.18	6.02±2.29
fdpi1	-0.97±0.37	-0.67±0.27	7.82±3.02
fdpi2	-1.02±0.4	-0.74±0.31	9.54±3.61
fdpi3	-0.58±0.24	-0.51±0.22	9.95±3.79
fdpi4	-0.22±0.14	-0.12±0.09	9.95±3.78
fdpi5	0.06±0.12	0.33±0.19	9.52±3.6
fcuo	-0.41±0.21	4.08±1.6	-2.79±1.08
fcur	0.23±0.17	0.45±0.24	6.15±2.34
fcui	0.56±0.31	0.38±0.19	6.78±2.58
fcro	-1.01±0.43	3.27±1.26	-2.31±0.88
fcrr	-0.25±0.14	-0.57±0.28	5.89±2.24
fcri	-0.29±0.21	-0.64±0.3	6.38±2.46
eplo	0.61±0.25	3.74±1.51	-1.39±0.93
eplr	0.88±0.36	-0.89±0.4	6.35±2.42
epli1	-0.29±0.53	-1.39±0.54	7.31±2.83
epli2	-0.52±0.29	-1.6±0.8	9.46±4.64
edlato	0.96±0.4	3.51±1.35	-2.89±1.15
edlatr	1.11±0.43	-0.64±0.27	6.43±2.46
edlati2	-0.32±0.19	-1.66±0.65	9.81±3.74
edlati3	0.22±0.14	-1.35±0.54	10.14±3.9
edlati4	0.68±0.27	-0.82±0.32	10.09±3.87
edlati5	0.92±0.36	-0.29±0.18	9.77±3.71
edco	0.78±0.31	3.15±1.21	-3.44±1.31
edcr	0.89±0.37	-1.29±0.54	5.99±2.27
edci2	-0.35±0.15	-1.66±0.64	9.83±3.73
edci3	0.19±0.12	-1.36±0.54	10.19±3.91
edci4	0.66±0.27	-0.83±0.33	10.13±3.87

Table 3.11 continued

edci5	0.9±0.36	-0.27±0.18	9.81±3.72
ecuo	0.86±0.36	3.61±1.37	-2.31±0.91
ecur	1.18±0.46	-0.08±0.11	6.53±2.48
ecui	1.2±0.48	-0.19±0.21	7.24±2.78
ecro	0.49±0.23	2.44±1.01	-3.99±1.56
ecri	0.42±0.08	-1.9±0.17	6.23±0.34
epto	-0.72±0.51	-0.68±0.43	-8.35±4.48
epti	-0.59±0.43	3.99±1.98	-2.24±1.35
cbo	-0.31±0.17	-3.91±1.91	-8.58±4.2
cbi	0.05±0.16	-2.12±1.43	-6.52±3.23
bro	1.03±0.41	-2.12±0.86	-6.94±2.65
bri	-0.09±0.22	2.73±1.08	-1.92±0.76
bcdo	0.46±0.3	-0.4±0.36	-5.92±2.25
bcdi	0.29±0.33	-1.45±0.58	5.26±2.02
bbo	0.14±0.14	-3.95±1.5	-8.38±3.17
bbi	0.11±0.28	2.96±1.46	-1.59±0.92
aplo	0.72±0.36	2.46±1.17	0±1.55
aplr	-0.15±0.19	-1.46±0.57	5.57±2.11
apli	-0.49±0.21	-1.19±0.52	6.51±2.5
anco	0.33±0.22	1.24±0.99	-4.97±2.47
anci	0.58±0.31	3.83±1.87	-2.59±1.27
ado	1.51±0.59	-3.09±1.18	-8.81±3.34
adi	0.88±0.4	-1.32±0.92	-5.93±2.55
marker_paw3	2.14±1.97	0.69±2.73	9.44±5.07
marker_paw2	1.77±1.85	-0.08±1.56	8.54±4.78
marker_paw1	0.31±2.28	0.67±2.4	9.72±5.28
marker_radius3	-1.69±3.48	-1.1±1.8	3.65±2.61
marker_radius2	-1.04±2.34	-1.11±1.04	2.81±1.68
marker_radius1	-1.62±2.66	-1.26±0.95	4±2.27
marker_ulna3	4.13±4.08	1.87±1.56	-1.93±1.55
marker_ulna2	1.92±2.16	1.19±1.39	-1.92±1.44
marker_ulna1	1.2±3.15	2.22±2.23	-1.28±0.96
marker_humerus3	4.16±4.11	-0.48±0.55	-6.68±3.82
marker_humerus2	2.28±2.53	-2.16±1.49	-6.63±3.9
marker_humerus1	1.3±3.98	-1.65±1.47	-5.45±3.03
marker_scapula3	3.57±3.64	0.29±1.94	-12.07±6.55
marker_scapula2	2.47±2.79	-0.31±2.61	-12.48±6.7
marker_scapula1	0.86±3.67	-0.12±2.36	-12.15±6.54

Table 3.11 continued

locUlna	-0.71±2.54	2.86±1.54	-2.6±1.29
locRadius	0.98±0.52	3.3±1.7	-2.14±1.34
locPaw	-1.16±1.86	-1.56±1.14	5.17±2.65
ifr	1.23±0.6	-1.95±0.96	-9.03±4.41
locHumerus	0.05±0.14	-2.57±1.26	-8.27±4.04
ecrr	0.25±0.13	-1.7±0.83	5.7±2.78
ecrli	0.09±0.04	-1.57±0.77	7.76±3.79
ecrlr	0.23±0.13	-1.68±0.82	5.67±2.77
ecrlo	0.47±0.23	2.02±1	-4.29±2.1
fdsr	0.15±0.07	-0.42±0.21	6.67±3.26
tmedsi	-0.71±0.36	4.43±2.17	-3.3±1.61
tmedso	-1.08±0.53	3.12±1.54	-2.84±1.39

The recorded moment arms are again presented here for reference (Figure 3.10). The solid lines are the mean values and the correspondingly colored dashed lines represent the standard deviations. The range of elbow moment arm goes from 0 to 140° and those of the wrist from 0 to 75°.

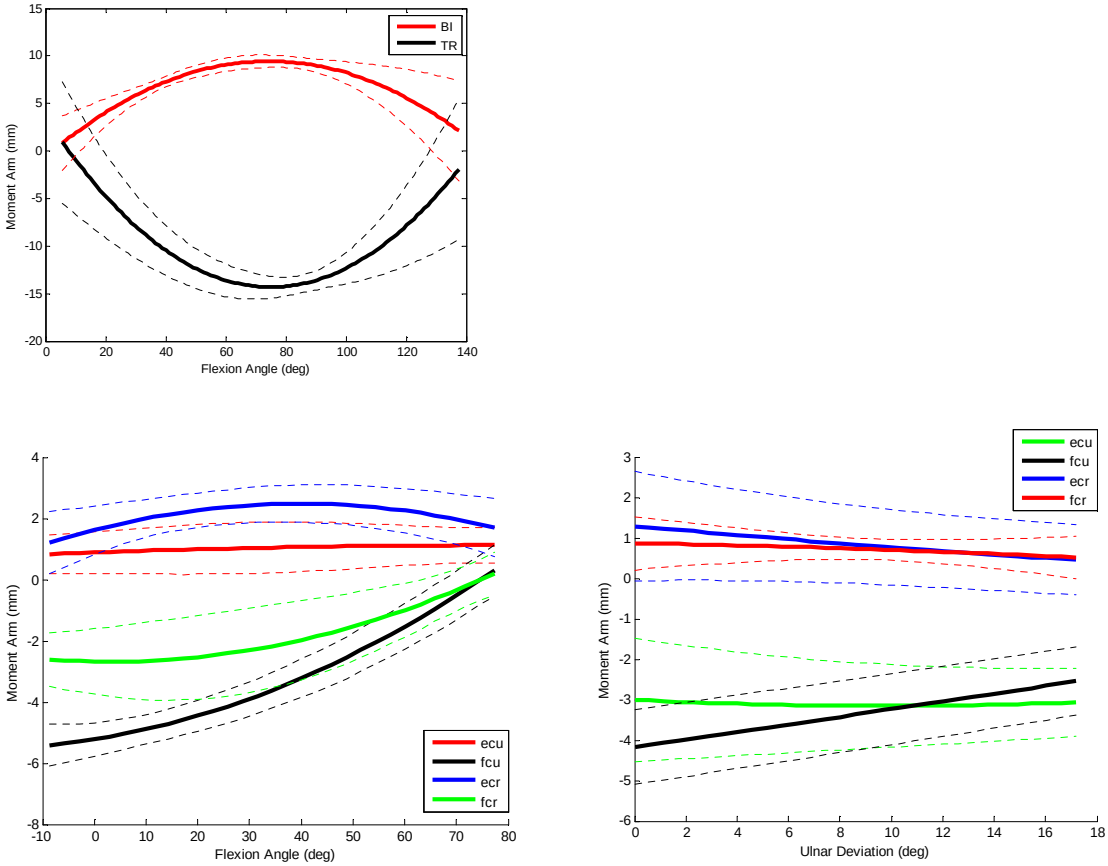

Figure 3.10. Average moment arm (±SD) of elbow and wrist flexion-extension motions and wrist ulnar deviation. The bands represent the mean moment arms with corresponding standard deviations across all 8 specimens.

The optimized limb (Table 3.12) produced axis fits that were qualitatively consistent with the locations of the muscles and joints (Figures 3.11-3.14). These were quantitatively optimized using the measured moment arms (Figure 3.10). The location of the joint centers and a bony landmark, within global coordinates, are also presented (Table 3.13). It could be determined from these that the lengths, at least based on joint centers, are 68.4mm for the scapula, 82.4mm for the humerus, 97.7mm for the ulna, 90.7mm for the

radius, and 36.5mm for the paw. These are all in good agreement with the measured segment lengths (Table 3.2).

Table 3.12: Optimized Joint Axes

	Location			Orientation		
Axis	**X(cm)**	**Y(cm)**	**Z(cm)**	**X(°)**	**Y(°)**	**Z(°)**
Scapula reference frame						
Flexion-Extension	0.05	-2.57	-8.27	-56.99	-3.81	-4.53
Internal-External Rotation	0.05	-2.57	-8.27	0.64	39.68	-41.33
Abduction-Adduction	0.05	-2.57	-8.27	-5.89	41.15	39.43
Humerus reference frame						
Elbow flexion-extension	-0.85	5.92	5.67	54.68	14.61	8.94
Ulna reference frame						
Forearm pronation-supination	1.78	-0.05	0.46	2.83	20.30	-53.51
Radius reference frame						
Paw flexion-extension	-0.57	-3.98	8.13	36.09	34.26	28.39

Table 3.13: Optimized Joint Axis Locations in Global Coordinates

Segment	X(cm)	Y(cm)	Z(cm)
caudal angle	0.44	13.15	-1.56
humerus	4.23	7.53	-0.66
ulna	-2.78	3.2	-0.79
radius	-2.71	2.84	1.01
paw	-0.94	-6.02	0.25
fmmcp	-0.57	-9.62	-0.26

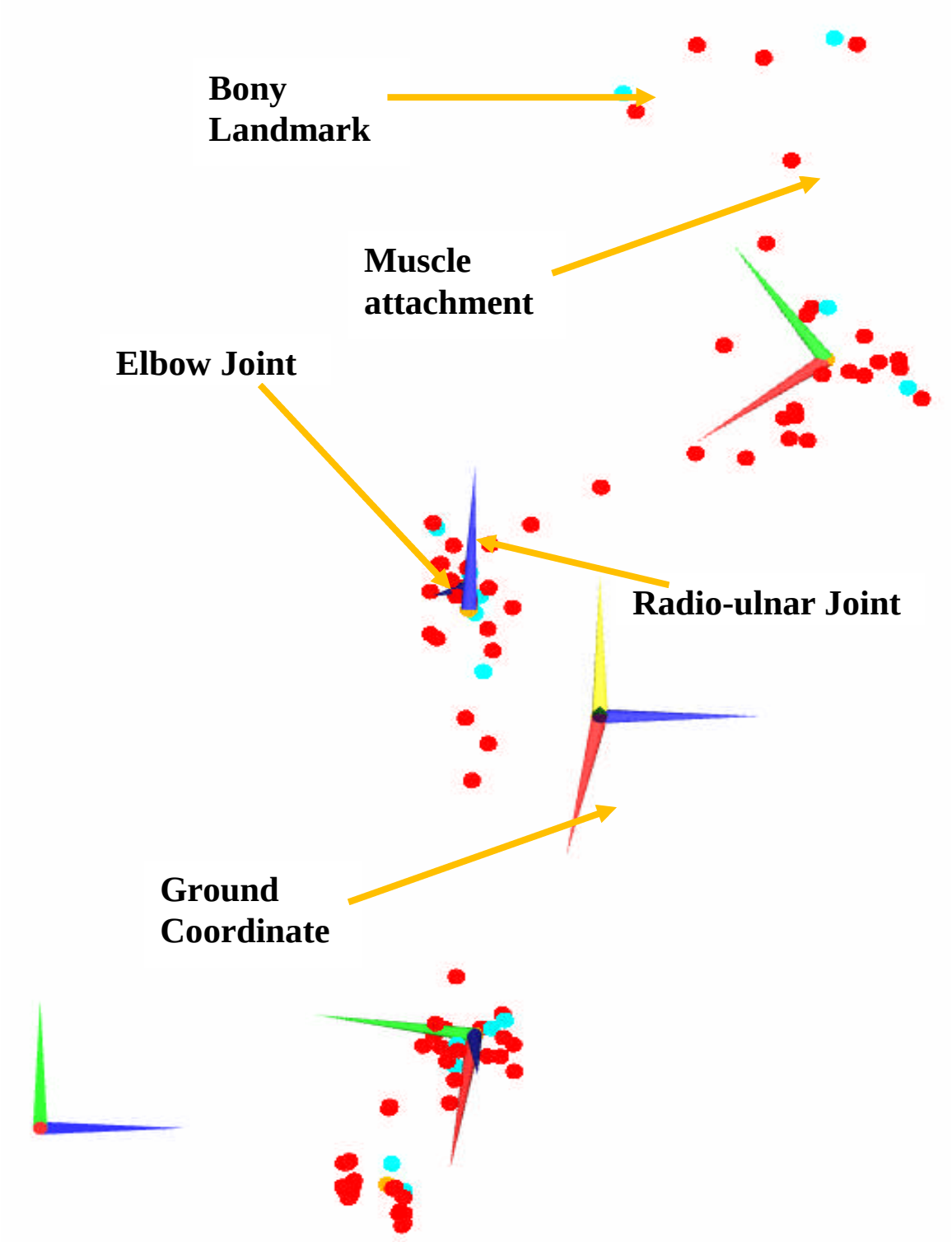

Figure 3.11: Attachment Points and Joint Centers in XY frame. The cloud of attachment points and bony landmarks, along with the moment arm-optimized joint locations.

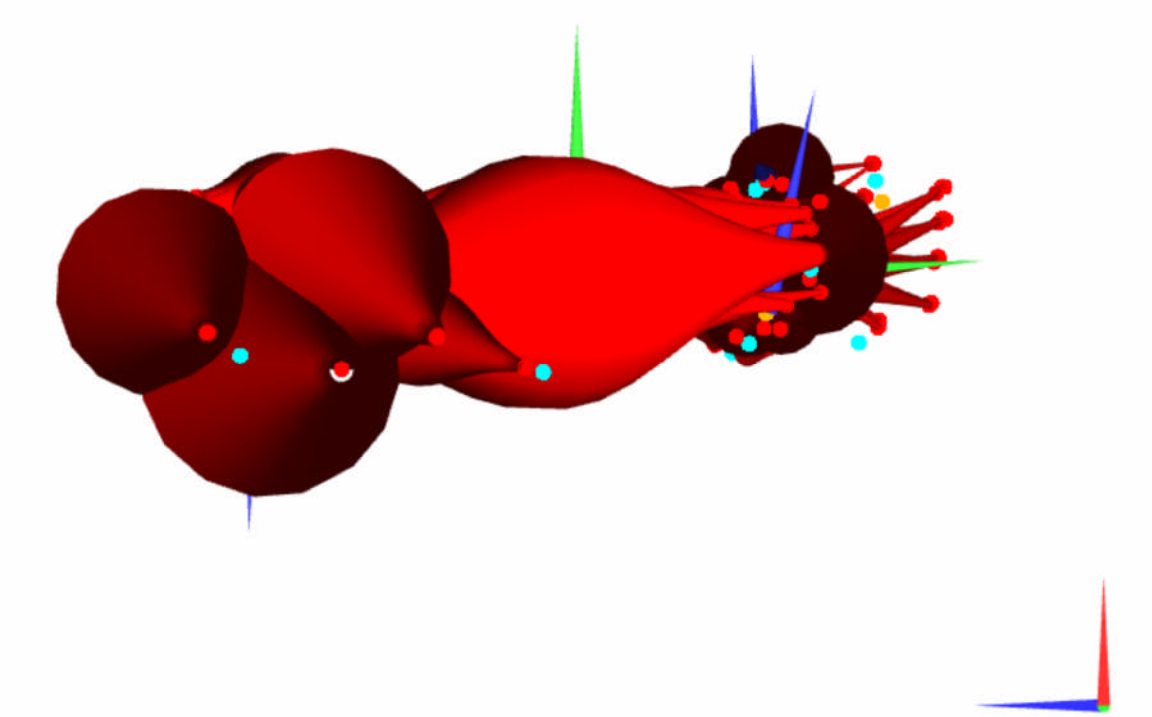

Figure 3.12: Attachment Points and Joint Centers in XZ frame (View from Top). Muscle attachment points and bony landmarks, along with the moment arm-optimized joint locations.

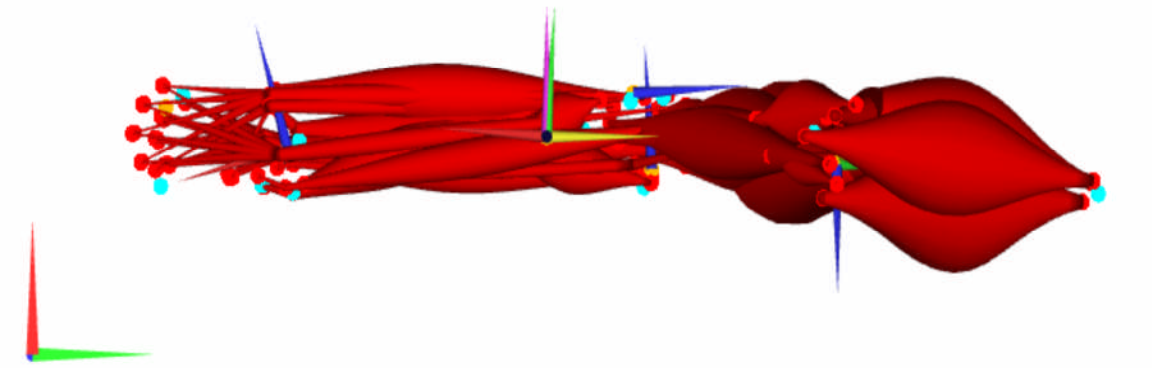

Figure 3.13: Attachment Points and Joint Centers in YZ frame. Muscle attachment points and bony landmarks, along with the moment arm-optimized joint locations.

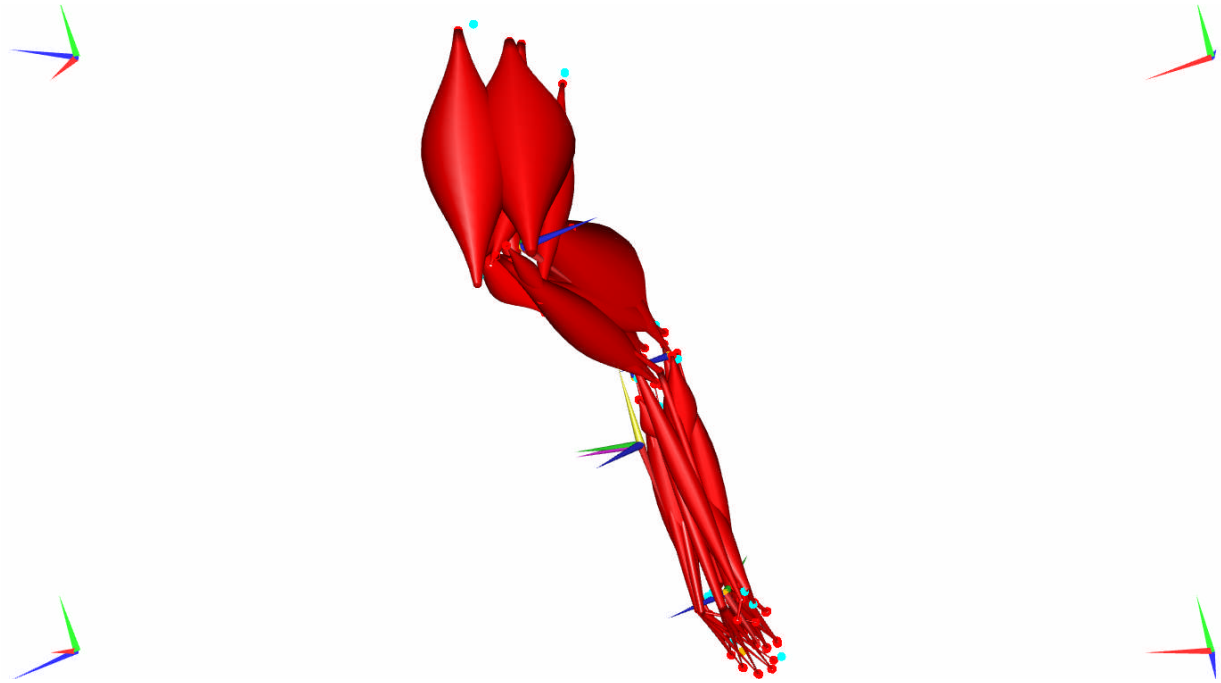

Figure 3.14: Attachment Points and Joint Centers in XYZ frame. Muscle attachment points and bony landmarks, along with the moment arm-optimized joint locations.

The moment arm fits at the elbow were shifted to the left (TBG) and to the right (BBI) of the data by approximately 25° (Figure 3.15a). At the wrist, the moment arm at ECU fell within the range of data while the arm at FCU was in agreement in an extended posture and grew smaller at a faster rate than the data as flexion angle increased (Figure 3.15b). The FCR moment arm was approximately twice as large as that of the data while the ECR was in the range at extension but quickly grew to 2-3 times the data moment arm (Figure 3.15c).

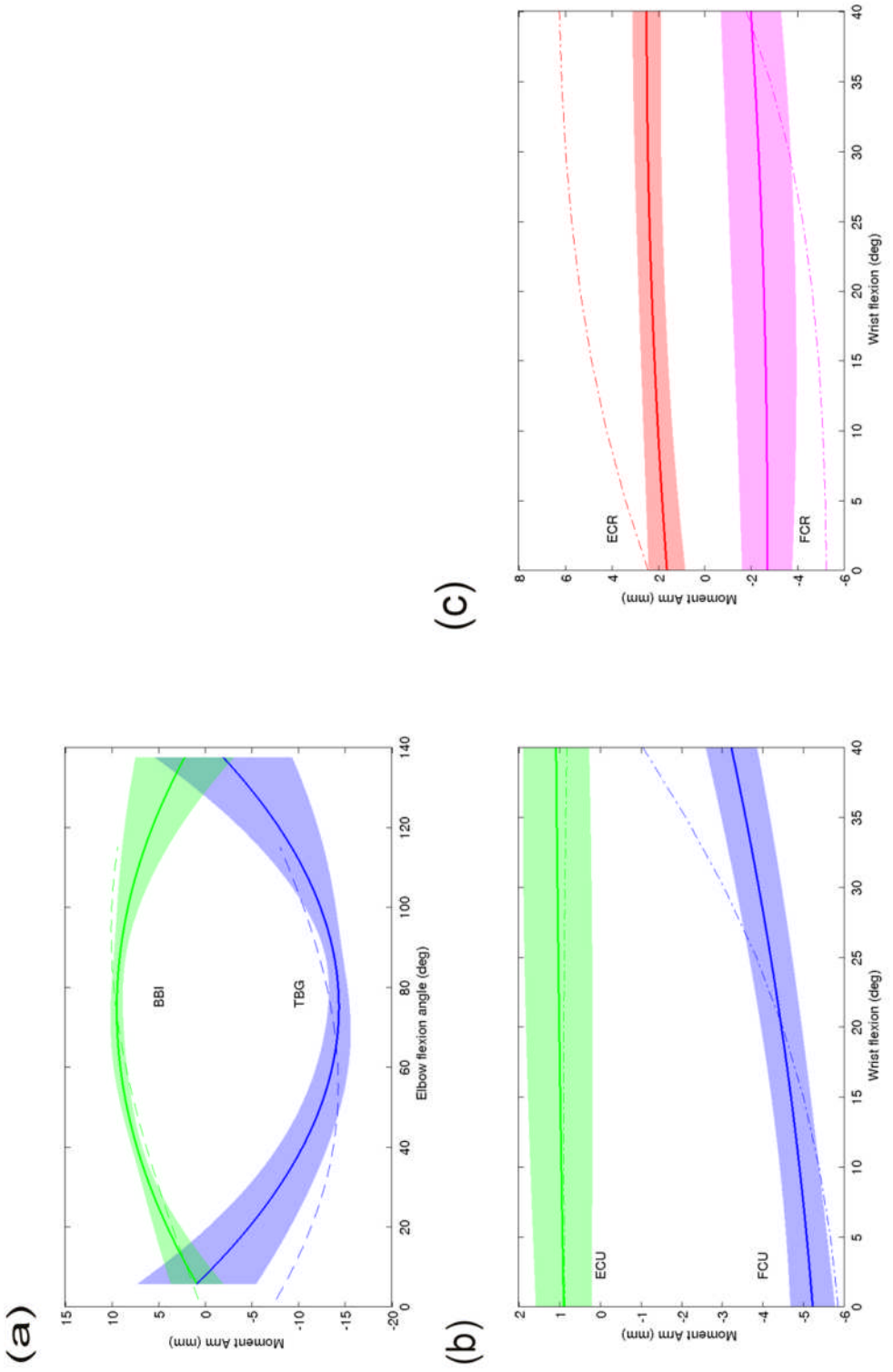

Figure 3.15: Optimized Moment Arm Fits. The solid lines, and shading, are the measured moment arm with standard deviations. The correspondingly colored dashed lines are the model fit.

During construction, the limb was made to mimic various postures recorded during locomotion [151]. The sequence of motions through these four postures, from touchdown (P1) to toe-off (P4), are qualitatively quite realistic (Figure 3.16). The sequence moves from right to left.

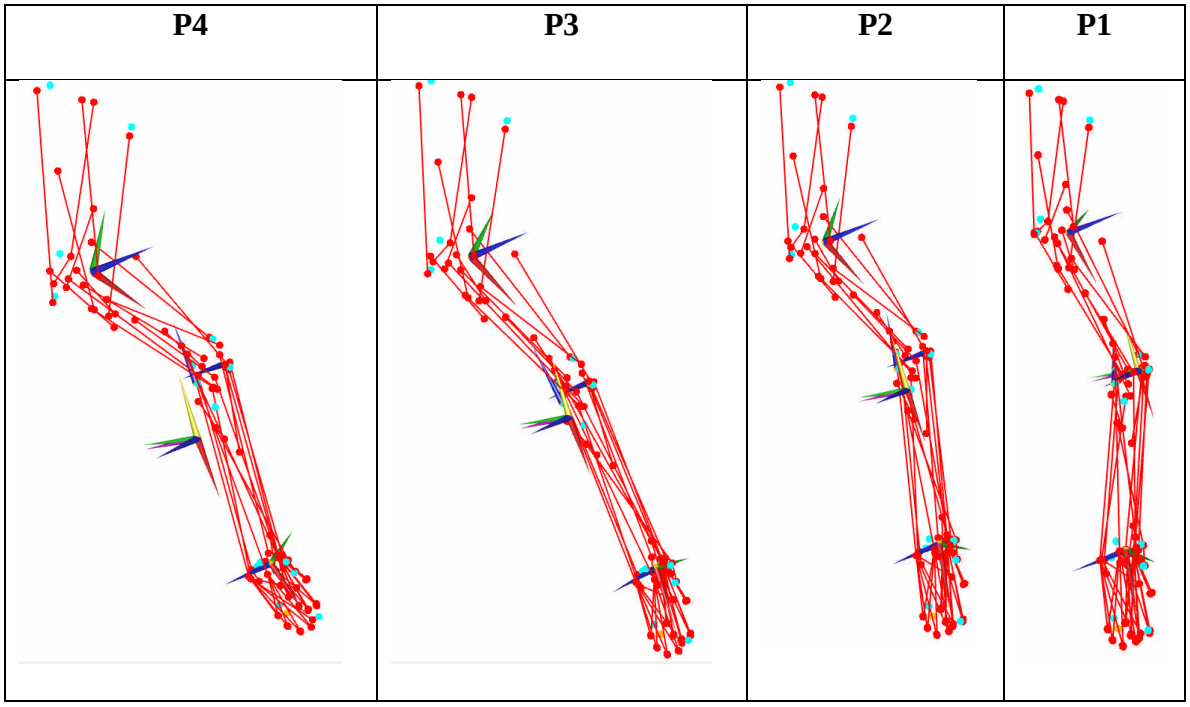

Figure 3.16: Sequence of locomoting postures. Joint angle data obtained from recordings of a cat during locomotion was used to recreate the sequence of postures.

3.5 Discussion

3.5.1 Limitations

In constructing this model, assumptions were made which may have affected the accuracy of the model. The shoulder of the cat is anatomically classified as a ball-and-socket (spheroidal) joint and the elbow as a hinge (revolute) joint [103]. The wrist is capable of 2 degree-of freedom movement: flexion-extension and radial-ulnar deviation (adduction-adduction) [154]. Therefore, engineering models of these joints were used. While the joints are described as such, the actual articular surfaces are not perfect spheres or hinges, and so do not produce the exact motions that would be expected. For this reason, experiments measuring moment arms were performed. These measurements, taken across the functional range of motion of the joints, allowed us to both validate and calibrate the model. In summary, the use of moment arm provided a way to mitigate the errors in the range of motion of the limbs brought about by using the perfect engineering joints. However, the wrist proved to be more complicated, owing to its articulation at both the radius and ulnar that substantially restricted the range of motion in the plane of radio-ulnar deviation. The optimizations were unable to produce moment arms that were within an acceptable range, sometimes giving values up to an order of magnitude larger. Physiologically, the ulnar and radial muscles approximately 10-12mm apart but the radio-ulnar moment arms are much smaller. The engineering joints used were unable to reproduce these moment arms and it was decided, owing to this issue and the small amount of ulnar deviation minimizing its biomechanical influence, that this degree of freedom would be excluded.

We chose to use motion data from reflective markers to determine the limb kinematics. However, an axis finder [155] could have been used as was done in a previous study to determine the joint axes of the hindlimb [26]. This mechanical device allows one to find the joint axes as a combination of revolute joints based upon their morphology. The system requires substantial trial and error, however. Furthermore, since the moment arm, and thus the joint axis, varies throughout the range of motion, the single center of rotation that is found will be in error.

The surface fitting [122] and Reuleaux methods were meant to fit individual joints based on the assumed motions of their specific joints. The spherical joints would map out partial spherical surfaces and the hinge joints arcs. Mathematical algorithms were already developed in the literature [115, 117, 119, 120]. The statistical estimation [118] was a novel technique that potentially allowed for calculation of all joint centers at once, simply from the specification of tree. All algorithms, performed well during simplified test cases, but gave erroneous joint axis results suggesting moment arms that were not physiological. One issue could be that the noise in the system was simply too great to overcome. Another is that the surface fitting was very sensitive to the initial parameter, especially the vector that is orthogonal to the surface. The noise in the data may have been such that the initial value was poorly estimated, leading to sub-par performance. A third factor could have been that during transport and/or fixation between taking the motion data and registering the anatomical points, the triads may have shifted leading to an inability to accurately combine the two.

Errors present in our model may also have come from several experimental sources. Since harvesting and preparing the limb for kinematic recording took 1-2 hours,

the onset of rigor mortis, or the extra force introduced to overcome it, may have introduced some abnormal movement that affected the position measurements.

The triads of markers were mounted with bone pins instead of placed on the skin to avoid the large source of error owing to shifting of skin during movement [156, 157]. The Steinmann pins were inserted in places where that were (i) more accessible, that is with some exposed bone to minimize tissue damage, and (ii) thicker, for firmer hold of pin so as to minimize artifacts owing to pin movement. However, these criteria placed the pins, particularly in the ulna and radius close to the joint centers at the elbow and the wrist, which has been shown to magnify errors in transformation-type algorithms in particular [121]. Furthermore, the act of coordinate transformation itself introduces errors that may be present in the local coordinate system (such as noise in the position measurement) into the other coordinate frame [117].

Another source of error may have been introduced by the limb variability across specimen, particularly given that we were attempting to create a prototypical cat. Data on segment lengths (Table 3.2) indicate that the greatest variability occurs in the humerus (SD = 3.55 mm), which in the worst case is less than 4% of the length. While this may seem to be a small percentage with respect to the placement of muscle origins and insertions, the variability could affect the location of the joint axes, which may have a significant impact on the moment arms particularly at the wrist where they are generally small (Brand et al ’82). Indeed, the variability at the wrist (SD = 2.51mm) is very much on the order of the size of the errors found in the moment arms. Attempts to reduce the error on the ECR and FCR resulted in greater errors on the other muscles for a total overall increase in the error at the wrist. Data from other moment arms, such as extensor

EDL and EDC and flexors PAL and FDP, would be necessary to achieve more reliable fits. The greater moment arms in the model would enable larger joint torques and a greater force response in a situation where a translational perturbation is applied vertically upwards at the paw.

The implemented model reconstructs the details of structure and kinematics of the feline forelimb, including a sequence of limb positions made by an intact cat during locomotion, and the elbow and the ulnar moment arms were in fairly good agreement. There exists the temptation to relax the constraints on the optimization to obtain better fits for the radial muscles since the graph suggests that the joint location is itself offset from the actual. However, with only a few muscles, we run the risk of over-fitting the model.

During reaching tasks in cats, the elbow moves through a range from approximately 48 - 150 ° and the wrist from 10 - 65 [10]. The model is capable of attaining those angles and moment arms are available for the entire range in the wrist and 90% of the elbow.

The variability in estimate joint axes can depend on the method used. Imaging such as MRI can be used, with variability as small as 2mm [158]. Other techniques, based on bone geometry [159] have been employed to determine knee joint axes. These geometrical method, which given fixed axes, have produced errors as much as 21mm in position and 11° in orientation. Functional axis of rotation schemes like SARA [117] have produced errors of 13mm and 7°. In our study, a combination of surface fitting, constrained minimization and moment arm tuning was required. The full combination

may not have been required, however, if they markers are set so that there is no chance of movement during transport of fixation. The Todorov algorithm is made to handle different types of sensor modalities. It may be possible that may have performed better with position-and-orientation sensors.

The current model has joint location variability as large as 4.2cm, which may have come from combining specimens fixed in different postures. A cat hindlimb model produced with the use of the Hollister method [155] gave a maximum joint position error of 10.9cm at the ankle but has been used to produce experimental verifiable results [4, 76].

While neural [5], including EMG [2, 6, 80], as well as behavioral [7-10], and architectural [1, 3] studies have been done in the forelimb, this is the first time that moment arms have been recorded. Furthermore, the model provides an ideal test-bed for the interpretation of these data.

A physiologically based 3D computational model of a feline forelimb has been developed incorporating muscle architectural properties musculoskeletal kinematics. The kinematic reconstruction performed has allowed us to parameterize the mechanics of the limb by obtaining joint angles, limb lengths and the appropriate placement of muscles. The surface method generally performed better than the Reuleaux method but required further optimization. Passive properties of the limb, namely moment arms, were used to further optimize joint kinematics. This work demonstrates that axis finding methods can provide a first approximation for biological joints, which then require further refinement to capture the unique kinematics of these joints. This muscle model employed here does not explain the processes of muscle contraction dynamics involving cross-bridge

energetics, but may provide future insight at a system level incorporating whole muscle mechanics and neural behavior.

CHAPTER 4:

STIFFNESS OF THE CAT FORELIMB:

EXPERIMENTS AND MODEL VALIDATION

4.1 Introduction

Interaction with the environment often involves compensation of a limb for instabilities so as to maintain posture. The question of which hierarchical levels of the musculoskeletal system are involved and their specific contributions remains an unresolved issue. The continuous feedback of muscle proprioceptors (muscle spindles, Golgi tendon organs and cutaneous receptors) through spinal pathways has been thought to provide a mechanism of stiffness regulation [4, 51]. This stiffness regulation has been posited to contribute to the control of posture by the neuromusculoskeletal system [29, 52]. However, other researchers have claimed that postural responses are determined by proprioceptors projecting to supraspinal centers, rather than from spinal reflexes [35, 112].

Motor behavior may be based on a complex interaction of limb anatomy, visual, vestibular, and somatosensory systems [20]. Within the realm of postural studies, substantial research has been carried out to determine the influence of each of these systems. In a seminal experiment, intact cats were trained to stand quietly on a platform while the surface was shifted in multiple directions in the horizontal plane [8, 9]. The cats' corrective response, termed the Force Constraint Strategy, was such that each hindlimb produced a ground-reaction force, in one of two directions, with amplitude modulated to the direction of perturbation. Electromyographic recordings, which

represent muscle activation patterns, demonstrated that the postural response is tuned to the direction of the supporting surface perturbation. It has been observed in humans during both stance and volitional reaching tasks [160, 161]. Supporting evidence of cortical control comes from studies of human soleus muscle responses during support surface perturbations that indicated corticospinal involvement during the late phase of stance control [23]. However, more recent research has shown that, even when cortical input was removed, the force constraint behavior was still observed [4].

The aforementioned contradictory results demonstrate that more needs to be done to clarify the extent of involvement of each of the systems in a postural control, but also begs the question as to what is the lowest level capable of producing the appropriate postural response observed in intact subjects. One of our main objectives is to experimentally answer this question. In addition, as a complement to empirical data, we aim to apply musculoskeletal modeling and analysis techniques, which have gained in popularity [25-28, 75, 162] to elucidate the underlying mechanisms of postural control and locomotion. Computational models allow one to more closely examine the various relationships among, and actions of, the diverse systems in carrying out motor tasks by looking at the effect of the assumptions made as to the structure of the various systems, as well as the impact their inclusion or exclusion of the behavior. As the model becomes more complex (such as the addition of force feedback or combination with the hindlimb model), it could be used to predict outcomes of experiments that might be intractable. As such, a mathematical model serves as an important research tool. We proposed to perform our experiments both *in vivo* and computationally in the cat forelimb, which has

not received much attention but is essential to obtaining a complete and accurate understanding of neuromechanical control.

As previously mentioned, Macpherson [9, 112] proposed that supraspinal input was required to produce the force constraint strategy. However, the decerebrate cat was found to produce the tuned muscular responses of force constraint without visual and vestibular feedback [78]. Furthermore, muscle spindle responses in anaesthetized cats were also appropriately tuned [79]. Our objective was to revisit the question of whether neural input - specifically spinal reflexes - was required, or were architectural factors sufficient to produce the force constraint pattern. Modeling experiments using the same disturbances on the cat hindlimb [77] indicate that the observed behavior is the result of limb architecture. With this in mind, we examined the responses in both anaesthetized (passive) and unanaesthetized (active) states. The influences of visual and vestibular feedback on the limb response were mostly eliminated in our protocol by having the animal's head fixed in a stereotaxic frame. We hypothesize that the limb architecture will be sufficient to generate the force constraint behavior.

Much of the research examining postural strategy in cats has focused on the horizontal plane, wherein the forelimb does not display a strong force constraint strategy [9]. However, a large proportion of the cat's response occurs in the vertical plane. Therefore, our objective was to extend the research on postural strategy to the sagittal plane. We hypothesized that the animal would display a stronger force constraint behavior in the sagittal axis than it does in the horizontal axis.

In experiments investigating arm posture in humans [30, 163, 164], it was demonstrated that the major axis of stiffness was along the line from the endpoint, or

hand, to the base pivot point, or shoulder, and re-directed itself based on posture. To verify this behavior, we examined the stiffness response for the limb in two different positions: one that represented the cat in an extended standing posture and another in a crouched posture.

Perturbation studies [30] have suggested that the postural response may be modeled by springs and may be represented by an ellipse. Based on this assumption, a non-spring-like response, indicated by a non-zero curl, could only be as a result of asymmetric neural feedback gain between muscles [29]. However, perturbation simulations on a three-dimensional cat hindlimb computational model [77] found that the force directions were spring-like but that the forces were asymmetric. We hypothesized that the forelimb will also be directionally spring-like, and that the magnitude of the force response would be asymmetric.

4.2 Methods

Experiments were performed on 5 female cats (8 forelimbs, 2 hindlimbs) ranging in mass from 3.0kg to 4.7kg. Animal care and the experimental protocol was approved by and carried out according to the standard of the Georgia Institute of Technology Institutional Animal Care and Use Committee and the Guide for the Care and Use of Laboratory Animals. Animals were first anaesthetized with isoflurane in an induction chamber, and then a tracheotomy performed to continuously provide and monitor anesthesia levels. The external jugular vein was cannulated to allow for fluid delivery to maintain blood pressure at acceptable levels. Each animal was placed in an upright position such that the head was mounted in a stereotaxic frame and the trunk was

supported in a hammock. The base of the tail was also clamped to support the hindlimbs. For the forelimb experiments each scapula was immobilized with a clamp on the scapular spine. For hindlimb experiments, the pelvis was clamped to prevent upward or side motion. The paws of the limbs to be manipulated were secured onto two 6-axis robotic actuators (TX60, Stäubli Robotics, CA) mounted with force sensors (ATI Industrial Automation, NC). In both forelimb and hindlimb experiments, the non-manipulated limbs rested on a stable surface. An intercollicular decerebration operation was then completed. In this procedure, the head was shaved, and an incision made rostro-caudally to expose the cranium. The cranium above the neocortex was carefully removed with a pair of rongeurs. Sections of cortex surrounding the brainstem were then aspirated to reveal the colliculi, and a vertical transection made through the superior colliculus and all brain matter rostral to the transection was removed from the cranium. This procedure results in the removal of the inhibition by the cortex of extensor motor neurons and produces muscle directional activation patterns that are similar to those in the intact cat (Honeycutt et al. 09).

The perturbation consisted of 1 cm displacements of the supporting surface in 16 directions in the sagittal plane. Natural (no electrical stimulation) spontaneous endpoint force responses of the limb were recorded while in isoflurane-anaesthetized (passive) and unanaesthetized (active) states. The perturbation profile was that of a ramp and hold, consisting of the 1cm movement (Figure 4.1). Background force data was recorded for the 100ms preceding each perturbation and the mean subtracted from its corresponding disturbance response, which was calculated as the mean from 0.2-0.3s. Two defined

positions of the limb were used, which were labeled as 'extended' and 'crouched' (5 cm above extended).

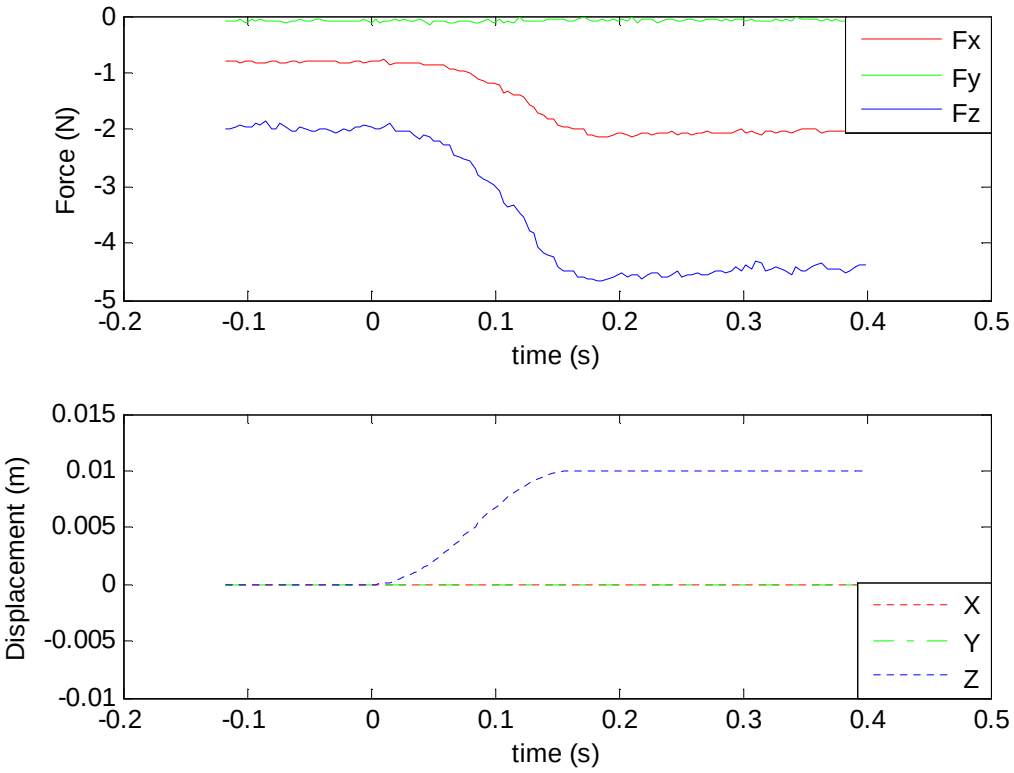

Figure 4.1: Ramp and hold force response.

4.2.1 Analysis

4.2.1.1 Stiffness Definition

The stiffness, which is a measure of the force experienced by an object in response to a displacement, is one component of the limb impedance, the other components being viscosity and inertia. The determination of stiffness was performed under the assumption that the neuromusculoskeletal system is mostly spring-like in nature (Mussa-Ivaldi et al., 1985). Thus, for perturbations in the sagittal plane about a

reference position, the force response is directly proportional but at varying angles of direction. The behavior is represented by the following equation:

$$\begin{bmatrix} F_x \\ F_z \end{bmatrix} = \begin{bmatrix} K_{xx} & K_{xz} \\ K_{zx} & K_{zz} \end{bmatrix} \begin{bmatrix} dx \\ dz \end{bmatrix} \quad or \;\; F = K\, dx\,,$$

where F_x and F_z are the horizontal and vertical components of the force response, dx and dz are the corresponding components of the given perturbation, and K_{xx}, K_{xz}, K_{zx}, and K_{zz} the elements of the stiffness tensor. The stiffness tensor can be divided into symmetric, K_S, and antisymmetric, K_A, components as follows:

$$K_S = \frac{K + K'}{2} \quad , \quad K_A = \frac{K - K'}{2},$$

where K' represents the transpose of K. In our analysis the stiffness tensor is calculated by a least-squares regression of the force and displacement.

The response is represented in the form of a stiffness ellipse, which is produced by multiplying the circular displacement vectors by the stiffness tensor. The long axis of each ellipse gives the direction of displacement for which the restoring forces are maximal while the short axis gives the direction of displacement for which the restoring forces are minimal. The maximum (K_{max}) and minimum (K_{min}) stiffness can be obtained by the eigenvalues of the stiffness tensor. The angle of the major axis with the x-axis (α), the stiffness orientation, was calculated from the eigenvectors. If the musculoskeletal system is spring-like, then the actual force responses will be represented by the stiffness ellipse.

4.2.1.2 Stiffness Ellipse Models

Previous research on a hindlimb model analyzed the response of the endpoint to perturbation against three idealized models, named uniform, ellipsoid and force constraint models [77]. Data from the current experiment with force field profiles fitting the ellipsoid and force constraint models (normalized to the same maximum force) are used as illustrations (Figure 4.2). The uniform model was generated from the identity matrix. Representations of the force field, force magnitude and force direction of each model are shown in rows a, b and c respectively. *Strictly speaking, these all represent ellipsoid models, but each is at a different region of the spectrum with respect to isotropy*.

Useful parameters for analysis of the magnitude and direction plots are shape and deviation. The shape index, the ratio of K_{max} to $K_{min,}$ represents the level of anisotropy of the stiffness ellipse. A higher shape index corresponds to greater anisotropy. The deviation is the angle between the horizontal axis and a best fit line through the direction plots.

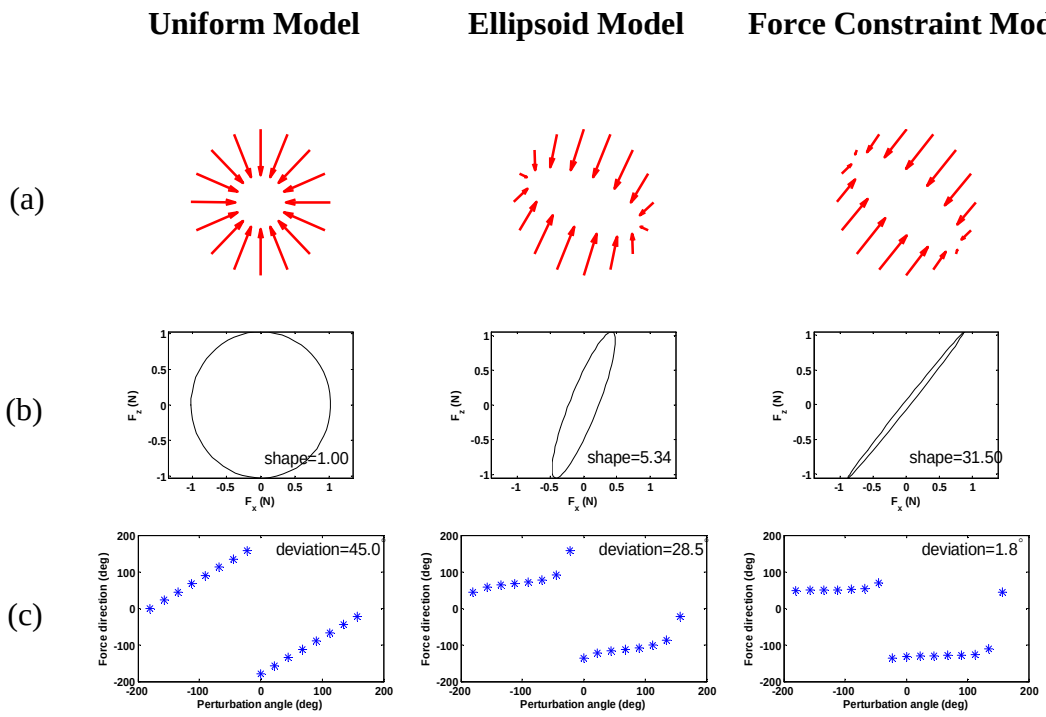

Figure 4.2. Idealized models of limb behavior. Plots of the (a) force field, (b) force magnitude and (c) force direction of Uniform, Ellipsoid and Force Constraint Models.

.

Of note in these models is that there are two points, found at opposite ends of the force field plots (a), where the force transitions from one direction the other, resulting in a discontinuity in the direction plots (c). During calculation of the deviation, these two points are excluded from the measurement of slope. The uniform model, at the lower end of the spectrum, treats the leg endpoint response as that of a linear spring, in which the force opposes the direction of the perturbation and has equal magnitude in all directions (Figure 4.2a). When separated into magnitude (b) and direction (c) responses, this model results in a circular (shape = 1) force magnitude and lines of constant high non-zero slope (approaching 45°). At the high extreme, the force constraint model, as the name suggests, restricts the force response to a particular direction independent of the

perturbation direction. The magnitude of the response is proportional to the projection of the perturbation direction onto the constrained force direction. Thus, the magnitude-only plot gives a highly (shape >> 1) eccentric ellipse (b) and the direction-only response is that of lines of low (approaching 0°) slope. The ellipsoid model falls in between the first two models. It treats the muscles as springs while simultaneously taking into account the kinematics of the limb that relate the endpoint displacement to the joint angle displacements. This latter constrains the range of possible limb orientations and hence the force response. The magnitude-only response is an ellipse that is less anisotropic than that of the force constraint model (1 < shape << 30) and the directional response shows curves of variable slope (> 10°). Thus, an inverse relationship is seen between the shape and deviation. It is to be noted that none of these models accounts for any asymmetry in force magnitude, that is, they assume the ellipses are centered about the zero perturbation position as would be the case for spring-like forces.

4.2.1.3 Curl and Z_{mean}

In a spring-like system the stiffness matrix is symmetric, that is $K_{xz} = K_{zx}$. However, if this is not the case, the level of non-spring-like behavior can be quantified via a term known as the curl, which is calculated as the difference between the off-diagonal terms of the stiffness tensor (i.e. $K_{zx} - K_{xz}$). The magnitude of the curl forces can then be compared to those of the symmetric component to evaluate the level of of non-spring-like behavior. The ratio of the curl to the smallest (K_{min}) and largest (K_{max}) eigenvalues gives the values Z_{max} and $Z_{min,}$ respectively. Non-spring-like behavior can also be measured by

a parameter referred to as Z_{mean}, a geometric mean of Z_{max} and Z_{min} [29]. Z_{mean} is calculated by the following equation:

$$Z_{mean} = \sqrt{\frac{|K_A|}{|K_S|}} \ ,$$

where | | represents the determinant.

4.3 Results

These experiments were performed in order to characterize the stiffness of the forelimb by measuring the postural response to perturbations in the sagittal plane. The experiments also permit a comparison of the postural strategy employed, be it uniform, ellipsoid or force constraint, between the forelimb and hindlimb.

The results for a representative forelimb are shown in Figure 4.3. The directions of the force fields are similar to that of the force constraint model but the ellipse fit equals or underestimates in one direction and overestimates in the other. The characteristics are more clearly revealed on separate examination of the force magnitude and force direction plots. The plots indicate response to perturbation, whereby a positive value for the force magnitude shows response to stretch (or pulling away from the trunk) and negative magnitude showing response to compression (or pushing toward the trunk). The force magnitude plots show that in the extended position, whether active (Figure 4.3a) or passive (Figure 4.3b), the ellipse fit underestimates the force magnitude in the positive direction, that is, when the limb is being stretched. Conversely, the ellipse fit overestimates the magnitude in the negative direction when the limb is being compressed. The magnitude of the force, plotted on the same scale, is much higher in the active state, as is the shape index (28.71 vs. 8.85). In the crouched posture, the response is inverted.

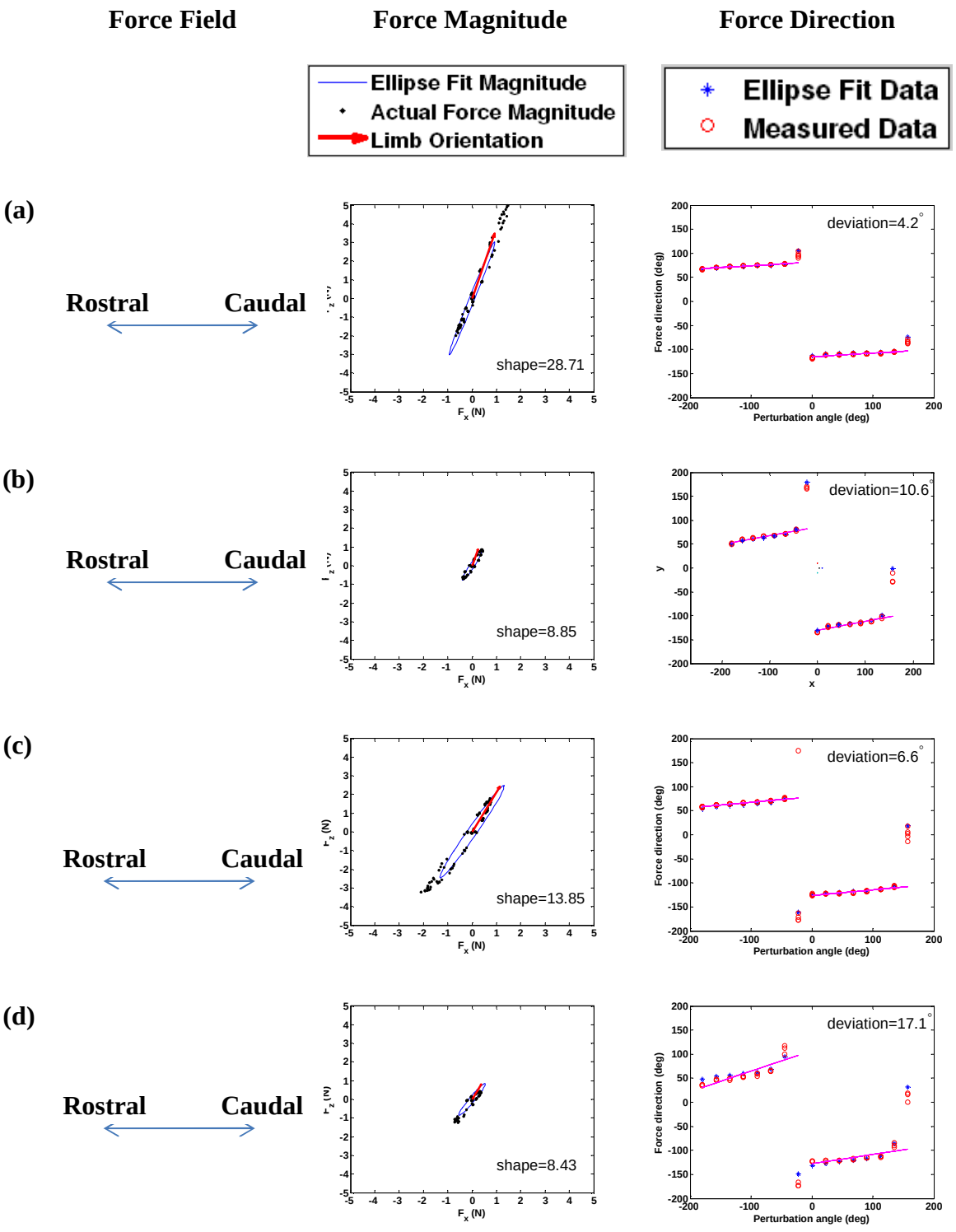

Figure 4.3. Forelimb Sagittal Plane Force Results (Representative Animal). Force field, and separate magnitude and direction responses of the forelimb of a representative cat. (a) Active extended; (b) Passive Extended; (c) Active crouched; (d) Passive crouched.

In both active (Figure 4.3c) and passive (Figure 4.3d) states, the ellipse fit overestimates the force magnitude in the positive direction, when the limb is being stretched, and underestimates the magnitude in the negative direction when the limb is being compressed. As in the extended position, the magnitude in the active state is larger than in the passive state, and the shape index in the former is 13.85, as opposed to 8.43 in the latter. The force direction plots in the active state indicate a force constraint strategy while the passive state response tends toward the ellipsoid model.

The results for a representative hindlimb are displayed, for comparison, in Figure 4.4. The directions of the force fields are more similar to that of the ellipsoid model in this case. The force magnitude plots show a similar behavior as those in the forelimb with respect to the position-dependent asymmetry and the state-dependent difference in magnitudes. Namely, while the limb is initially in the extended position (Figure 4.4a & b), the ellipse fit underestimates the force magnitude in the positive direction, when the limb is being stretched and over-estimates during compression. The opposite is seen while initially in the crouched position (Figure 4.4c & d). The magnitudes are also greater in the active (4.4a & c) than the passive (4.4b & d) state. However, the shape indices are all much smaller (at least by 50%) than the forelimb counterpart. Correspondingly the broader ellipse fit profile conforms to the ellipsoid model's. Finally, the force direction plots deviate from the flat profile of the force constraint strategy towards that of the ellipsoid model, further supporting the magnitude and field results.

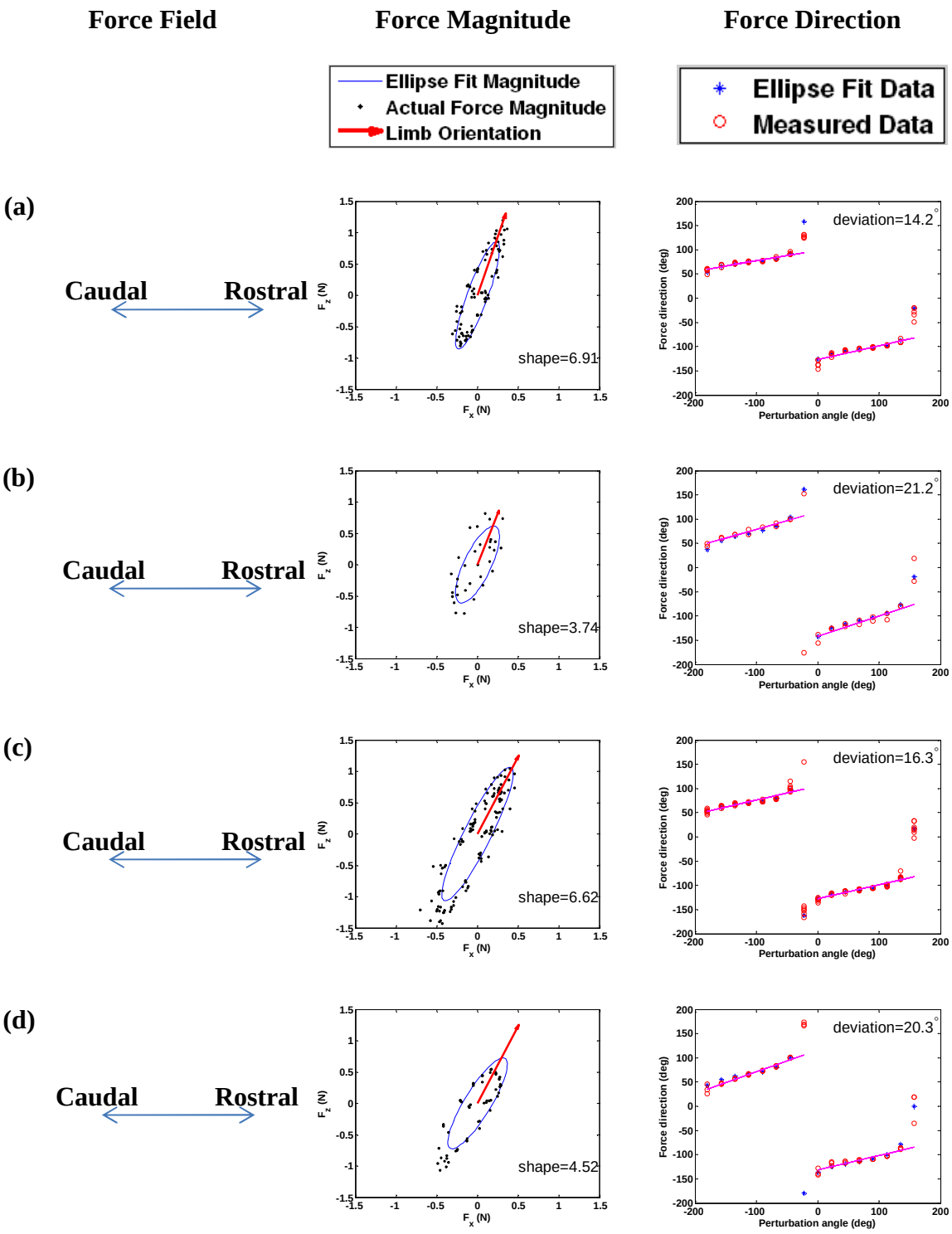

Figure 4.4. Hindlimb Sagittal Plane Force Results (Representative Animal). Force field, and separate magnitude and direction responses of the hindlimb of a representative cat. (a) Active extended; (b) Passive Extended; (c) Active crouched; (d) Passive crouched.

The responses of all forelimbs were combined, normalizing for limb orientation, and are shown in Figure 4.5. The results mirror those found in the representative limb (Figure 4.3). In the active extended paradigm (16a), the force magnitude is skewed in the positive direction, reaching values of 8N, and the force direction exhibits flat lines indicative of a force constraint strategy. During passive extended stance (16b) the force magnitude is still skewed in the positive direction but the strength is much lower with a maximum of approximately 1.3N. The force direction is still that of the force constraint strategy. In active crouch (16c), the response is skewed in the negative direction with maximum close to -4 N, compared to a -1.7 N in passive crouch (16d). While the former state still exhibits force directions suggestive of force constraint, the latter shows a directional deviation of 18.3°, which suggests an ellipsoid model response. Summary magnitude data is shown in Table 4.1. Only the active extended position is significantly greater than the corresponding hindlimb position and state (One-sample T-test, α=0.05), as well as the other positions and states (T-test, α=0.05).

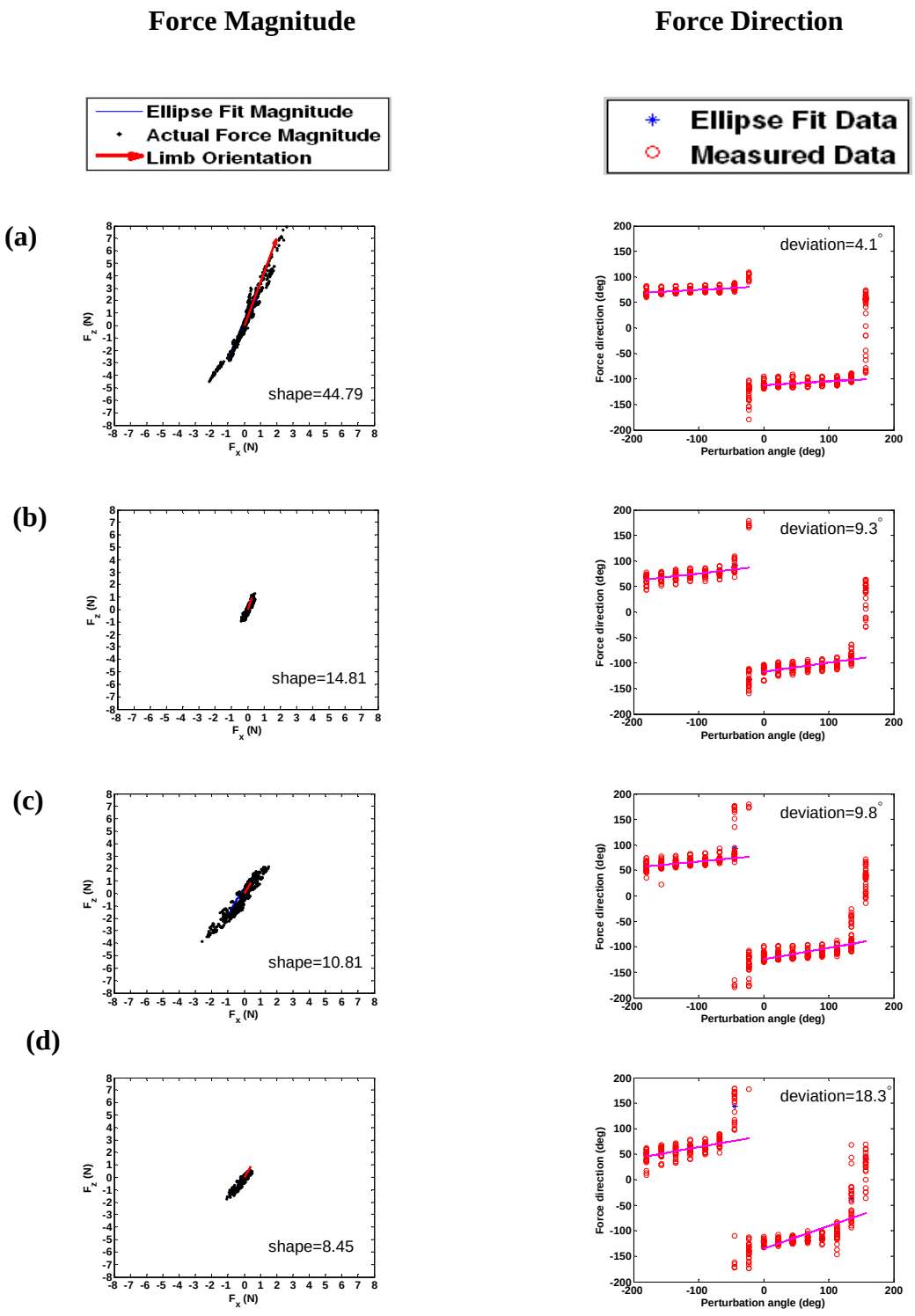

Figure 4.5: Forelimb Sagittal Plane Combined Force Responses. Force magnitude and force direction of all 8 forelimbs are shown. (a) Active extended; (b) Passive Extended; (c) Active crouched; (d) Passive crouched.

Table 4.1: Summary Shape Indices. * indicates statistical significance wrt other forelimb states. $^{+}$ indicates statistical significance wrt corresponding hindlimb state and position.

	Forelimb (Combined)	S.D.	Hindlimb (Representative)
Active Extended	44.79*$^{+}$	12.48	6.91
Passive Extended	14.81	7.13	3.74
Active Crouched	10.81	8.24	6.62
Passive Crouched	8.45	13.15	4.52

4.4 Discussion

Our first objective was to extend the research on postural strategy employed by the intercollicular decerebrate cat to the sagittal plane. Our second objective was to obtain active and passive responses to support perturbations in the sagittal plane of the forelimbs while in two different stance positions. With the leg initially in the extended position, a greater force response was produced for perturbations that further extended the leg than for those that compressed the leg. This was observed in both the active and passive states. When the leg was initially in the crouched position, the inverse response was observed in that a larger force was produced for disturbances that compressed the leg. Larger forces were produced in the active state than in the passive in both positions. The active forelimb possessed more constrained stiffness ellipses than the passive, with high shape indices and low deviation from horizontal. These data allow us to understand the roles of the nervous system and limb geometry in the postural response to perturbations of limb supporting surface and to evaluate the performance of our computational limb models.

4.4.1 Limitations/Technical Issues

Experiments may have benefitted from standardization of the limb posture in terms of the joint angles to more closely conform to those found in previous literature. We were forced to deviate from this procedure, however, due to spatial constraints. While in the stereotaxic frame, we needed to position the limbs being measured beyond the support surface of the non-experimental limbs to ensure that the robotic arm would not hit the rigid support surface apparatus during perturbations. To compare all the limbs, each was normalized, to a single limb orientation. This was considered valid since the scapula is fixed and the centroid is one of the points used for determining limb orientation. Thus, the effect is that of shifting the supporting surfaces of the different limbs to the same initial position.

Unlike the pelvic region in which the leg bony articulation to the trunk, the scapula is only connected via muscle. This allows the scapula to have a large range of movement capable of considerable damping of perturbations at the endpoint. The extra rigidity conferred to the limb by clamping the scapula would eliminate the damping owing to scapula movement and allow the limb to exert higher vertical forces than it otherwise would with the scapula free. Constraining the scapula may have increased the shape to the extent the forelimb was actually more force constrained than the hindlimb, in opposition to the results found by Macpherson et al (1988) for intact cats in the horizontal plane. However, that study did also note in passing that the vertical forces were an order of magnitude greater than the horizontal forces. Therefore, it may be the case that in the sagittal plane, the differences are more due to geometry than neural mechanisms.

It was observed that, in later experiments, the magnitude of the curl was much smaller than in the earlier experiments (Table 4.2), and that these later values were on the same order of magnitude as those found during arm posture experiments in humans [30]. The discrepancy in magnitude may have been due to signal processing modification in the hardware, after results on the first four limbs were collected, that led to a reduction in the noise level. The lower degree noise fluctuations may have resulted in better calculation of the average steady state response.

Alternatively, the placement of the paw may have been such that the limb was twisted from its usual position in the intact cat, leading to an inherent torque-production in the response. In our experiments the curl was statistically larger (T-test, $\alpha = 0.05$) in the active extended state than the passive extended state. There was no difference between the crouched states. However, when the relative magnitude of non-spring-like behavior with respect to spring-like stiffness, represented by Z_{mean}, was compared, no statistical difference was found between the active and passive states. Therefore, even though the curl was greater in the active extended case, this was probably due to greater force production overall.

Table 4.2. Average Curl and Z_{mean} for all forelimbs in all positions and states.

Active Extended		Passive Extended		Active Crouched		Passive Crouched	
Mean Curl	Z_{mean} (%)	Mean Curl	Z_{mean} (%)	Mean Curl	Z_{mean} (%)	Mean Curl	Z_{mean} (%)
25.4	36.5	15.0	43.9	26.3	50.8	12.1	65.6
32.5	63.2	16.9	67.5	11.2	19.9	13.3	75.0
43.1	381.8	14.4	71.0	18.3	46.4	8.4	35.9
45.6	37.5	8.6	35.9	7.2	8.3	14.0	39.8
4.8	9.9	1.6	4.5	5.4	6.2	2.5	3.4
12.9	10.6	1.5	2.6	5.1	3.4	7.5	11.0
12.8	8.7	5.3	8.1	9.4	4.4	5.3	5.7
14.8	16.3	13.0	33.2	2.4	1.6	17.9	32.6

The ellipse fit is able to capture the directional characteristics, but not the force magnitude, in both active and passive states. The force field and force direction (Figures 14, 15 and 16) data reveal excellent overlap between the ellipse fit and the measured results in terms of the restoring force direction. However, the observed force magnitude is skewed to one side or another so that the ellipse underestimates it in one direction and overestimates it in the other. Previous research in humans suggested that the stiffness ellipse amply represented the experimental data and there was no asymmetry [30, 163, 165]. The displacements imposed (5mm, 8mm and 10mm) were small enough relative to the length of the human arm that they produce movements that were maximally at 2% of the range of motion. This placed the fibers within the short-range stiffness regime [33] wherein the change in muscle length is < 1% [166] and the muscle behavior can be approximated to that of a spring. Using the musculoskeletal model, it was found that the 10mm displacement employed in our experiment results in a change in muscle length with mean 1.30±0.05 %. This means that the perturbations stretched the fibers beyond the region of short-range stiffness, whereby the non-linear viscous properties of muscle become more evident [167]. Given that the stiffness ellipse fails to capture the force magnitude properties, it may not be a suitable model and suggests that the limb may not be spring-like for movements outside the short-range regime.

There is greater anisotropy/eccentricity and the limb axis is more in-line with the data in the active limb than in the passive limb. Although there was a tendency for the shape indices to be greater in the active state than the passive state in both limbs and in both positions, statistical significance was only achieved in the extended forelimb case. In this scenario, the stiffness orthogonal to the limb axis increased by 207% over the

passive while the stiffness along the limb axis increased by 283% over the passive state. Thus, the greater anisotropy in the active limb would seem to be a direct result of a more substantial increase in force magnitude along the major axis of stiffness. This could be as a result of intrinsic activation of the extensor-flexor muscles. It may also be due to increased neural drive from spinal pathways functioning on top of, or subsuming, the already underlying behavior of the passive limb to further constrain it along the limb orientation axis. Since supraspinal input has been removed in the case of the passive limb, they cannot be a factor.

The forelimb force magnitude is more anisotropic and force direction more closely approximates the force constraint strategy than the hindlimb. Support surface perturbation experiments performed in intact cats [8, 9] show that the force response direction in the horizontal plane was constrained in all limbs, but that the forelimb response was less so than the hindlimb's. Our results indicated that the opposite was the case. The shape indices are consistently higher in the forelimb and the force direction plots exhibit the low slope lines consistent with the force constraint strategy. However, the force direction plots of the hindlimb conform to the ellipsoid model. These may not in fact be a contradiction of the previous results since those were performed in the horizontal plane. It may be the case that the forelimb is much more constrained in the sagittal than in the horizontal plane.

The limbs exhibit position-dependent, state-independent asymmetric gains, suggesting that the asymmetry is a geometric phenomenon. The results of the experiments indicate that both forelimb and hindlimb produce greater force when perturbations further extend the limb from an initially extended position or further

compress it from an initially crouched position. This behavior occurs regardless of whether the animal is in an active or anaesthetized state. The results show that the core behavior, that is the asymmetry in force response, cannot originate from the stretch reflex or from supraspinal sources since all neural input was silenced in the anaesthetized state. Thus, the action is geometrical in nature.

4.4.2 Further Findings

During the extended position, the limb was stiffer when being stretched than when compressed. During a crouched posture, the opposite behavior was exhibited. In one of our experiments we found that the cross-over point, that is the point wherein there was no asymmetry in force response, occurred within 5mm vertically above the extended position. These findings led us to the conclusion that the extended position was in fact an over-extension of the cat limb such that further attempt of extension brought the limb close to the edge of its working space, and hence, close to a singularity. This resulted in the limb behaving like a rigid rod that, with high stiffness, generated a force that was well beyond that generated for perturbations in the opposite direction where the limb is closer to its normal operating mode. Indeed, experiments involving cats in self-selected posture [10, 168] show internal joint angles of 170°-177° at the wrist, 135°-150° at the elbow and 58°-70° (w.r.t. horizontal axis) at the shoulder. The corresponding values in our experiments were 173°±4° at the wrist, 137°±5° at the elbow, and 80°±7° at the shoulder. While the first two are within normal ranges, the last is well outside. Changing the angle of the shoulder in the model to an acceptable range did change the direction of the ellipse, but did not change the behavior during extended or crouched positions. The extended

position of the shoulder was, as previously stated, a result of the necessity to maintain the limb away from the rigid support surface to prevent collision with the robotic arms. Therefore, it would seem that the normal stance position of the cat is such that it operates in a regime where it preferably resists compression, or collapse, of the limb. Extension of the limb much beyond its comfortable operating region results in a highly rigid state that seeks to prevent further extension that may damage the limb. In this way, the limb acts so as to maintain its structural integrity.

In conclusion, we have found that the cat limb opposes displacements of its supporting surface in the sagittal plane with a response that is maximal along the direction from the endpoint, or paw, to the pivot, or shoulder. The responses are qualitatively similar whether the cat in anaesthetized or not, indicating that they are a geometric constraint of the limb itself. The stiffness ellipsoid model is an insufficient representation of the force response of the cat limb to perturbations that displace it outside to the regime where short-range stiffness would apply. As previously stated, research examining postural control has posited that the asymmetry indicated by high curl could only be as a result of neural feedback between muscles [29]. There was no difference in the relative non-spring-like components of stiffness between the passive and active states in our experiments, further indicating that asymmetric reflex gains did not play an important part, if any, in the response. Under normal conditions the cat's limbs preferentially respond to perturbations of its supporting surface to maintain weight support. Extension of the limbs beyond normal length or angle shifts the limbs in to a regime wherein they preferentially respond so as to prevent further extension and potential damage. Contrary to what is observed in the horizontal plane, the forelimb is

more force constrained than the hindlimb in the sagittal plane, clearly suggesting a preference for tasks involving high vertical forces.

CONCLUSION

This research project had two main objectives: (i) to establish that the forelimb is sufficiently different from the hindlimb to warrant exploration of its neuromechanical properties; and (ii) To incorporate these properties within a computational model, and (iii) to experimentally explore an aspect of postural control and to validate the accuracy and viability of the neuromusculoskeletal model to do likewise.

The forelimb was found to be significantly smaller (by approximately 40% by mass) than the hindlimb and so cannot contribute as much to propulsion. Further evidence for the forelimb's diminished role in propulsion comes from the observation that its most powerful proximal muscles have pulling directions that are not in the sagittal plane. They strongly suggest, as has been done in other species, that the forelimb is actually the initiator of turning in the animal. Further grounds for this conclusion are provided in the form of strong digital flexors capable of pressing into the ground during these high-velocity movements.

Unlike the hindlimb, which functions along the anatomical lines of flexor-extensor action, display more diverse recruitment of its muscles in a more task-specific manner.

In studies involving the locomoting cat, the forelimb has been shown to make use of more muscle synergies than the hindlimb [2], suggesting that more complex control is required in the forelimb than in the hindlimb.

The moment arms at the ankle have been shown to possess intrinsic limb stabilizing ability in abduction-adduction and inversion-eversion [105]. The forelimb did

not exhibit any moment arms that actively worked to stabilize the joint, although one of the muscles decreased the available torque at the joint.

The current work, together with the aforementioned previous studies, supplied sufficient proof that the forelimb and hindlimb possess distinct structural characteristics that manifest themselves in their function and provided the impetus for further examination of the forelimb.

A musculoskeletal model was successfully implemented utilizing the measured and calculated parameter in a Hill-type model. The skeletal structure was composed of rigid bodies and the joints were determined from recorded kinematic data. The muscles were mapped to the skeletal frame, from multiple specimens, by employing digitized data of the attachment and bony landmarks. All the specimens underwent transformations to be combined into a prototypical model. The model was then validated against experimentally recorded moment arms. The quality of the fits was better for the elbow and ulnar deviators than for the radial deviators.

The aspect of postural control we wanted to experimentally test was that of the forelimb's force response to translational perturbations of the supporting surface in the sagittal plane. In our experiments the behavior in the sagittal plane was force constrained. Previous experiments of the forelimb's behavior in the horizontal plane showed that it could be modeled as being one extreme of an ellipsoid model, that of a uniform model [8, 9]. However, later experiments showed that the forelimb exhibited what was described as force constrained behavior [14, 169]. The combination of these results seems to suggest that the forelimb may in fact exhibit force constrained behavior.

Our results indicated that this anisotropy in the forelimb is greater than that found in the hindlimb, unlike Macpherson's [8, 9] results in the horizontal plane.

This force response is not fully represented by a stiffness ellipse, perhaps indicating the need for a viscosity ellipse, or a combination of the two. Research has indicated that a stiffness ellipse suitably models the response to minute, stochastic perturbations [165] where the muscles remain within the short-range regime. Outside this region, muscles are subject to viscous effects due to cross-bridge dynamics of breaking and re-attaching [170]. The current work has demonstrated that the perturbations employed causes muscles to be stretched outside this region (1.30±0.05 % change in muscle length) resulting in the asymmetric force response observed.

The forelimb model as it currently stands is not yet ready to model the precise conditions of the experimental setup. Specifically, length feedback was included, which allowed the limb to present some stiffness response when perturbed. The anaesthetized state cannot be modeled with this scenario. The active preparation also cannot be fully modeled as the decerebrate preparation still leaves the brain stem intact, and those inputs are not part of the model. However, the model limb still was able to provide a proof of concept. In fact, the phenomenological Hill model employed demonstrates most of the essential features found in the experiment, namely (i) it generates restorative forces to the perturbation, with the direction of maximal stiffness along the vertical limb axis; (ii) it generates an asymmetric force magnitude response when modeled with a stiffness ellipse; and (iii) it generated an accurate directional pattern of force constraint in the extended position but not in the crouched position.

5.1 Future Directions

A natural step now that a forelimb model has been implemented is to combine it with the existing hindlimb model to obtain a complete four-legged cat model with which one could evaluate various levels of control of posture and locomotion. One example would be to determine how much of a gain to maintenance of stability would be achieved by the inclusion of force feedback. Another would be to add in the Ia connections, both bi-directional and uni-directional, separately and together, to determine the effect on posture or even locomotion.

Unlike the hindlimb that is connected to the trunk at the pelvis, the forelimb is only connected via muscle and so floats under the skin. To carry out our study we clamped it by the spine of the scapula to keep it immobile. Doing so may have increased the rigidity to an extent that the limb was much more force constrained than it is in the intact cat. A follow-up study would be to perform the experiments without the scapula clamped to determine how much it affects the stiffness/force response and to what degree the damping alters the strategy employed.

The result that stability in inherently mechanical and is scaled by neural input to accommodate the disturbance potentially simplifies the problem of control in the area of bio-inspired robotics. It means that one would only have to regulate the gain to the joint actuators to achieve the appropriate level of stiffness to maintain postural stability.

Finally, the model could also be used within the medical, and in particular rehabilitation, fields to evaluate the possible effects of various interventions and injuries. One such example would be tendon transfer surgery. Muscles in the model can be detached from their initial position and reattached at another site and the force response

to perturbations determined as in this study or the kinematics of overground locomotion examined. In this way, the benefits and drawbacks could be ascertained before undertaking a medical procedure.

APPENDIX A

Table A.1: Fiber and Sarcomere lengths.

Muscle	NeuroMech Name	Abbr	Muscle Mass (g)	Fiber Length (mm)	Sarcomere Length (um)
Acromiodeltoideus	ad	ACD	2.79±0.47	13.61±0.6	2.61±0.41
Spinodeltoideus	sd	SPD	3.54±1.01	35.26±0.4	2.62±0.46
Teres Major	tj	TMA	8.47±1.36	52.96±0.38	2.84±0.61
Teres Minor	tn	TMI	0.93±0.22	13.74±0.16	2.8±0.37
Supraspinatus	sps	SPS	17.23±1.84	26.74±1.33	2.38±0.24
Coracobrachialis	cb	CCB	0.31±0.04	12.3±0.25	2.74±0.08
Subscapularis	ssc	SSC	15.37±1.8	14.92±1.19	2.65±0.2
Infraspinatus	if	INF	13.15±1.7	17.01±1.07	2.3±0.37
Biceps brachii	bb	BBI	5.85±0.98	29±0.81	2.95±0.41
Brachialis	br	BRA	3.47±0.35	42.75±0.22	3.23±0.56
Brachioradialis	bcd	BRR	0.8±0.21	112.34±0.03	3.2±0.57
Epitrochlearis	ept	EPI	1.95±0.51	37.1±0.16	3.03±0.41
Triceps Brachii Longus	tlong	TBG	22.89±3.93	22.09±2.75	2.29±0.48
Triceps brachii medialis	tmed	TBM	5.55±0.38	31.43±0.21	2.7±0.54
Triceps Brachii Lateralis	tlat	TBL	9.01±2.19	34.01±0.84	2.27±0.28
Anconeus	anc	ANC	2.04±0.13	18.14±0.13	2.13±0.44
Pronator Teres	pt	PRT	1.62±0.28	12.84±0.73	2.75±0.22
Supinator	sup	SUP	0.86±0.16	6.95±0.31	2.33±0.45
Flexor Carpi radialis	fcr	FCR	1.26±0.17	14.88±0.14	2.95±0.23
Flexor Carpi Ulnaris	fcu	FCU	4.01±0.32	11.16±0.31	2.42±0.34
Flexor digitorum profundus	fdp	FDP	9.27±2	24.68±1.07	2.89±0.31
Flexor Digitorum Superficialis	fds	FDS	0.18±0.05	6.2±0.07	2.65±0.28
Palmaris Longus	pl	PAL	2.61±0.55	10.95±0.61	2.44±0.01
Extensor carpi radialis	ecr	ECR	4.03±0.53	46.14±0.64	3.26±0.8
Extensor Carpi Ulnaris	ecu	ECU	1.78±0.17	11.49±0.23	2.69±0.36
Extensor digitorum communis	edc	EDC	1.99±0.17	25.9±0.21	2.99±0.29
Extensor digitorum lateralis	edlat	EDL	1.22±0.12	19±0.23	3.33±0.48
Extensor pollicis longus	epl	EPL	0.55±0.07	22.95±0.08	2.68±0.24
Abductor pollicis longus	apl	APL	1.82±0.27	12.01±0.25	2.76±0.3

Table A.2 Digitization data for all specimens. Cat 1

	X (mm)		Y(mm)		Z(mm)	
point						
adi	-5.25	±1.03	-80.00	±2.32	27.13	±1.03
ado	-8.82	±1.00	-97.94	±0.86	37.05	±1.25
al	20.33	±0.53	-141.94	±2.61	48.50	±0.69
am	-35.56	±5.98	-147.73	±1.38	-13.14	±7.25
apli	-15.77	±1.56	51.61	±3.35	-1.89	±2.97
aplo	20.94	±1.93	-0.94	±20.37	-6.39	±6.51
aplr	-14.47	±0.73	47.55	±1.89	0.06	±1.29
bbo	-23.85	±0.69	-96.55	±1.69	28.03	±0.76
bi	30.42	±1.02	-30.77	±1.14	-14.02	±1.47
bl	37.78	±1.10	-138.62	±1.40	23.98	±0.72
bm	-15.05	±6.06	-143.57	±1.50	-38.13	±7.54
bo	-5.53	±1.68	-78.98	±1.41	23.85	±1.69
bri	-9.75	±1.18	42.17	±4.86	6.20	±2.92
bro	4.36	±0.48	-69.06	±0.75	9.38	±1.68
cbi	-14.88	±0.66	-78.47	±0.66	18.76	±1.09
cbo	-25.26	±0.56	-100.19	±0.81	24.45	±0.88
cl	26.93	±1.71	-52.35	±1.11	30.59	±1.76
cm	-22.47	±0.82	-66.51	±1.04	-38.07	±0.70
dl	52.49	±1.00	-4.30	±3.25	18.09	±1.41
dm	-40.51	±1.07	-22.71	±2.03	-77.85	±2.01
eci	36.37	±3.04	-37.36	±2.39	-18.63	±0.93
ecri	-16.17	±1.42	48.41	±0.89	8.92	±0.89
ecro	31.21	±0.84	-49.43	±1.08	-5.43	±1.24
ecui	1.43	±1.19	61.62	±2.36	2.58	±1.16
ecuo	39.14	±1.31	-30.66	±1.09	-5.65	±1.68
ecur	3.70	±1.23	56.33	±1.82	3.64	±1.06
edci2	-19.95	±1.38	90.03	±2.35	-5.03	±1.03
edci3	-15.22	±1.30	98.40	±4.15	-1.60	±1.10
edci4	-8.43	±0.88	97.23	±3.74	0.44	±1.80
edci5	-1.43	±1.04	91.40	±1.21	-0.94	±1.18
edco	33.77	±1.34	-42.26	±1.97	-1.86	±0.90
edcr	-5.76	±0.97	52.12	±1.70	7.24	±1.06
edlati2	-19.49	±1.25	90.35	±2.63	-4.92	±1.17
edlati3	-15.12	±1.13	98.09	±4.60	-1.43	±1.25
edlati4	-8.93	±1.09	97.43	±3.79	0.57	±1.70
edlati5	-1.36	±1.07	91.27	±1.33	-0.74	±1.36
edlato	36.24	±1.15	-35.26	±1.15	-2.09	±0.45
edlatr	-0.28	±0.89	54.54	±1.53	6.10	±1.05
epli1	-15.16	±0.80	52.67	±2.40	-1.10	±1.95
epli2	-25.37	±0.79	88.08	±0.77	-5.96	±0.90
eplo	30.74	±6.86	-7.68	±13.96	-8.52	±2.72
eplr	-5.04	±0.84	51.25	±0.98	6.32	±1.21
fcri	-6.45	±1.41	52.06	±2.11	-5.95	±1.40
fcro	27.40	±0.80	-33.89	±0.66	-20.22	±0.87

Table A.2 continued

fcrr	-6.43	±1.70	51.06	±4.84	-6.62	±1.96
fcui	3.70	±2.11	57.29	±4.07	-4.35	±2.96
fcuo	34.74	±1.51	-36.27	±1.53	-15.61	±2.82
fcur	5.51	±1.27	52.58	±3.49	-4.44	±3.17
fdpi1	-12.17	±2.32	62.10	±1.10	-12.81	±0.87
fdpi2	-16.43	±2.97	84.20	±1.20	-12.63	±0.85
fdpi3	-12.64	±3.30	91.25	±1.27	-9.09	±0.35
fdpi4	-6.72	±3.37	90.90	±1.32	-7.28	±1.80
fdpi5	-0.51	±2.68	85.30	±1.43	-8.69	±1.53
fdpo	32.47	±1.03	-32.32	±0.79	-18.80	±0.43
fdpr	-5.61	±0.72	50.32	±0.65	-5.95	±0.65
fdsi2	-13.91	±0.79	84.28	±1.42	-12.81	±0.62
fdsi3	-9.26	±2.67	90.62	±1.20	-10.02	±0.85
fdsi4	-3.68	±3.50	89.36	±1.82	-9.53	±1.21
fdsi5	1.50	±0.49	84.33	±0.98	-9.76	±0.94
fdso	7.47	±0.51	31.46	±0.52	-8.49	±0.63
flmcp	-6.59	±3.01	75.66	±4.92	1.61	±4.85
fmmcp	-25.39	±3.81	71.57	±5.75	-3.53	±4.63
ftb	-17.41	±2.59	46.51	±5.37	1.25	±4.73
hgt	-23.12	±1.11	-79.35	±1.94	29.38	±2.56
hle	40.32	±1.79	-35.90	±0.89	-6.68	±2.57
hme	27.44	±1.42	-36.94	±0.44	-22.33	±2.36
isi	-16.34	±0.58	-89.52	±1.12	34.07	±0.66
iso	17.83	±0.85	-149.72	±2.67	9.01	±1.13
isr	-1.71	±0.27	-99.90	±0.89	27.15	±0.73
pli1	-10.79	±1.22	64.80	±6.98	-11.71	±2.11
pli2	-14.50	±1.44	87.20	±3.74	-12.13	±2.26
pli3	-10.20	±1.81	93.91	±2.92	-9.33	±2.13
pli4	-4.65	±1.89	92.96	±2.79	-7.68	±1.91
pli5	-0.21	±3.79	85.10	±9.03	-8.61	±1.87
plo	27.67	±0.73	-36.87	±1.58	-20.34	±0.81
plr	-3.69	±1.43	54.10	±2.81	-7.28	±1.86
pti	11.88	±1.93	-0.06	±3.45	0.48	±1.96
pto	23.99	±0.91	-37.60	±0.22	-19.26	±1.32
rh	39.51	±0.49	-30.77	±1.26	-5.93	±1.30
rsp	-15.97	±2.33	39.03	±3.80	6.11	±5.16
rus	-7.58	±1.05	42.58	±0.62	13.00	±1.78
sa	-0.04	±0.44	-101.43	±1.28	27.44	±1.32
sca	25.09	±0.72	-134.09	±0.98	-2.69	±0.54
sdi	-5.47	±0.86	-79.30	±0.92	26.78	±0.35
sdo	8.68	±0.50	-132.91	±2.18	25.04	±1.17
si	14.80	±1.25	-4.98	±0.39	0.94	±1.08
so	37.83	±1.62	-27.89	±0.49	-6.12	±0.61
ssci	-20.96	±1.12	-91.09	±0.69	17.47	±0.83
ssco	7.22	±0.72	-152.12	±0.90	10.75	±0.95
ssi	-21.31	±0.44	-83.46	±0.84	37.31	±0.25
sso	-8.26	±1.82	-155.92	±1.63	24.66	±1.32

Table A.2 continued

svs	8.66	±0.64	-156.34	±1.12	14.68	±0.87
tji	-9.62	±0.80	-74.53	±1.07	20.62	±0.66
tjo	25.54	±0.33	-138.12	±3.07	-1.25	±0.91
tlati	40.63	±0.57	-34.44	±1.52	-11.52	±1.18
tlato	-9.38	±0.56	-87.07	±0.62	26.96	±0.92
tlongi	41.42	±0.72	-45.74	±1.66	-18.24	±1.00
tlongo	-11.66	±0.63	-100.80	±0.76	18.36	±0.34
tmedo	-11.05	±0.44	-74.75	±0.78	16.80	±0.82
tmedsi	42.63	±0.68	-43.22	±0.55	-26.30	±0.64
tmedso	30.13	±2.20	-40.19	±0.79	-23.75	±1.40
tni	-11.16	±0.76	-86.96	±1.17	31.00	±1.03
tno	0.15	±1.08	-114.53	±0.68	17.77	±0.25
uop	45.22	±1.93	-41.35	±1.57	-21.10	±4.30
usp	1.13	±5.15	47.99	±3.42	5.71	±4.43

Table A.3 Digitization data for all specimens. Cat 2

	X (mm)		Y (mm)		Z (mm)	
point						
adi	-29.36	±1.03	-68.59	±1.72	-50.19	±0.85
ado	-36.86	±1.03	-86.90	±0.54	-62.70	±1.44
ai	18.65	±1.67	-15.80	±1.65	-20.38	±3.23
al	-34.92	±0.97	-110.08	±0.79	-109.98	±0.76
am	-81.81	±1.04	-48.32	±0.75	-121.47	±0.70
ao	-4.00	±2.54	-38.88	±1.79	-34.36	±4.05
apli	6.44	±2.16	30.44	±3.35	77.11	±3.50
aplo	19.16	±1.95	-15.19	±1.26	-5.63	±4.50
aplr	7.51	±1.87	16.99	±1.73	77.87	±3.83
bbi	3.34	±2.82	-15.40	±1.87	-10.31	±4.44
bbo	-53.49	±1.67	-80.93	±1.51	-65.09	±3.36
bi	7.74	±2.29	-13.99	±6.71	-12.81	±3.30
bl	-20.72	±1.52	-96.66	±0.97	-119.94	±2.13
bm	-62.19	±2.83	-45.41	±1.60	-149.08	±2.56
bo	-29.56	±1.84	-68.77	±1.54	-48.25	±3.20
bri	13.16	±2.83	8.56	±1.47	74.10	±2.57
bro	-15.73	±3.12	-48.33	±2.01	-42.57	±3.07
cbi	-40.35	±0.99	-62.04	±1.10	-51.84	±1.36
cbo	-56.79	±1.12	-79.70	±2.02	-70.89	±1.21
cl	31.47	±1.32	-21.98	±1.57	-18.23	±1.67
cm	-72.49	±1.13	-8.33	±0.81	-51.06	±2.73
dl	21.73	±2.08	-1.20	±1.73	61.59	±2.08
dm	-51.11	±0.85	-0.60	±0.84	-41.40	±0.75
eci	12.61	±1.00	-6.24	±1.13	-31.06	±0.63
eco	-25.15	±0.94	-57.22	±1.10	-69.31	±0.98
ecri	14.74	±2.17	34.28	±1.38	84.28	±3.47
ecro	2.62	±2.28	-32.15	±1.41	-30.53	±3.46
ecui	29.31	±0.71	29.75	±1.22	73.20	±1.19
ecuo	20.74	±1.30	-18.02	±1.25	-16.26	±1.18
ecur	31.03	±0.75	22.84	±1.29	74.20	±0.97
edci2	16.32	±0.59	70.66	±1.28	74.59	±1.27
edci3	24.62	±0.89	79.29	±1.15	69.07	±1.26
edci4	30.59	±0.90	74.98	±1.07	67.16	±1.35
edci5	34.59	±0.61	64.32	±0.44	66.53	±1.34
edco	11.89	±1.38	-26.12	±0.84	-24.02	±1.20
edcr	22.68	±0.68	16.92	±1.93	79.77	±1.53
edlati2	16.19	±0.65	70.76	±0.80	74.93	±1.18
edlati3	24.66	±0.63	79.58	±1.15	68.88	±1.49
edlati4	30.82	±0.77	75.02	±1.31	67.12	±1.48
edlati5	34.42	±1.26	64.25	±1.06	66.69	±1.08
edlato	15.98	±2.21	-25.07	±1.19	-20.75	±1.59
edlatr	27.88	±0.54	20.46	±1.15	78.60	±0.68
em	-30.20	±1.78	29.91	±1.60	-28.62	±5.36
epli1	7.25	±1.60	37.48	±1.06	78.24	±0.79
epli2	12.84	±1.53	54.79	±1.27	75.65	±0.80

Table A.3 continued

eplo	21.88	±0.68	-9.34	±1.68	-9.66	±5.20
eplr	22.99	±2.01	15.92	±2.65	78.52	±2.20
epo	21.10	±0.34	-8.10	±1.89	-6.97	±3.11
fcri	8.77	±2.48	22.95	±1.36	71.74	±0.25
fcro	3.06	±1.78	-5.03	±1.47	-19.79	±1.08
fcrr	11.86	±0.96	22.90	±1.59	70.17	±1.31
fcui	25.15	±1.61	29.00	±1.68	65.24	±3.31
fcuo	14.75	±1.59	-5.06	±0.78	-26.32	±0.47
fcur	23.22	±1.64	26.28	±2.18	63.11	±2.89
fdpi1	8.48	±1.68	37.90	±2.52	69.52	±2.53
fdpi2	11.10	±1.46	63.06	±1.69	65.65	±1.48
fdpi3	19.73	±1.42	69.66	±1.40	61.85	±1.53
fdpi4	24.50	±1.67	67.69	±1.10	58.92	±1.26
fdpi5	27.99	±1.54	58.31	±1.16	57.44	±1.18
fdpo	7.47	±1.02	-6.96	±1.39	-17.42	±1.40
fdpr	12.71	±3.01	27.66	±5.78	69.18	±0.86
fdsi2	12.10	±1.49	62.50	±0.58	65.87	±0.67
fdsi3	19.24	±0.78	69.07	±2.34	62.07	±0.90
fdsi4	24.38	±1.03	68.12	±0.70	58.43	±1.27
fdsi5	27.65	±0.63	58.89	±1.23	57.13	±0.46
fdso	15.40	±0.74	22.34	±0.33	51.55	±1.10
flmcp	27.61	±2.36	49.71	±9.20	67.19	±3.24
fm	-25.91	±1.83	59.27	±0.77	31.95	±1.96
fmmcp	8.26	±5.56	56.64	±2.05	76.62	±4.13
ftb	5.49	±1.24	33.36	±7.42	79.34	±3.32
hgt	-51.59	±2.14	-79.49	±1.20	-49.58	±2.84
hle	15.95	±0.86	-24.64	±0.82	-14.09	±1.62
hme	-0.53	±1.21	-7.31	±0.86	-18.79	±2.14
isi	-40.62	±0.84	-85.85	±0.56	-56.29	±1.01
iso	-23.34	±1.06	-86.10	±1.24	-134.81	±1.38
pli1	9.93	±0.77	38.22	±1.03	67.75	±1.16
pli2	13.26	±1.21	62.68	±1.15	66.01	±1.53
pli3	20.42	±1.42	69.65	±1.66	62.68	±1.13
pli4	26.10	±1.58	68.03	±1.40	59.83	±2.06
pli5	29.61	±1.50	58.12	±1.17	56.81	±1.74
plo	6.36	±0.92	-4.33	±1.50	-20.83	±2.77
plr	13.86	±0.85	25.41	±1.11	69.28	±1.23
pti	7.21	±1.49	-6.41	±0.70	13.61	±1.86
pto	-3.03	±1.48	-11.31	±0.45	-18.53	±1.83
rh	16.99	±1.24	-21.29	±1.85	-7.66	±3.14
rsp	7.98	±1.41	15.72	±2.36	79.48	±2.15
rus	21.58	±0.67	22.43	±1.79	75.53	±0.44
rusp	10.75	±0.32	-13.54	±0.48	-2.77	±0.73
sa	-27.63	±1.51	-82.03	±1.28	-82.83	±2.66
sca	-19.10	±2.01	-71.30	±1.16	-135.74	±3.67
sdi	-29.01	±0.71	-68.15	±1.77	-50.10	±1.32

Table A.3 continued

sdo	-33.58	±0.52	-96.68	±0.74	-115.41	±2.37
si	12.74	±2.22	-6.96	±1.28	31.85	±4.07
so	11.59	±2.05	-21.11	±1.85	-3.72	±3.97
ssci	-53.12	±0.41	-67.34	±0.36	-65.43	±1.51
ssco	-36.27	±0.59	-87.20	±0.53	-127.93	±1.18
ssi	-54.29	±1.48	-82.57	±1.54	-51.15	±1.51
sso	-43.28	±2.02	-101.47	±0.80	-131.42	±2.37
svs	-39.49	±1.76	-98.58	±1.90	-138.59	±1.46
tji	-40.43	±0.52	-63.31	±0.57	-42.22	±1.33
tjo	-14.70	±0.30	-73.60	±1.10	-131.91	±1.02
tlati	18.70	±0.88	-14.02	±0.99	-25.00	±1.41
tlato	-38.68	±0.30	-73.51	±0.70	-57.01	±1.26
tlongi	15.39	±1.19	-12.81	±1.29	-38.44	±1.02
tlongo	-43.59	±0.29	-72.84	±0.19	-79.07	±0.18
tmedi	8.44	±1.56	-13.37	±0.84	-33.81	±0.81
tmedo	-38.15	±0.80	-60.80	±0.74	-51.46	±1.08
tmedsi	9.73	±0.42	-11.58	±1.37	-30.42	±1.70
tmedso	-3.49	±0.73	-14.35	±1.45	-20.99	±2.20
tni	-38.07	±2.18	-77.93	±1.83	-56.42	±7.95
tno	-33.21	±1.57	-76.16	±1.14	-89.09	±12.36
uop	14.57	±0.80	-12.92	±1.29	-32.61	±1.71
usp	27.47	±1.23	24.98	±2.43	71.51	±2.47

Table A.4 Digitization data for all specimens. Cat 3

	X (mm)		Y (mm)		Z (mm)	
adi	8.47	±0.81	-7.69	±0.72	-88.80	±1.30
ado	6.03	±0.60	-14.31	±0.48	-114.71	±1.50
ai	38.14	±1.71	20.03	±2.49	-21.54	±0.86
al	21.33	±1.42	-25.74	±1.18	-145.39	±1.07
am	-51.24	±0.91	50.30	±0.77	-135.28	±1.83
ao	30.75	±1.57	11.66	±2.00	-42.70	±1.20
apli	-27.31	±2.74	-3.46	±5.30	60.23	±2.41
aplo	28.75	±2.40	11.42	±3.14	-9.37	±2.64
aplr	-27.86	±2.74	-8.14	±5.04	51.82	±2.42
bbi	19.33	±1.06	14.20	±0.23	-17.82	±1.20
bbo	-6.98	±1.73	-9.25	±1.18	-111.58	±1.51
bi	20.94	±1.21	13.04	±1.65	-21.61	±0.61
bl	27.96	±1.80	-24.60	±1.56	-72.26	±1.04
bm	-41.52	±1.22	59.26	±1.22	-70.82	±1.84
bo	5.32	±10.70	-6.91	±3.48	-72.08	±50.36
bri	-24.95	±5.02	-15.69	±14.46	46.42	±4.45
bro	14.83	±0.34	3.35	±0.24	-70.74	±0.98
cbo	-9.68	±1.30	-2.45	±1.26	-113.24	±1.67

Table A.4 continued

cl	47.58	±1.22	-11.27	±2.43	-6.86	±0.82
cm	-25.11	±1.80	54.04	±4.68	-15.00	±10.83
dl	14.74	±2.34	-44.88	±3.23	81.26	±1.80
dm	-56.90	±2.36	32.26	±3.95	86.75	±1.51
eci	26.87	±18.77	17.13	±18.14	-3.17	±33.70
eco	15.93	±1.57	13.77	±1.25	-102.82	±1.48
ecri	-33.41	±2.36	-14.13	±0.06	63.29	±3.62
ecro	28.21	±0.77	11.03	±0.09	-43.08	±0.30
ecui	-10.53	±4.12	-19.90	±0.73	65.23	±1.64
ecuo	36.82	±3.95	12.60	±1.02	-18.88	±0.89
ecur	-7.87	±4.25	-19.61	±0.83	59.26	±1.52
edci2	-26.63	±1.71	-9.21	±0.94	94.50	±1.91
edci3	-23.34	±1.79	-13.22	±1.01	97.83	±1.16
edci4	-19.64	±1.67	-18.01	±0.87	98.21	±1.28
edci5	-15.28	±1.78	-21.49	±0.89	92.74	±1.17
edco	33.52	±1.21	9.14	±1.13	-31.00	±1.68
edcr	-22.11	±1.73	-18.64	±1.76	55.40	±2.98
edlati2	-26.64	±1.88	-9.11	±1.02	94.68	±1.40
edlati3	-23.35	±2.01	-13.28	±1.03	97.63	±1.28
edlati4	-19.66	±2.15	-18.12	±1.04	98.13	±1.16
edlati5	-15.21	±1.80	-21.58	±1.14	92.77	±0.94
edlato	31.36	±13.37	5.45	±6.44	-20.15	±19.27
edlatr	-15.28	±1.54	-20.95	±0.80	58.59	±1.41
em	-25.80	±2.19	35.71	±3.67	36.73	±1.76
epli1	-28.03	±1.54	-5.61	±4.16	72.38	±2.12
epli2	-27.42	±1.74	-7.95	±4.63	93.93	±2.66
eplo	32.13	±1.31	13.05	±2.48	-9.65	±1.04
eplr	-19.86	±1.95	-19.19	±4.12	57.39	±2.37
fcri	-18.74	±2.33	-4.45	±4.52	60.69	±1.92
fcro	20.27	±3.13	24.42	±2.10	-25.98	±1.14
fcrr	-18.39	±2.64	-4.09	±4.10	54.37	±2.06
fcui	-7.41	±2.77	-9.09	±3.73	64.62	±1.16
fcuo	30.07	±0.59	25.98	±0.67	-23.44	±0.46
fcur	-5.61	±3.84	-7.72	±3.23	60.22	±1.43
fdpi1	-20.70	±1.38	-0.16	±4.50	72.47	±7.91
fdpi2	-19.95	±2.15	-0.82	±5.27	99.06	±2.65
fdpi3	-17.49	±2.14	-5.39	±5.15	105.25	±1.97
fdpi4	-12.71	±2.58	-8.70	±4.91	103.89	±2.83
fdpi5	-8.05	±5.08	-11.58	±6.35	94.96	±8.93
fdpo	23.39	±1.16	27.72	±2.46	-23.31	±0.88
fdpr	-16.91	±2.11	-2.46	±5.67	54.21	±1.78
fdsi2	-19.57	±1.52	-3.06	±1.53	99.52	±1.02
fdsi3	-17.03	±1.33	-7.80	±1.41	106.56	±1.26
fdsi4	-12.67	±1.22	-10.28	±1.10	105.54	±0.98
fdsi5	-5.66	±1.18	-13.99	±1.64	98.95	±1.07

Table A.4 continued

fdso	-4.38	±0.85	0.57	±1.35	44.77	±1.17
flmcp	-17.07	±1.03	-21.45	±0.50	88.18	±0.13
fmmcp	-28.48	±3.52	-1.73	±6.32	89.01	±2.15
ftb	-27.19	±3.01	-3.21	±5.47	61.14	±1.76
hgt	-7.20	±1.07	-15.69	±0.79	-99.45	±1.63
hle	37.44	±1.74	12.03	±2.06	-25.67	±0.95
hme	21.50	±1.69	27.82	±1.97	-26.42	±0.84
isi	1.07	±0.87	-16.10	±0.57	-106.96	±0.89
iso	35.20	±1.02	24.82	±0.89	-166.92	±0.58
isr	14.60	±1.03	-8.68	±0.51	-115.52	±0.90
pli1	-18.67	±3.46	-1.78	±1.01	71.99	±1.25
pli2	-19.34	±2.70	-2.57	±0.95	99.32	±1.13
pli3	-16.53	±2.74	-7.74	±1.26	106.41	±1.29
pli4	-12.11	±3.18	-10.08	±0.83	105.40	±1.16
pli5	-5.72	±2.85	-14.57	±1.44	98.09	±1.70
plmcp	-10.91	±2.82	-18.56	±7.25	88.94	±1.64
plo	21.18	±1.39	24.71	±0.96	-22.78	±0.72
plr	-13.46	±4.79	-5.39	±0.97	58.58	±1.30
pti	4.60	±1.83	4.86	±4.48	3.34	±1.26
pto	20.13	±1.46	25.79	±2.09	-28.63	±0.59
rh	33.82	±1.42	9.05	±1.90	-19.20	±2.34
rsp	-27.15	±2.67	-6.91	±5.39	50.92	±2.91
sa	16.29	±4.30	-8.35	±3.18	-117.59	±3.07
sca	41.79	±1.03	33.69	±2.01	-154.00	±1.03
sdi	8.40	±1.48	-8.06	±0.39	-88.85	±1.86
sdo	24.95	±0.47	9.08	±0.65	-156.87	±2.19
si	-0.02	±1.43	-1.38	±0.17	8.32	±0.69
so	30.91	±0.60	8.17	±0.67	-19.62	±0.30
ssci	-6.13	±0.55	2.92	±0.44	-102.26	±0.48
ssco	17.91	±0.36	17.02	±0.32	-161.18	±0.31
ssi	-11.33	±0.32	-15.22	±0.41	-100.41	±1.98
sso	7.63	±1.71	7.82	±0.41	-173.13	±0.89
svs	23.66	±1.72	18.35	±2.69	-177.92	±0.68
tji	-1.49	±0.82	1.06	±0.66	-90.11	±1.15
tjo	43.12	±0.91	34.37	±0.52	-155.99	±0.94
tlati	39.73	±1.54	20.25	±1.37	-24.29	±1.30
tlato	4.86	±0.63	-7.32	±1.12	-98.04	±0.71
tlongi	41.47	±1.23	27.72	±1.03	-30.07	±1.59
tlongo	2.70	±1.09	2.29	±0.41	-113.92	±0.98
tmedi	37.34	±0.47	28.95	±0.06	-32.54	±0.00
tmedo	5.01	±1.22	2.63	±0.76	-100.37	±0.84
tni	6.40	±1.83	-12.00	±0.81	-100.22	±1.35
tno	15.47	±1.45	6.28	±0.99	-124.01	±2.06
uop	41.75	±1.70	30.64	±1.84	-26.85	±1.25
usp	-8.01	±2.94	-14.32	±5.04	59.18	±1.45

Table A.5 Digitization data for all specimens. Cat 4

	X (mm)		Y (mm)		Z (mm)	
adi	7.88	±1.36	49.14	±1.93	11.32	±0.92
ado	31.37	±0.27	83.50	±0.34	38.33	±0.76
al	73.88	±0.47	57.36	±0.66	98.79	±0.62
am	-14.67	±0.41	118.17	±0.36	83.37	±0.54
anci	-18.74	±1.62	-0.39	±1.46	22.06	±1.72
anco	1.22	±1.37	44.65	±2.73	24.49	±0.47
apli	-50.92	±1.15	-30.94	±0.93	-78.01	±0.18
aplo	-20.10	±1.74	-4.80	±1.42	12.30	±2.56
aplr	-37.87	±1.88	-25.18	±1.18	-73.12	±0.72
bbi	-26.50	±1.11	-0.56	±0.66	1.89	±0.59
bbo	19.03	±1.82	90.56	±2.41	26.36	±3.35
bl	67.28	±0.44	28.65	±0.40	29.50	±0.42
bm	-13.02	±0.37	91.24	±0.57	7.60	±0.60
brdi	-33.27	±3.63	-23.14	±1.38	-64.95	±3.29
brdo	8.23	±0.96	54.17	±1.71	24.71	±0.37
brdotom	8.32	±2.01	37.79	±3.96	15.45	±1.25
bri	-18.64	±0.78	4.29	±0.55	6.38	±1.05
bro	20.37	±1.02	66.49	±1.87	21.32	±1.02
brotom	11.88	±2.05	51.71	±1.74	14.09	±1.28
cbi	16.06	±0.66	75.05	±0.83	13.19	±0.72
cbo	15.69	±2.46	89.88	±0.94	22.68	±2.16
cl	31.27	±0.32	-40.27	±0.54	12.92	±0.41
cm	-60.92	±0.41	9.12	±0.48	-0.55	±0.54
dl	-61.44	±0.94	-84.51	±0.83	-48.09	±0.86
dm	-59.14	±0.80	-39.31	±1.15	-121.13	±0.62
eci	-34.10	±0.98	6.74	±0.77	18.28	±2.02
eco	-1.06	±0.36	64.20	±0.96	41.30	±1.25
ecri	-48.35	±0.54	-40.82	±0.47	-90.82	±0.40
ecro	-5.59	±0.50	18.97	±0.76	22.52	±0.23
ecui	-42.99	±1.35	-48.03	±0.97	-74.43	±1.71
ecuo	-18.97	±0.95	-3.38	±3.14	17.55	±4.89
ecur	-36.37	±0.84	-43.06	±1.04	-64.93	±1.88
edci2	-59.20	±1.97	-53.03	±3.35	-107.98	±4.96
edci3	-54.28	±1.24	-56.53	±2.01	-102.95	±1.79
edci4	-56.07	±1.57	-61.98	±1.88	-95.11	±0.94
edci5	-60.47	±0.83	-65.50	±2.85	-91.19	±2.00
edco	-9.94	±2.04	7.72	±3.43	23.25	±4.59
edcr	-33.52	±1.19	-32.70	±1.03	-70.91	±2.43
edlati2	-59.68	±1.87	-53.13	±3.23	-109.01	±4.47
edlati3	-54.25	±1.25	-56.54	±2.02	-102.77	±1.50
edlati4	-56.07	±1.88	-61.81	±2.30	-94.98	±1.27
edlati5	-60.27	±1.03	-65.82	±3.06	-91.43	±2.35
edlato	-13.10	±2.13	1.70	±1.07	21.40	±2.62
edlatr	-32.78	±0.91	-37.92	±0.98	-65.23	±1.82
el	6.32	±0.45	-49.99	±0.51	-48.76	±0.44

Table A.5 continued

epli1	-52.21	±1.49	-38.27	±0.26	-90.97	±1.69
epli2	-58.50	±0.42	-48.97	±0.60	-102.50	±0.41
eplo	-22.34	±1.24	-4.00	±1.82	16.41	±3.03
eplr	-35.27	±0.90	-39.06	±0.57	-68.39	±1.86
fcri	-50.10	±1.75	-31.59	±0.75	-78.34	±3.17
fcro	-31.05	±0.37	9.54	±0.78	15.51	±1.06
fcrr	-45.92	±0.78	-27.71	±1.05	-67.71	±1.45
fcui	-48.95	±3.11	-43.16	±2.72	-68.07	±4.39
fcuo	-26.09	±4.17	11.84	±3.48	25.98	±3.10
fcur	-45.14	±4.58	-38.09	±1.93	-57.72	±2.05
fdpi1	-62.10	±1.30	-40.14	±0.94	-89.95	±0.57
fdpi2	-68.42	±1.49	-48.01	±1.36	-97.31	±1.20
fdpi3	-65.95	±1.96	-51.83	±0.61	-96.89	±0.78
fdpi4	-66.69	±1.55	-55.03	±0.83	-91.52	±0.70
fdpi5	-68.31	±1.68	-55.24	±1.34	-86.08	±0.77
fdpo	-30.15	±2.09	4.33	±2.25	15.60	±2.02
fdpr	-45.60	±2.20	-35.41	±2.99	-62.95	±2.76
fdsi	-66.58	±1.04	-56.28	±0.98	-93.72	±1.37
fdso	-48.64	±0.84	-29.74	±0.68	-59.62	±1.96
fl	10.11	±1.16	-103.64	±1.19	-93.18	±0.84
flmcp	-59.18	±2.30	-60.98	±0.98	-87.58	±1.92
fm	-77.74	±0.65	-48.06	±1.00	-100.56	±0.52
fmmcp	-59.77	±0.76	-49.61	±0.45	-104.30	±1.93
ftb	-48.86	±0.87	-29.67	±0.54	-78.91	±1.66
hgt	29.66	±0.37	90.21	±0.42	27.55	±0.89
hle	-9.71	±0.37	4.22	±0.97	16.84	±0.58
hme	-30.66	±0.30	12.65	±0.68	15.06	±0.80
ifi	28.54	±0.41	78.87	±0.42	29.08	±0.76
ifo	9.99	±0.57	77.55	±2.20	106.85	±0.70
ma	46.81	±0.21	64.71	±0.64	83.49	±0.51
mb	45.36	±0.40	64.34	±0.34	103.88	±0.29
mc	38.68	±0.29	35.11	±0.22	18.86	±0.23
md	41.37	±0.19	43.98	±0.24	37.37	±0.12
me	-10.94	±0.16	-32.48	±0.26	11.05	±0.12
mf	-3.39	±0.23	-24.76	±0.70	-5.82	±0.24
mg	0.40	±0.26	-31.02	±0.18	-59.48	±0.07
mh	-10.59	±0.16	-47.16	±0.27	-63.10	±0.12
mi	-68.99	±0.87	-82.91	±0.32	-69.89	±0.99
mj	-48.75	±0.50	-81.44	±0.32	-70.16	±0.24
pli1	-61.55	±1.89	-40.73	±1.12	-91.01	±1.85
pli2	-67.86	±1.71	-47.48	±0.97	-97.80	±1.32
pli3	-65.11	±1.84	-51.41	±1.25	-95.77	±0.88
pli4	-65.25	±1.79	-54.22	±1.47	-91.58	±0.94
pli5	-67.61	±1.50	-54.64	±1.78	-86.26	±1.06
plo	-29.39	±2.79	10.20	±1.49	18.50	±3.42
plr	-49.42	±2.33	-31.65	±2.58	-66.50	±4.64

Table A.5 continued

pti	-26.76	±1.87	-8.83	±0.74	-30.35	±0.95
pto	-27.67	±2.24	13.41	±1.33	18.23	±2.13
rh	-11.97	±0.43	-1.08	±0.95	10.31	±1.46
rsp	-41.51	±0.92	-22.92	±0.67	-71.55	±1.05
rus	-32.41	±1.19	-31.64	±0.33	-61.63	±2.24
rusp	-22.51	±0.59	-0.24	±1.29	2.64	±0.95
sa	32.36	±1.09	82.68	±1.54	37.86	±0.89
sca	5.40	±1.15	63.63	±0.21	101.62	±0.62
sdi	17.81	±2.16	61.45	±3.34	17.92	±3.03
sdo	26.14	±0.71	84.45	±1.26	75.86	±3.05
si	-24.42	±0.43	-4.48	±0.40	-17.79	±0.57
so	-11.95	±0.75	-2.54	±1.42	10.77	±0.81
ssci	10.06	±1.32	86.91	±2.90	29.01	±3.40
ssco	6.90	±1.18	86.63	±1.75	103.59	±1.57
ssi	27.61	±1.15	90.78	±2.00	23.66	±1.82
sso	15.45	±0.63	104.62	±1.93	99.89	±2.46
svs	14.44	±0.76	107.39	±0.46	97.93	±0.72
tji	10.29	±0.32	68.71	±0.89	14.75	±0.52
tjo	2.99	±0.42	69.32	±2.33	84.95	±4.61
tlati	-20.99	±1.00	0.36	±1.85	25.06	±2.42
tlato	20.22	±1.06	69.74	±4.19	33.43	±7.92
tlongi	-22.41	±1.21	10.13	±2.71	32.96	±0.84
tlongo	17.99	±0.31	80.09	±0.68	52.11	±0.62
tmedi	-25.54	±2.35	14.44	±3.01	20.64	±2.67
tmedo	6.69	±7.88	57.69	±7.87	20.64	±3.92
tni	27.56	±0.54	76.63	±0.39	29.01	±1.23
tno	14.88	±0.46	76.22	±0.80	69.76	±1.44
uop	-21.98	±0.70	11.36	±0.24	31.59	±0.36
usp	-40.53	±1.08	-43.52	±0.86	-64.22	±1.14

Table A.6 Digitization data for all specimens. Cat 6

	X (mm)		Y (mm)		Z (mm)	
adi	12.85	±1.23	-14.64	±1.21	-15.45	±0.47
ado	28.25	±0.76	28.73	±0.85	-52.00	±2.39
al	-41.81	±0.84	29.39	±0.64	-105.55	±0.97
am	50.47	±0.57	-21.59	±0.84	-103.84	±1.09
anci	-12.99	±0.87	-48.19	±1.74	-4.90	±9.39
anco	9.15	±2.13	-22.81	±3.92	-24.35	±2.34
apli	22.79	±1.01	-17.31	±1.07	96.44	±1.84
aplo	-1.61	±1.08	-33.18	±1.32	52.49	±2.63
aplr	17.00	±0.61	-13.82	±0.82	85.16	±1.28
bbi	0.23	±0.52	-42.96	±1.69	8.85	±1.30
bbo	42.25	±2.63	22.48	±2.95	-44.79	±3.89
bl	-32.77	±0.68	51.83	±1.58	-40.53	±0.61

Table A.6 continued

bm	60.16	±0.78	3.32	±0.97	-32.93	±1.04
brdi	15.99	±3.17	-13.66	±2.81	89.24	±4.82
brdo	17.60	±2.79	-5.43	±5.32	-31.68	±3.24
bri	0.02	±1.92	-37.35	±2.54	3.18	±2.97
bro	24.70	±0.90	17.30	±1.29	-40.18	±2.87
cl	-70.43	±0.58	-22.95	±2.09	-13.75	±0.67
cm	20.31	±1.51	-71.63	±1.01	-6.40	±1.66
dl	-28.22	±2.17	-53.51	±2.19	125.05	±1.31
dm	34.64	±1.01	0.08	±1.30	122.16	±1.66
eci	-0.19	±4.23	-57.34	±1.41	-8.45	±1.49
eco	28.50	±4.33	-12.31	±1.14	-52.77	±2.43
ecrbi	9.97	±2.10	-10.99	±0.93	100.72	±1.30
ecrbr	11.46	±1.28	-11.27	±1.08	87.61	±2.93
ecrli	16.23	±2.66	-11.06	±2.24	100.05	±2.30
ecrlo	-1.07	±0.43	-31.43	±1.07	-16.93	±0.79
ecrlr	11.87	±2.25	-11.41	±1.25	86.84	±4.00
ecro	-6.07	±1.16	-38.51	±0.47	-7.17	±1.16
ecui	1.60	±1.19	-20.22	±0.93	103.47	±2.23
ecuo	-13.60	±1.32	-45.52	±1.79	-6.10	±5.43
ecur	-2.19	±1.33	-22.08	±1.35	91.59	±2.70
edci2	17.59	±1.66	-6.40	±1.04	122.99	±6.80
edci3	10.65	±1.19	-7.66	±1.23	122.66	±7.07
edci4	4.88	±1.04	-13.07	±0.99	122.18	±5.86
edci5	2.30	±0.82	-18.72	±1.25	122.13	±4.92
edco	-7.45	±1.05	-38.47	±0.51	-10.32	±1.06
edcr	6.54	±1.32	-12.36	±1.25	90.32	±4.90
edlati2	17.68	±2.27	-6.34	±1.02	122.95	±6.80
edlati3	10.57	±1.09	-7.84	±1.23	122.47	±6.95
edlati4	4.59	±1.10	-13.25	±0.96	122.14	±6.01
edlati5	2.33	±0.90	-18.69	±1.16	122.05	±4.93
edlato	-12.04	±1.55	-40.51	±1.51	-9.12	±2.90
edlatr	1.58	±1.54	-17.22	±1.28	92.64	±6.21
el	53.33	±2.05	33.58	±1.62	35.81	±1.36
epli1	23.82	±2.03	-12.90	±0.98	109.06	±2.66
epli2	17.81	±2.15	-9.95	±0.86	123.43	±3.70
eplo	-11.22	±0.78	-51.75	±0.94	-1.12	±2.06
eplr	6.54	±1.20	-18.23	±0.57	94.45	±3.02
fcri	17.12	±2.24	-20.50	±0.94	92.64	±6.59
fcro	2.25	±1.01	-50.65	±2.32	-2.68	±3.27
fcrr	14.88	±0.76	-22.28	±0.68	86.32	±2.78
fcui	8.53	±3.68	-29.37	±0.79	93.83	±1.31
fcuo	-6.81	±5.04	-57.95	±0.58	-6.95	±3.26
fcur	9.40	±4.41	-29.78	±0.94	90.13	±1.60
fdpi1	24.45	±2.53	-19.35	±0.97	111.62	±4.13
fdpi2	22.41	±2.61	-19.65	±2.07	118.60	±4.16
fdpi3	17.96	±2.65	-20.14	±1.01	120.54	±3.91

Table A.6 continued

fdpi4	13.78	±2.56	-22.22	±0.87	120.80	±3.25
fdpi5	9.55	±2.95	-25.70	±1.25	120.49	±3.28
fdpo	0.57	±4.07	-52.99	±0.86	-5.46	±1.83
fdpr	14.18	±3.05	-25.18	±1.24	87.43	±3.01
fdsi1	25.22	±2.13	-18.34	±0.64	111.16	±1.21
fdsi2	23.83	±1.94	-17.84	±0.76	120.72	±3.74
fdsi3	19.29	±1.39	-19.96	±0.85	121.91	±2.53
fdsi4	14.28	±1.88	-22.48	±0.61	121.34	±2.18
fdsi5	10.22	±2.50	-25.83	±0.70	122.36	±2.92
fdso	13.27	±1.84	-29.76	±0.52	80.24	±1.07
fdsr	13.91	±1.91	-25.28	±0.78	97.25	±1.12
fl	-39.49	±1.26	16.85	±1.50	124.95	±0.54
flmcp	5.16	±0.57	-25.22	±0.91	123.31	±0.47
fmmcp	22.55	±0.57	-8.52	±1.60	121.66	±1.41
ftb	20.46	±0.47	-20.22	±1.05	98.38	±1.29
gl	-28.18	±0.22	57.74	±0.56	-107.30	±1.64
gm	64.79	±0.53	4.47	±0.73	-101.20	±1.05
hgt	37.89	±1.92	29.50	±1.06	-47.69	±1.79
hle	-9.99	±0.91	-41.92	±1.06	-4.97	±2.19
hme	8.51	±0.41	-53.25	±0.95	-1.58	±0.75
ifi	29.35	±1.39	25.70	±1.88	-49.98	±0.57
ifo	15.98	±1.08	-3.53	±1.78	-121.30	±1.93
ma	-4.11	±1.07	23.41	±0.63	-99.29	±0.85
mb	-12.40	±0.19	7.28	±0.26	-89.91	±0.72
mc	5.99	±0.40	45.50	±0.43	-47.64	±0.38
md	3.80	±0.14	43.76	±0.34	-27.75	±0.30
me	-35.68	±0.49	-29.61	±0.51	-2.52	±0.40
mf	-43.34	±0.39	-48.26	±0.13	1.57	±0.35
mg	35.50	±0.20	-2.69	±0.21	42.62	±0.47
mh	36.73	±0.42	5.31	±1.29	60.71	±0.33
mi	-21.18	±0.37	-29.58	±0.35	130.68	±0.29
mj	-8.04	±0.89	-43.85	±0.77	136.31	±0.90
pli1	25.12	±2.33	-17.57	±0.96	109.82	±1.07
pli2	24.87	±1.38	-16.66	±0.73	122.23	±1.36
pli3	19.78	±2.12	-19.19	±0.69	122.75	±0.59
pli4	14.99	±2.03	-21.67	±0.85	122.70	±1.07
pli5	11.03	±2.12	-25.73	±0.79	122.52	±2.56
plo	1.89	±2.12	-54.57	±0.68	-6.53	±1.61
plr	16.81	±1.61	-23.64	±0.64	93.32	±1.37
pti	5.16	±1.66	-27.12	±2.55	42.49	±4.78
pto	6.89	±2.80	-49.92	±1.31	-5.23	±2.92
rh	-6.55	±1.04	-39.02	±0.40	2.62	±1.23
rsp	6.78	±0.60	-15.62	±0.77	89.74	±1.74
rus	3.34	±0.43	-20.70	±0.32	85.70	±0.87
rusp	-0.08	±0.23	-44.19	±0.77	13.95	±1.90
sa	28.11	±1.04	27.41	±0.94	-55.31	±1.82
sca	12.01	±1.67	-20.61	±1.72	-110.44	±3.15

Table A.6 continued

sdi	22.51	±0.62	11.84	±0.88	-28.07	±1.34
sdo	17.70	±0.82	18.74	±0.93	-77.93	±4.49
si	2.40	±0.29	-33.07	±1.45	31.83	±0.36
so	-9.21	±1.75	-39.76	±1.13	0.58	±3.22
ssci	46.61	±2.26	14.63	±3.36	-46.97	±3.42
ssco	27.16	±2.78	3.29	±2.93	-123.11	±2.41
ssi	40.91	±1.35	31.21	±0.37	-41.39	±1.27
sso	32.87	±0.34	24.45	±0.72	-120.00	±1.07
svs	39.19	±1.34	28.91	±2.12	-114.85	±1.90
tji	34.07	±0.41	7.65	±1.07	-35.64	±0.73
tjo	9.92	±0.31	-20.38	±0.95	-108.07	±1.37
tlati	-13.16	±1.31	-49.73	±1.65	-14.05	±1.70
tlato	28.76	±1.80	12.97	±1.47	-48.68	±1.44
tlongi	-10.08	±4.04	-54.76	±2.56	-15.62	±4.65
tlongo	29.48	±2.03	8.95	±2.84	-62.81	±2.31
tmedi	-2.24	±2.16	-53.06	±2.61	-13.30	±2.18
tmedo	30.02	±2.52	8.61	±2.18	-43.59	±5.85
tni	27.06	±1.18	22.55	±2.85	-45.79	±1.04
tno	24.38	±0.46	7.57	±0.42	-69.75	±0.90
uop	-5.39	±0.57	-59.64	±1.34	-16.74	±0.55
usp	1.34	±0.65	-23.61	±0.88	92.12	±1.37

Table A.7 Digitization data for all specimens. Cat 7

	X (mm)		Y (mm)		Z (mm)	
adi	10.41	±2.29	2.03	±2.16	-34.36	±1.54
ado	17.42	±1.05	20.04	±0.52	-78.63	±1.27
al	-40.88	±1.69	17.85	±1.80	-127.31	±3.02
am	49.70	±1.96	-32.01	±2.25	-110.29	±3.19
anci	-11.88	±0.51	-34.69	±2.17	-4.97	±4.15
anco	2.60	±1.07	-14.89	±1.47	-33.94	±2.44
apli	15.00	±1.79	-1.94	±1.04	89.13	±2.99
aplo	-11.71	±0.73	-23.66	±1.26	28.99	±0.72
aplr	6.34	±1.29	-0.59	±0.76	76.27	±0.83
bbi	-2.55	±2.18	-29.59	±1.28	6.85	±1.41
bbo	30.00	±1.57	15.65	±2.01	-68.36	±3.23
bl	-33.79	±2.37	19.18	±2.36	-46.78	±2.18
bm	61.95	±2.41	-28.87	±2.23	-32.17	±3.22
brdi	6.48	±1.21	2.16	±0.99	80.61	±1.48
brdo	4.42	±0.70	-1.30	±0.90	-38.82	±0.87
bri	-5.53	±2.22	-33.01	±9.72	3.85	±4.58
bro	10.11	±1.89	10.04	±4.05	-56.78	±6.60
cbi	9.21	±1.35	-10.01	±2.17	-36.98	±2.67
cbo	30.20	±2.57	13.62	±3.06	-70.22	±2.53
cl	-56.41	±2.24	1.81	±4.19	8.31	±1.80

Table A.7 continued

cm	28.61	±1.05	-56.18	±2.11	22.36	±1.53
dl	-14.50	±2.38	-33.43	±1.41	111.96	±1.58
dm	40.15	±2.13	31.79	±2.29	106.53	±4.21
ecrbi	4.30	±1.57	1.20	±0.84	96.89	±1.33
ecrbr	3.17	±1.38	2.19	±0.86	83.68	±2.06
ecrli	8.74	±1.40	2.89	±0.80	96.55	±1.29
ecrlr	3.14	±1.32	2.15	±0.81	83.80	±1.23
ecro	-2.46	±1.21	-20.06	±1.31	-23.21	±2.05
ecui	-1.40	±1.24	-9.90	±1.45	94.97	±1.91
ecuo	-11.64	±1.54	-35.35	±1.97	-0.76	±4.60
ecur	-4.25	±1.40	-11.42	±1.61	87.22	±1.17
edci2	10.65	±2.44	3.83	±1.17	108.68	±3.73
edci3	6.17	±1.42	1.37	±1.11	109.16	±3.20
edci4	2.97	±1.01	-2.78	±1.12	108.83	±3.07
edci5	1.00	±1.12	-7.62	±1.57	108.53	±3.29
edco	-10.18	±1.25	-27.40	±1.30	-13.19	±1.22
edcr	-0.14	±1.72	-0.82	±1.14	83.80	±3.16
edlati2	9.00	±2.91	2.96	±1.46	105.89	±4.71
edlati3	5.22	±1.90	0.70	±1.57	106.57	±4.48
edlati4	2.27	±1.27	-3.41	±1.09	106.31	±4.34
edlati5	0.65	±1.33	-7.34	±1.24	106.26	±4.26
edlato	-12.84	±1.05	-29.61	±2.20	-6.83	±1.64
edlatr	-2.32	±1.17	-6.24	±1.68	86.77	±1.92
em	51.23	±0.37	-12.45	±0.50	61.74	±1.03
epli	1.99	±1.32	-1.88	±1.22	89.89	±0.57
eplo	-15.67	±0.34	-46.02	±0.84	0.46	±0.94
eplr	-1.20	±1.07	-6.21	±1.82	84.07	±1.19
fcri	12.64	±3.33	-4.54	±2.67	88.54	±2.16
fcro	6.27	±3.29	-36.19	±1.45	0.54	±1.11
fcrr	10.61	±3.30	-6.39	±2.39	83.72	±1.89
fcui	3.05	±2.07	-15.32	±0.40	90.03	±1.04
fcuo	-4.11	±2.09	-44.73	±1.79	-9.34	±4.12
fcur	0.94	±1.06	-17.07	±0.97	80.18	±1.50
fdpi1	19.21	±2.83	-6.82	±1.18	103.79	±1.68
fdpi2	16.69	±2.63	-5.30	±2.14	112.95	±2.82
fdpi3	13.86	±3.05	-9.28	±1.84	111.41	±1.15
fdpi4	10.59	±2.52	-10.91	±2.22	113.43	±2.58
fdpi5	7.45	±2.49	-13.10	±1.18	112.52	±1.43
fdpo	1.00	±4.59	-39.53	±1.37	-4.97	±2.03
fdpr	8.32	±2.87	-10.10	±1.38	85.49	±5.35
fdsi2	18.20	±0.41	-5.41	±1.23	113.91	±1.46
fdsi3	14.46	±0.72	-9.87	±1.17	113.21	±2.99
fdsi4	11.44	±0.98	-12.60	±0.55	114.25	±0.70
fdsi5	7.55	±1.48	-14.32	±0.04	113.26	±0.95
fdso	8.11	±0.58	-14.25	±0.74	78.46	±2.54
fdsr	8.44	±2.04	-12.19	±1.28	87.10	±2.42

Table A.7 continued

fl	-39.79	±1.50	32.09	±2.26	124.52	±2.25
flmcp	2.90	±0.74	-14.18	±0.67	120.46	±1.27
fm	23.26	±1.03	-12.85	±1.89	113.29	±2.17
fmmcp	18.47	±0.80	2.48	±0.65	120.68	±1.64
ftb	14.29	±0.57	-5.51	±0.93	93.35	±1.15
gl	-29.65	±3.01	38.93	±2.71	-123.35	±2.10
gm	59.41	±0.95	-5.93	±2.02	-95.57	±3.04
hgt	19.13	±1.02	25.05	±0.19	-73.50	±0.65
hle	-10.28	±0.34	-23.34	±0.69	-6.61	±0.38
hme	6.16	±0.15	-32.88	±1.03	-7.55	±0.56
ifi	17.89	±1.44	18.43	±1.82	-70.82	±1.47
ifo	11.78	±0.82	-16.21	±2.18	-137.96	±1.96
ma	-22.21	±0.54	9.10	±0.76	-140.27	±0.47
mb	-20.05	±0.67	23.76	±0.69	-122.10	±2.88
mc	-7.08	±0.94	25.60	±0.64	-45.05	±2.06
md	-16.48	±0.90	11.10	±1.49	-28.32	±2.06
me	-31.28	±0.45	-2.15	±0.88	-1.48	±0.69
mf	-31.47	±0.74	-0.41	±0.95	18.43	±0.87
mg	32.76	±0.99	-9.87	±0.93	45.66	±1.02
mh	35.15	±0.74	9.50	±1.05	59.84	±1.16
mi	-13.01	±0.58	-19.76	±1.43	90.46	±1.47
mj	-22.54	±0.56	-10.32	±0.56	113.98	±1.29
pli1	19.98	±1.67	-7.56	±0.59	105.23	±1.01
pli2	18.72	±1.28	-5.45	±0.84	113.59	±2.47
pli3	14.75	±0.35	-9.68	±1.16	113.05	±2.96
pli4	12.09	±1.21	-12.67	±1.17	114.66	±1.05
pli5	8.00	±1.48	-14.45	±0.37	113.57	±0.87
plo	0.82	±1.66	-41.14	±0.69	-7.46	±2.34
plr	9.34	±0.77	-11.27	±1.76	81.00	±1.35
pti	0.98	±1.64	-16.09	±1.61	34.78	±5.52
pto	5.58	±1.97	-37.09	±2.25	-6.22	±2.21
rh	-5.12	±1.76	-21.03	±0.59	3.58	±1.25
rsp	9.53	±0.92	0.01	±0.69	81.67	±0.71
rus	-0.23	±0.98	-9.10	±0.63	80.04	±2.64
rusp	-2.56	±0.51	-25.03	±1.19	9.23	±3.19
sa	14.25	±0.41	21.80	±0.34	-85.43	±1.04
sca	6.33	±0.48	-29.78	±0.67	-129.51	±0.86
sdi	4.52	±0.57	1.49	±0.44	-58.12	±3.06
sdo	10.48	±0.85	9.18	±1.13	-103.65	±3.39
si	-18.02	±0.58	-36.46	±0.94	-1.40	±0.67
so	-6.07	±0.90	-18.37	±1.05	34.46	±0.58
ssci	29.32	±2.81	6.30	±1.47	-70.68	±2.45
ssco	24.16	±3.58	-7.33	±4.03	-136.62	±1.56
ssi	28.36	±2.46	22.08	±1.43	-66.60	±4.17
sso	28.24	±2.45	8.32	±4.38	-134.59	±4.45

Table A.7 continued

svs	41.75	±0.36	6.09	±0.39	-128.13	±0.61
tji	19.44	±0.31	5.74	±0.62	-54.02	±0.46
tjo	9.83	±3.20	-27.16	±3.40	-116.70	±6.63
tlati	-9.84	±0.85	-40.69	±1.67	-5.10	±2.10
tlato	14.97	±0.51	11.41	±0.39	-64.43	±0.68
tlongi	-8.17	±1.24	-45.18	±0.90	-11.85	±2.82
tlongo	16.94	±0.51	4.35	±1.75	-85.83	±1.15
tmedi	-1.66	±1.35	-41.39	±3.14	-10.98	±1.43
tmedo	12.42	±0.20	12.49	±1.04	-62.82	±1.12
tni	15.59	±1.14	15.79	±2.24	-67.66	±1.24
tno	13.92	±0.36	-6.85	±0.30	-104.27	±0.63
uop	-5.07	±0.22	-34.61	±0.93	-17.24	±0.59
usp	0.47	±0.74	-16.18	±0.96	87.87	±1.02

APPENDIX B

Table B.1: Length Feedback Gains

	tlong	tmed	tlat	anc	BB	BR	BCD	ECRL	ECRB	EDC	EIP	EDL	ECU	SUP	APL
tlong	6.9	1.9	0.4	0.6	0	0	0	0	0	0	0	0	0	0	0
tmed	2.2	4.9	1.9	0.9	0	0	0	0	0	0	0	0	0	0	0
tlat	1.7	1.6	2.1	0.7	0	0	0	0	0	0	0	0	0	0	0
anc	0	0	0	0	0	0	0	0	0	0	0	0	0	0	0
BB	0	0	0	0	3.9	1.7	0.3	0.3	0.2	0.1	0	0	0	0	0
BR	0	0	0	0	1	4.7	1.3	1	0.4	0.7	0	0	0	0	0
BCD	0	0	0	0	0.6	2.1	3.6	0.8	0.5	0.7	0	0	0	0	0
ECRL	0	0	0	0	1	0.9	0.4	1.9	2.7	0	0	0	0	0	0
ECRB	0	0	0	0	0.7	0.5	0.2	1.6	5.4	0.4	0	0	0	0	0
EDC	0	0	0	0	0	0	0	0	0.7	3.4	0.9	0.6	0.2	0	0
EIP	0	0	0	0	0	0	0	0	0.3	1.1	0.4	2.4	0	0	0.2
EDL	0	0	0	0	0	0	0	0	0	0.7	2.7	0	0.9	0	0
ECU	0.9	0.6	0.2	0.3	0	0	0	0	0	0	0.3	0	4.8	0	0
SUP	0.1	0.1	0.1	0.2	0.5	0.1	0	0.1	0.1	0	0	0	0	4.3	0.5
APL	0	0	0	0	0.1	0	0	0	0	0	0	0.3	0	0.1	3

	PQ	fdp5	fdp1	fdp3	fdp2m	fdp2u	fdp4	PL	FCUU	FCUH	FCR
PQ	1.9	0	0.1	0	0	0.1	0	0	0	0	0
fdp5	0.1	2.6	2.1	0.5	0.7	1.4	1.5	0	0	0	0
fdp1	0.2	1.4	3.7	0.7	0.7	1.4	0.8	0	0	0	0
fdp3	0	0.8	0.9	1.4	0.5	1	2	0.1	0	0	0.1
fdp2m	0	1.3	1	0.7	0.9	1.6	0.8	0.1	0	0	0
fdp2u	0	0.9	2.4	0.6	0.7	2.1	1.2	0.3	0	0	0.1
fdp2	0	1.1	1.7	0.65	0.8	1.85	1	0.2	0	0	0.05
fdp4	0	0.5	0.3	0.7	0.1	0.3	2.9	0.2	0	0	0.4
PL	0	0.1	0.1	0.1	0.1	0.2	0.5	2.3	0.1	0.3	0.5
FCUU	0	0	0.1	0	0	0	0	0.3	2.8	1.4	0
FCUH	0	0	0	0	0.1	0	0	0.5	1	4.3	0.2
FCU	0	0	0.05	0	0.05	0	0	0.4	1.9	2.85	0.1
FCR	0	0.1	0	0	0	0	0.1	0.1	0	0.3	3.5

	BI	BR	BRD	ECRL	ECRB	PRT	PQ	FP5	FCR	APL	TLA+AN	TLO+TM
PRT	0.4	0.4	0.3	0.3	0.9	4.8	1.4	0	0.5	0	0	0
PQ	0	0	0	0	0	2.4	3.7	0.2	0.2	0	0	0
FCR	0	0	0	0	0	0.1	0	0	4.1	0.8	0.3	1

APPENDIX C

C.1 Introduction

Part of our objective was also to develop a mathematical model of the cat forelimb that would correctly predicted all the essential features observed in our experiment. These features would include (i) appropriate direction of the stiffness ellipse; (ii) agreement in terms of force direction and presence or absence of force magnitude asymmetry; and (iii) accurate pattern of force constraint, or lack thereof.

C.2 Modeling

The model platform, Neuromechanic, is a simulated physical environment designed to analyze and test the control of biomechanical systems. Neuromechanic employs rigid body equations of motion, various muscles models, and multilayer neural networks, to determine, among other parameters of interest, muscle and joint states, and system stability. The platform is an on-going developmental project being implemented by Dr. Nate Bunderson, a post-doctoral fellow, in our research laboratory, and Jeff Bingham, a collaborating graduate student.

The musculotendon complex was designed using a variation of a Hill model (Zajac 1989), composed of an inelastic tendon in series with a muscle fiber. The muscle fiber has a parallel arrangement of a contractile and elastic element. The force produced by an individual muscle can be represented by the function

$$F^m(t) = \cos\varphi \, (\, a(t)F_a(\dot{l})F_a(l) + F_p(l) + \, \eta \frac{\dot{l}}{v_0^m}) \, F_o^m,$$

where $F^m(t)$ is the muscle-fiber force, φ the pennation angle, $a(t)$ the muscle activation, $F_a(\dot{l})$ the normalized active velocity-dependent fiber force, $F_a(l)$ normalized active length-dependent fiber force, $F_p(l)$ the normalized passive length-dependent fiber force, η the passive damping coefficient, $\dot{l}$ the fiber shortening velocity, v_0^m the maximum shortening velocity, and F_o^m the maximum isometric muscle-fiber force. Thus, the model makes use of the force-length and force-velocity relationships and the activation dynamics to estimate the force generated by each muscle.

The physiological data used in these parameters were obtained by various methods. The whole limb was reconstructed using 3-D kinematic motion data, as well as anatomical data such as muscle origin, insertion and via points, and skeletal reference points. Parameters such as muscle mass, muscle length and pennation angle were directly measured from cadaver dissections. Fiber length and sarcomere length were used to derive attributes such as the optimal fiber length and the physiological cross-sectional area (PCSA) [61], from which maximum contractile force could be calculated [150]. The active force-length, passive force-length, and active force-velocity curves [55, 57, 58] were modeling by interpolated splines. The model was further calibrated using experimentally obtained moment arms. These moment arms, which vary with angle, were calculated as the ratio of tendon excursion to the joint angle, both obtained using the tendon displacement method [100].

In summary, Neuromechanic was employed to construct a model composed of 5 rigid-body segments, with 6 degrees of freedom (3 at the shoulder, 1 at the elbow, 1 between the radius and ulna, and 1 at the wrist), and 29 muscles. The muscles were positioned according to their attachment points, and their properties (mass, optimal fiber

length, pennation angle, etc.), were incorporated. The scapula was fixed and the model limb was given the same perturbations at the paw as those applied to the experimental limb and the resulting endpoint forces compared. This procedure allowed us to determine the stiffness properties of the limb, as well as evaluate the model's predictive capacity and effectiveness as a mathematical representation of the cat forelimb.

C.3 Results

The perturbation protocol was performed in a computational model of the forelimb, the results of which are shown in Figure C.1. Similar to the experiments an asymmetric force magnitude response was produced with a high shape index of 26.47 when the limb was in the extended position. However, the model forelimb produced greater forces in the negative direction, or when the limb is being compressed, as in the experimental crouched posture condition. The force direction plot was similar to that of the force constraint model. In the crouched position the asymmetry is similar to the experimental case, with greater force magnitude when the limb is compressed. However, the shape index is considerably lower (4.37) than the extended condition and the force direction profile is suggestive of the ellipsoid model, as opposed to the force constraint in experiments.

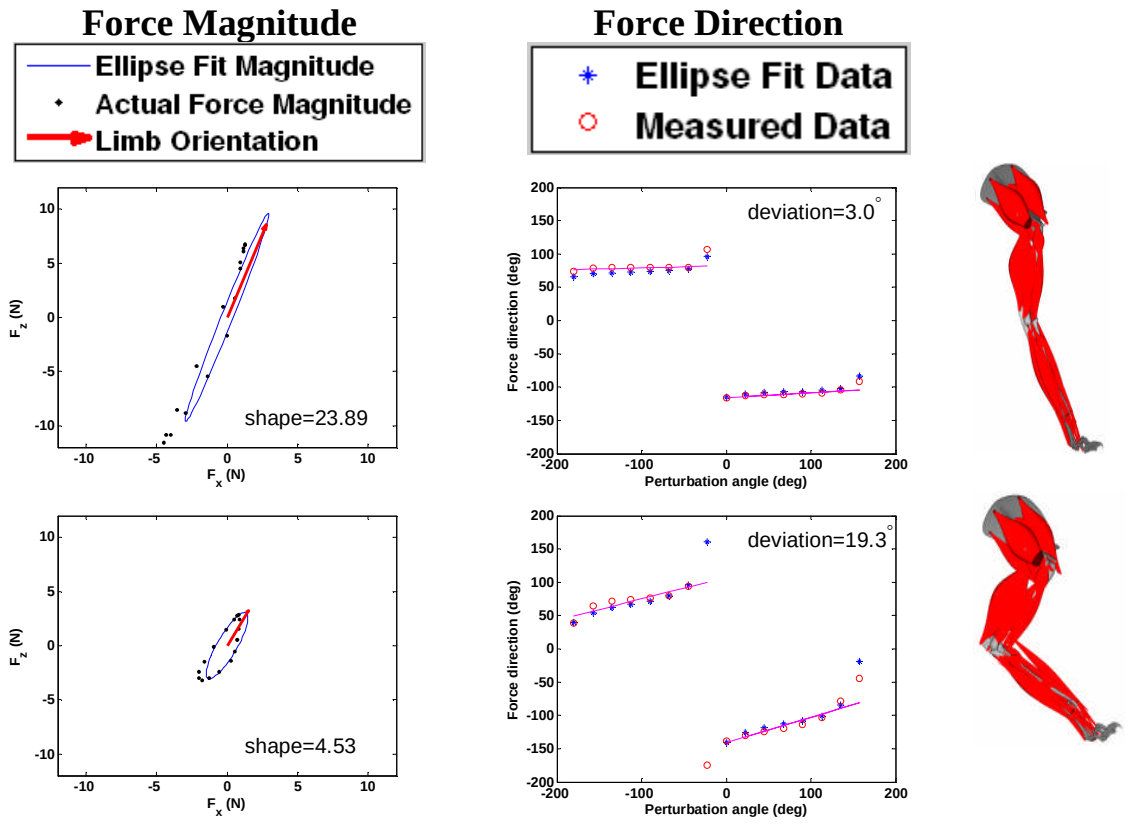

Figure C.1. Forelimb Sagittal Plane Model Force Results. Force field response of the forelimb of the musculoskeletal model is shown, as well as its separate magnitude and direction components, in extended (top) and crouched (bottom) positions.

The hindlimb model (Figure C.2) displays greater force magnitude under compression in both the extended and crouched positions. The shape index is greater in the extended position (8.34 vs. 5.14) but still much lower than that of the forelimb extended condition. The direction profiles of both hindlimb conditions indicate an ellipsoid strategy.

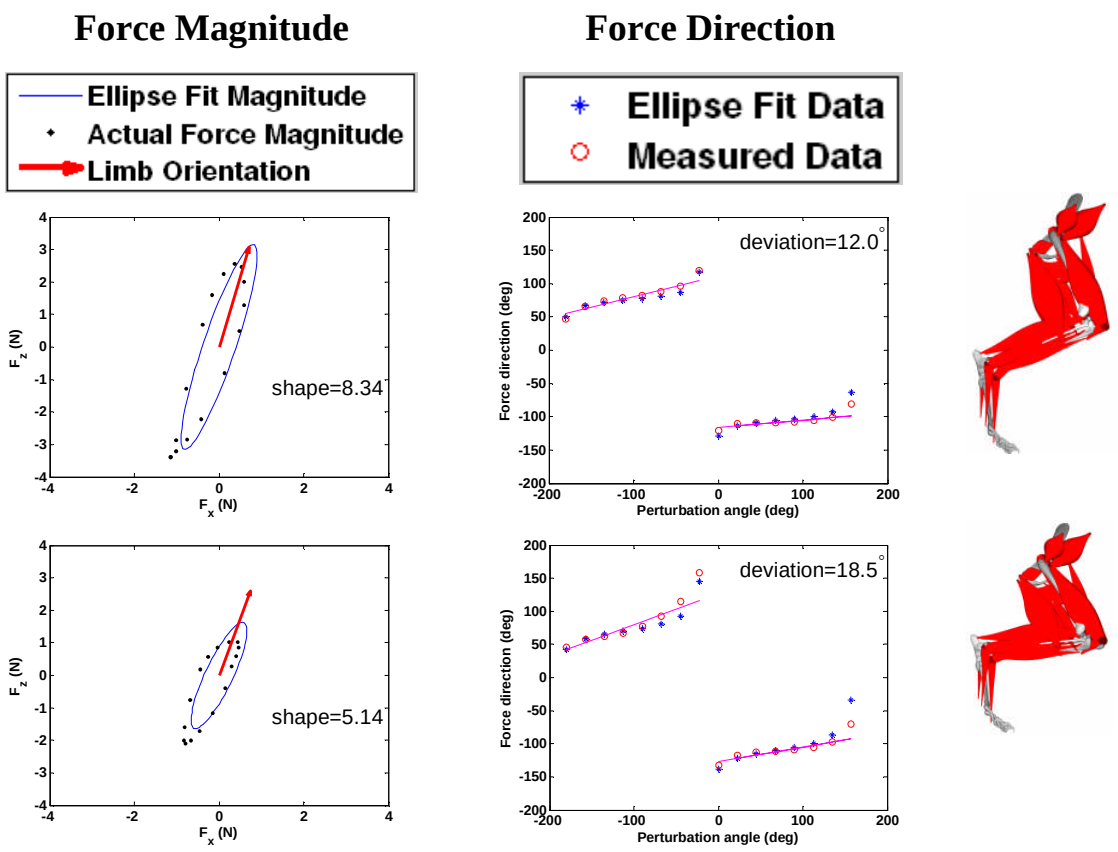

Figure C.2. Hindlimb Sagittal Plane Model Force Results. Force field response of the hindlimb of the musculoskeletal model is shown, as well as its separate magnitude and direction components, in extended (top) and crouched (bottom) positions.

The forelimb model exhibited a high shape index stiffness ellipse during the extended position as in experiments, but the direction of force magnitude asymmetry was reversed. In the crouched position the direction of force magnitude asymmetry was in agreement with experiment but the shape index was much lower and the force direction showed a higher deviation.

The computational model produced force fields that opposed the direction of disturbance, with the greatest response corresponding to the main limb axis from

endpoint to scapula. Stiffness ellipses were also produced from the computational model data and were found to also capture the direction properties as in experiments. In all cases the model exhibited the asymmetric force response to perturbation seen in experiments.

The model differed from the experimental results in a couple of ways. The first was that the strategy predicted by the model for forelimb behavior changed from force constraint model during extended stance to the ellipsoid model during crouched stance. The experiments indicated that the forelimb employed the force constraint strategy in both cases, and only employed the force constraint during the passive crouched regime. Mussa-Ivaldi et al. [30] also noted that the magnitude and shape of their models changed much more than those of their subjects as the arm position changed. Those authors suggested that their models may not have incorporated some aspect of neural input or muscle properties. However, since our experiments revealed that the same behavior is observed irrespective of neural input, the latter explanation is more likely. Our Hill muscle model, which is an approximation, may not possess the necessary attribute that produces a slower change as the limb shifts to positions closer to the trunk. The model shows proof of principle but still needs to undergo a sensitivity analysis.

REFERENCES

[1] T. C. Collatos, V. R. Edgerton, J. L. Smith, and B. R. Botterman, "Contractile properties and fiber type compositions of flexors and extensors of elbow joint in cat: implications for motor control," *J Neurophysiol,* vol. 40, pp. 1292-300, Nov 1977.

[2] T. Drew, J. Kalaska, and N. Krouchev, "Muscle synergies during locomotion in the cat: a model for motor cortex control," *J Physiol,* vol. 586, pp. 1239-45, Mar 1 2008.

[3] N. Fritz and C. Schmidt, "Contractile properties of single motor units in two multi-tendoned muscles of the cat distal forelimb," *Exp Brain Res,* vol. 88, pp. 401-10, 1992.

[4] C. F. Honeycutt and T. R. Nichols, "The decerebrate cat generates the essential features of the force constraint strategy," *J Neurophysiol,* vol. 103, pp. 3266-73, Jun 2010.

[5] M. Illert, "Monosynaptic Ia pathways and motor behaviour of the cat distal forelimb," *Acta Neurobiol Exp (Wars),* vol. 56, pp. 423-34, 1996.

[6] N. Krouchev, J. F. Kalaska, and T. Drew, "Sequential activation of muscle synergies during locomotion in the intact cat as revealed by cluster analysis and direct decomposition," *J Neurophysiol,* vol. 96, pp. 1991-2010, 2006.

[7] F. Lacquaniti and C. Maioli, "Independent control of limb position and contact forces in cat posture," *J Neurophysiol,* vol. 72, pp. 1476-95, Oct 1994.

[8] J. M. Macpherson, "Strategies that simplify the control of quadrupedal stance. II. Electromyographic activity," *J Neurophysiol,* vol. 60, pp. 218-31, 1988.

[9] J. M. Macpherson, "Strategies that simplify the control of quadrupedal stance. I. Forces at the ground," *J Neurophysiol,* vol. 60, pp. 204-17, 1988.

[10] J. H. Martin, S. E. Cooper, and C. Ghez, "Kinematic analysis of reaching in the cat," *Exp Brain Res,* vol. 102, pp. 379-92, 1995.

[11] N. Harischandra, J. M. Cabelguen, and O. Ekeberg, "A 3D Musculo-Mechanical Model of the Salamander for the Study of Different Gaits and Modes of Locomotion," *Front Neurorobot,* vol. 4, p. 112, 2010.

[12] M. Raibert, K. Blankespoor, G. Nelson, and R. Playter. (2008, 23 Aug). *BigDog, the Rough-Terrain Quadruped Robot*. Available: http://www.bostondynamics.com/img/BigDog_IFAC_Apr-8-2008.pdf

[13] J. L. McKay and L. H. Ting, "Optimization of muscle activity for task-level goals predicts complex changes in limb forces across biomechanical contexts," *PLoS Comput Biol,* vol. 8, p. e1002465, 2012.

[14] J. M. Macpherson, "Changes in a postural strategy with inter-paw distance," *J Neurophysiol,* vol. 71, pp. 931-940, 1994.

[15] A. G. Caicoya, M. Illert, and R. Janike, "Monosynaptic Ia pathways at the cat shoulder," *J Physiol,* vol. 518 (Pt 3), pp. 825-41, Aug 1 1999.

[16] V. Dietz, "Human neuronal control of automatic functional movements: interaction between central programs and afferent input," *Physiol Rev,* vol. 72, pp. 33-69, Jan 1992.

[17] A. Nardone, A. Giordano, T. Corra, and M. Schieppati, "Responses of leg muscles in humans displaced while standing. Effects of types of perturbation and of postural set," *Brain,* vol. 113 (Pt 1), pp. 65-84, Feb 1990.
[18] L. M. Nashner, "Adapting reflexes controlling the human posture," *Exp Brain Res,* vol. 26, pp. 59-72, Aug 27 1976.
[19] L. M. Nashner, F. O. Black, and C. Wall, 3rd, "Adaptation to altered support and visual conditions during stance: patients with vestibular deficits," *J Neurosci,* vol. 2, pp. 536-44, May 1982.
[20] R. J. Peterka, "Sensorimotor integration in human postural control," *J Neurophysiol,* vol. 88, pp. 1097-118, Sep 2002.
[21] A. L. Adkin, S. Quant, B. E. Maki, and W. E. McIlroy, "Cortical responses associated with predictable and unpredictable compensatory balance reactions," *Experimental Brain Research,* vol. 172, pp. 85-93, Jun 2006.
[22] J. V. Jacobs and F. B. Horak, "Cortical control of postural responses," *J Neural Transm,* vol. 114, pp. 1339-48, 2007.
[23] W. Taube, M. Schubert, M. Gruber, S. Beck, M. Faist, and A. Gollhofer, "Direct corticospinal pathways contribute to neuromuscular control of perturbed stance," *J Appl Physiol,* vol. 101, pp. 420-9, Aug 2006.
[24] T. R. Nichols, T. C. Cope, and T. A. Abelew, "Rapid spinal mechanisms of motor coordination," *Exerc Sport Sci Rev,* vol. 27, pp. 255-84, 1999.
[25] T. J. Burkholder and T. R. Nichols, "The mechanical action of proprioceptive length feedback in a model of cat hindlimb," *Motor Control,* vol. 4, pp. 201-20, Apr 2000.
[26] T. J. Burkholder and T. R. Nichols, "Three-dimensional model of the feline hindlimb," *J Morphol,* vol. 261, pp. 118-29, 2004.
[27] S. L. Delp and J. P. Loan, "A graphics-based software system to develop and analyze models of musculoskeletal structures," *Comput Biol Med,* vol. 25, pp. 21-34, Jan 1995.
[28] W. J. Kargo and L. C. Rome, "Functional morphology of proximal hindlimb muscles in the frog Rana pipiens," *J Exp Biol,* vol. 205, pp. 1987-2004, Jul 2002.
[29] N. Hogan, "The mechanics of multi-joint posture and movement control," *Biol Cybern,* vol. 52, pp. 315-31, 1985.
[30] F. A. Mussa-Ivaldi, N. Hogan, and E. Bizzi, "Neural, mechanical, and geometric factors subserving arm posture in humans," *J Neurosci,* vol. 5, pp. 2732-43, Oct 1985.
[31] A. V. Hill, "The Heat of Shortening and the Dynamic Constants of Muscle," *Proceedings of the Royal Society of London. Series B, Biological Sciences,* vol. 126, pp. 136-195, 1938.
[32] A. F. Huxley, "Muscular contraction," *J Physiol,* vol. 243, pp. 1-43, Nov 1974.
[33] A. F. Huxley and R. M. Simmons, "Mechanical properties of the cross-bridges of frog striated muscle," *J Physiol,* vol. 218 Suppl, pp. 59P-60P, Oct 1971.
[34] S. P. Ma, *Activation Dynamics for the Distribution-moment Model of Muscle*: Washington University, 1988. Department of Mechanical Engineering., 1988.
[35] J. M. Macpherson, D. S. Rushmer, and D. C. Dunbar, "Postural responses in the cat to unexpected rotations of the supporting surface: evidence for a centrally generated synergic organization," *Exp Brain Res,* vol. 62, pp. 152-60, 1986.

[36] J. M. Macpherson and J. T. Inglis, "Stance and balance following bilateral labyrinthectomy," *Prog Brain Res,* vol. 97, pp. 219-28, 1993.
[37] F. B. Horak, L. M. Nashner, and H. C. Diener, "Postural strategies associated with somatosensory and vestibular loss," *Exp Brain Res,* vol. 82, pp. 167-77, 1990.
[38] L. Nashner and A. Berthoz, "Visual contribution to rapid motor responses during postural control," *Brain Res,* vol. 150, pp. 403-7, Jul 14 1978.
[39] A. Iggo and K. H. Andres, "Morphology of cutaneous receptors," *Annu Rev Neurosci,* vol. 5, pp. 1-31, 1982.
[40] D. C. Dunbar, F. B. Horak, J. M. Macpherson, and D. S. Rushmer, "Neural control of quadrupedal and bipedal stance: implications for the evolution of erect posture," *Am J Phys Anthropol,* vol. 69, pp. 93-105, Jan 1986.
[41] L. H. Ting and J. M. Macpherson, "Ratio of shear to load ground-reaction force may underlie the directional tuning of the automatic postural response to rotation and translation," *J Neurophysiol,* vol. 92, pp. 808-23, Aug 2004.
[42] C. F. Honeycutt and T. R. Nichols, "Disruption of cutaneous feedback alters magnitude but not direction of muscle responses to postural perturbations in the decerebrate cat," *Exp Brain Res,* vol. 203, pp. 765-71, Jun 2010.
[43] A. Prochazka, "Proprioceptive Feedback and Movement Regulation," in *Comprehensive Physiology,* ed: John Wiley & Sons, Inc., 2010.
[44] P. B. Matthews, "Muscle Spindles and Their Motor Control," *Physiol Rev,* vol. 44, pp. 219-88, Apr 1964.
[45] C. F. Honeycutt, P. Nardelli, T. C. Cope, and T. R. Nichols, "Muscle spindle responses to horizontal support surface perturbation in the anesthetized cat: insights into the role of autogenic feedback in whole body postural control," *J Neurophysiol,* vol. 108, pp. 1253-61, Sep 2012.
[46] L. Jami, "Golgi tendon organs in mammalian skeletal muscle: functional properties and central actions," *Physiol Rev,* vol. 72, pp. 623-66, Jul 1992.
[47] P. E. Crago, J. C. Houk, and W. Z. Rymer, "Sampling of total muscle force by tendon organs," *J Neurophysiol,* vol. 47, pp. 1069-83, Jun 1982.
[48] J. Houk and E. Henneman, "Responses of Golgi tendon organs to active contractions of the soleus muscle of the cat," *J Neurophysiol,* vol. 30, pp. 466-81, May 1967.
[49] P. J. Stapley, L. H. Ting, M. Hulliger, and J. M. Macpherson, "Automatic postural responses are delayed by pyridoxine-induced somatosensory loss," *J Neurosci,* vol. 22, pp. 5803-7, Jul 15 2002.
[50] J. T. Inglis, F. B. Horak, C. L. Shupert, and C. Jones-Rycewicz, "The importance of somatosensory information in triggering and scaling automatic postural responses in humans," *Exp Brain Res,* vol. 101, pp. 159-64, 1994.
[51] T. R. Nichols and J. C. Houk, "Improvement in linearity and regulation of stiffness that results from actions of stretch reflex," *J Neurophysiol,* vol. 39, pp. 119-42, Jan 1976.
[52] E. J. Perreault, R. F. Kirsch, and P. E. Crago, "Voluntary control of static endpoint stiffness during force regulation tasks," *J Neurophysiol,* vol. 87, pp. 2808-16, Jun 2002.
[53] E. R. Kandel, J. H. Schwartz, and T. M. Jessell, *Principles of neural science,* 4th ed. New York: McGraw-Hill, Health Professions Division, 2000.

[54] A. V. Hill, "The mechanics of active muscle," *Proc R Soc Lond B Biol Sci,* vol. 141, pp. 104-17, Mar 11 1953.
[55] A. M. Gordon, A. F. Huxley, and F. J. Julian, "The variation in isometric tension with sarcomere length in vertebrate muscle fibres," *J Physiol,* vol. 184, pp. 170-92, May 1966.
[56] P. A. Huijing, "Important experimental factors for skeletal muscle modelling: non-linear changes of muscle length force characteristics as a function of degree of activity," *Eur J Morphol,* vol. 34, pp. 47-54, 1996.
[57] F. E. Zajac, "Muscle and tendon: properties, models, scaling, and application to biomechanics and motor control," *Crit Rev Biomed Eng,* vol. 17, pp. 359-411, 1989.
[58] G. C. Joyce, P. M. Rack, and D. R. Westbury, "The mechanical properties of cat soleus muscle during controlled lengthening and shortening movements," *J Physiol,* vol. 204, pp. 461-74, Oct 1969.
[59] J. M. Ritchie and D. R. Wilkie, "The effect of previous stimulation on the active state of muscle," *J Physiol,* vol. 130, pp. 488-96, Nov 28 1955.
[60] T. J. Burkholder, B. Fingado, S. Baron, and R. L. Lieber, "Relationship between muscle fiber types and sizes and muscle architectural properties in the mouse hindlimb," *J Morphol,* vol. 221, pp. 177-90, Aug 1994.
[61] R. D. Sacks and R. R. Roy, "Architecture of the hind limb muscles of cats: functional significance," *J Morphol,* vol. 173, pp. 185-95, Aug 1982.
[62] E. Henneman and C. B. Olson, "Relations between Structure and Function in the Design of Skeletal Muscles," *J Neurophysiol,* vol. 28, pp. 581-98, May 1965.
[63] T. J. Roberts, M. S. Chen, and C. R. Taylor, "Energetics of bipedal running. II. Limb design and running mechanics," *J Exp Biol,* vol. 201, pp. 2753-62, Oct 1998.
[64] T. S. Buchanan, D. G. Lloyd, K. Manal, and T. F. Besier, "Estimation of muscle forces and joint moments using a forward-inverse dynamics model," *Med Sci Sports Exerc,* vol. 37, pp. 1911-6, Nov 2005.
[65] G. K. Cole, A. J. van den Bogert, W. Herzog, and K. G. Gerritsen, "Modelling of force production in skeletal muscle undergoing stretch," *J Biomech,* vol. 29, pp. 1091-104, Aug 1996.
[66] J. J. Woods and B. Bigland-Ritchie, "Linear and non-linear surface EMG/force relationships in human muscles. An anatomical/functional argument for the existence of both," *Am J Phys Med,* vol. 62, pp. 287-99, Dec 1983.
[67] G. E. Goslow, Jr., H. J. Seeherman, C. R. Taylor, M. N. McCutchin, and N. C. Heglund, "Electrical activity and relative length changes of dog limb muscles as a function of speed and gait," *J Exp Biol,* vol. 94, pp. 15-42, Oct 1981.
[68] S. B. Williams, A. M. Wilson, J. Daynes, K. Peckham, and R. C. Payne, "Functional anatomy and muscle moment arms of the thoracic limb of an elite sprinting athlete: the racing greyhound (Canis familiaris)," *J Anat,* vol. 213, pp. 373-82, Oct 2008.
[69] S. B. Williams, A. M. Wilson, and R. C. Payne, "Functional specialisation of the thoracic limb of the hare (Lepus europeus)," *J Anat,* vol. 210, pp. 491-505, Apr 2007.

[70] N. A. Brown, M. G. Pandy, C. E. Kawcak, and C. W. McIlwraith, "Force- and moment-generating capacities of muscles in the distal forelimb of the horse," *J Anat,* vol. 203, pp. 101-13, Jul 2003.

[71] M. T. Butcher, J. W. Hermanson, N. G. Ducharme, L. M. Mitchell, L. V. Soderholm, and J. E. Bertram, "Contractile behavior of the forelimb digital flexors during steady-state locomotion in horses (Equus caballus): an initial test of muscle architectural hypotheses about in vivo function," *Comp Biochem Physiol A Mol Integr Physiol,* vol. 152, pp. 100-14, Jan 2009.

[72] J. W. Hermanson and K. J. Hurley, "Architectural and histochemical analysis of the biceps brachii muscle of the horse," *Acta Anat (Basel),* vol. 137, pp. 146-56, 1990.

[73] J. M. Ryan, M. A. Cobb, and J. W. Hermanson, "Elbow extensor muscles of the horse: postural and dynamic implications," *Acta Anat (Basel),* vol. 144, pp. 71-9, 1992.

[74] R. Heine, K. Manal, and T. S. Buchanan, "Using Hill-Type Muscle Models and Emg Data in a Forward Dynamic Analysis of Joint Moment: Evaluation of Critical Parameters," *Journal of Mechanics in Medicine and Biology,* vol. 3, pp. 169-186, Jun 2003.

[75] S. L. Delp and J. P. Loan, "A computational framework for simulating and analyzing human and animal movement," *Computing in Science & Engineering,* vol. 2, pp. 46-55, 2000.

[76] T. R. Nichols, K. I. Murinas, C. M. J. I. Huyghues-Despointes, and T. J. Burkholder, "Transformation of muscular action into endpoint forces in the hindlimb of the decerebrate cat," *Proceedings of the 25th Annual International Conference of the Ieee Engineering in Medicine and Biology Society, Vols 1-4,* vol. 25, pp. 3834-3836, 2003.

[77] N. E. Bunderson, J. L. McKay, L. H. Ting, and T. J. Burkholder, "Directional constraint of endpoint force emerges from hindlimb anatomy," *J Exp Biol,* vol. 213, pp. 2131-41, Jun 15 2010.

[78] C. F. Honeycutt, J. S. Gottschall, and T. R. Nichols, "Electromyographic responses from the hindlimb muscles of the decerebrate cat to horizontal support surface perturbations," *J Neurophysiol,* vol. 101, pp. 2751-61, Jun 2009.

[79] C. Honeycutt, P. Nardelli, T. Cope, and T. Nichols, "Autogenic spindle pathways mediate the postural response during horizontal support surface perturbations," *Soc Neurosci Abstr,* vol. 410, p. 16, 2007.

[80] A. W. English, "An electromyographic analysis of forelimb muscles during overground stepping in the cat," *J Exp Biol,* vol. 76, pp. 105-22, Oct 1978.

[81] W. J. Gonyea, "Functional implications of felid forelimb anatomy," *Acta Anat (Basel),* vol. 102, pp. 111-21, 1978.

[82] M. Schmidt and M. S. Fischer, "Morphological integration in mammalian limb proportions: dissociation between function and development," *Evolution,* vol. 63, pp. 749-66, Mar 2009.

[83] D. S. Rushmer, C. J. Russell, J. Macpherson, J. O. Phillips, and D. C. Dunbar, "Automatic postural responses in the cat: responses to headward and tailward translation," *Experimental Brain Research,* vol. 50, pp. 45-61, 1983.

[84] F. Lacquaniti and C. Maioli, "Independent control of limb position and contact forces in cat posture," *Journal of Neurophysiology,* vol. 72, pp. 1476-95, Oct 1994.

[85] D. S. Rushmer, C. J. Russell, J. macpherson, J. O. Phillips, and D. C. Dunbar, "Automatic postural responses in the cat: responses to headward and tailward translation," *Exp Brain Res,* vol. 50, pp. 45-61, 1983.

[86] H. W. Merkens, H. C. Schamhardt, G. J. Van Osch, and A. J. Van den Bogert, "Ground reaction force patterns of Dutch warmblood horses at normal trot," *Equine veterinary journal,* vol. 25, pp. 134-7, 1993.

[87] P. F. Rumph, J. E. Lander, S. A. Kincaid, D. K. Baird, J. R. Kammermann, and D. M. Visco, "Ground reaction force profiles from force platform gait analyses of clinically normal mesomorphic dogs at the trot," *American journal of veterinary research,* vol. 55, pp. 756-61, 1994.

[88] B. Demes, K. J. Carlson, and T. M. Franz, "Cutting corners: the dynamics of turning behaviors in two primate species," *J Exp Biol,* vol. 209, pp. 927-37, Mar 2006.

[89] D. L. Jindrich and R. J. Full, "Many-legged maneuverability: dynamics of turning in hexapods," *J Exp Biol,* vol. 202 (Pt 12), pp. 1603-23, Jun 1999.

[90] L. C. Rome and A. A. Sosnicki, "Myofilament overlap in swimming carp. II. Sarcomere length changes during swimming," *Am J Physiol,* vol. 260, pp. C289-96, Feb 1991.

[91] C. Gans and W. J. Bock, "The functional significance of muscle architecture--a theoretical analysis," *Ergebnisse der Anatomie und Entwicklungsgeschichte,* vol. 38, pp. 115-42, 1965.

[92] S. A. Spector, P. F. Gardiner, R. F. Zernicke, R. R. Roy, and V. R. Edgerton, "Muscle architecture and force-velocity characteristics of cat soleus and medial gastrocnemius: implications for motor control," *J Neurophysiol,* vol. 44, pp. 951-60, Nov 1980.

[93] T. M. Winters, M. Takahashi, R. L. Lieber, and S. R. Ward, "Whole muscle length-tension relationships are accurately modeled as scaled sarcomeres in rabbit hindlimb muscles," *J Biomech,* vol. 44, pp. 109-15, Jan 4 2011.

[94] A. A. Sosnicki, K. E. Loesser, and L. C. Rome, "Myofilament overlap in swimming carp. I. Myofilament lengths of red and white muscle," *Am J Physiol,* vol. 260, pp. C283-8, Feb 1991.

[95] G. J. Lutz and L. C. Rome, "Built for jumping: the design of the frog muscular system," *Science,* vol. 263, pp. 370-2, Jan 21 1994.

[96] M. J. Myers and K. Steudel, "Effect of limb mass and its distribution on the energetic cost of running," *J Exp Biol,* vol. 116, pp. 363-73, May 1985.

[97] Y. Yeh, R. J. Baskin, R. L. Lieber, and K. P. Roos, "Theory of light diffraction by single skeletal muscle fibers," *Biophysical journal,* vol. 29, pp. 509-22, 1980.

[98] J. Mendez and A. Keys, "Density and composition of mammalian muscle," *Metabolism,* vol. 9, pp. 184-188, 1960.

[99] T. J. Burkholder and R. L. Lieber, "Sarcomere length operating range of vertebrate muscles during movement," *J Exp Biol,* vol. 204, pp. 1529-36, May 2001.

[100] K. N. An, Y. Ueba, E. Y. Chao, W. P. Cooney, and R. L. Linscheid, "Tendon excursion and moment arm of index finger muscles," *J Biomech,* vol. 16, pp. 419-25, 1983.
[101] G. J. Loren, S. D. Shoemaker, T. J. Burkholder, M. D. Jacobson, J. Friden, and R. L. Lieber, "Human wrist motors: biomechanical design and application to tendon transfers," *J Biomech,* vol. 29, pp. 331-42, Mar 1996.
[102] T. J. Burkholder and R. L. Lieber, "Stepwise regression is an alternative to splines for fitting noisy data," *J Biomech,* vol. 29, pp. 235-8, Feb 1996.
[103] J. E. Crouch, *Text-atlas of cat anatomy*. Philadelphia,: Lea & Febiger, 1969.
[104] B. G. Wilder, *Anatomical technology as applied to the domestic cat, an introduction to human, veterinary, and comparative anatomy, with illustrations*. New York,: Barnes, 1882.
[105] R. P. Young, S. H. Scott, and G. E. Loeb, "An intrinsic mechanism to stabilize posture--joint-angle-dependent moment arms of the feline ankle muscles," *Neurosci Lett,* vol. 145, pp. 137-40, Oct 12 1992.
[106] P. E. Hudson, S. A. Corr, R. C. Payne-Davis, S. N. Clancy, E. Lane, and A. M. Wilson, "Functional anatomy of the cheetah (Acinonyx jubatus) forelimb," *Journal of Anatomy,* vol. 218, pp. 375-385, Apr 2011.
[107] S. Yakovenko, N. Krouchev, and T. Drew, "Sequential Activation of Motor Cortical Neurons Contributes to Intralimb Coordination During Reaching in the Cat by Modulating Muscle Synergies," *Journal of Neurophysiology,* vol. 105, pp. 388-409, Jan 2011.
[108] S. G. McLean, A. Su, and A. J. van den Bogert, "Development and validation of a 3-D model to predict knee joint loading during dynamic movement," *J Biomech Eng,* vol. 125, pp. 864-74, Dec 2003.
[109] F. J. Valero-Cuevas, H. Hoffmann, M. U. Kurse, J. J. Kutch, and E. A. Theodorou, "Computational Models for Neuromuscular Function," *IEEE Rev Biomed Eng,* vol. 2, pp. 110-135, 2009.
[110] F. E. Zajac, R. R. Neptune, and S. A. Kautz, "Biomechanics and muscle coordination of human walking: part II: lessons from dynamical simulations and clinical implications," *Gait Posture,* vol. 17, pp. 1-17, Feb 2003.
[111] W. L. Buford, Jr. and D. E. Thompson, "A system for three-dimensional interactive simulation of hand biomechanics," *IEEE Trans Biomed Eng,* vol. 34, pp. 444-53, Jun 1987.
[112] J. M. Macpherson and J. Fung, "Weight support and balance during perturbed stance in the chronic spinal cat," *J Neurophysiol,* vol. 82, pp. 3066-81, Dec 1999.
[113] L. W. Tsai, *Robot Analysis: The Mechanics of Serial and Parallel Manipulators*: Wiley, 1999.
[114] G. T. Yamaguchi, *Dynamic Modeling of Musculoskeletal Motion: A Vectorized Approach for Biomechanical Analysis in Three Dimensions*: Springer, 2005.
[115] C. W. Spoor and F. E. Veldpaus, "Rigid body motion calculated from spatial co-ordinates of markers," *J Biomech,* vol. 13, pp. 391-3, 1980.
[116] F. E. Veldpaus, H. J. Woltring, and L. J. Dortmans, "A least-squares algorithm for the equiform transformation from spatial marker co-ordinates," *J Biomech,* vol. 21, pp. 45-54, 1988.

[117] R. M. Ehrig, W. R. Taylor, G. N. Duda, and M. O. Heller, "A survey of formal methods for determining functional joint axes," *J Biomech,* vol. 40, pp. 2150-7, 2007.
[118] E. Todorov, "Probabilistic inference of multijoint movements, skeletal parameters and marker attachments from diverse motion capture data," *IEEE Trans Biomed Eng,* vol. 54, pp. 1927-39, Nov 2007.
[119] H. J. Woltring, R. Huiskes, A. de Lange, and F. E. Veldpaus, "Finite centroid and helical axis estimation from noisy landmark measurements in the study of human joint kinematics," *J Biomech,* vol. 18, pp. 379-89, 1985.
[120] K. Halvorsen, M. Lesser, and A. Lundberg, "A new method for estimating the axis of rotation and the center of rotation," *J Biomech,* vol. 32, pp. 1221-7, Nov 1999.
[121] M. M. Panjabi, "Centers and angles of rotation of body joints: a study of errors and optimization," *J Biomech,* vol. 12, pp. 911-20, 1979.
[122] G. Lukács, A. D. Marshall, and R. R. Martin, "Geometric least-squares fitting of spheres, cylinders, cones and tori," 1997.
[123] N. E. Bunderson, J. T. Bingham, M. H. Sohn, L. H. Ting, and T. J. Burkholder, "Neuromechanic: a computational platform for simulation and analysis of the neural control of movement," *Int j numer method biomed eng,* vol. 28, pp. 1015-27, Oct 2012.
[124] T. L. Hill, E. Eisenberg, Y. D. Chen, and R. J. Podolsky, "Some self-consistent two-state sliding filament models of muscle contraction," *Biophys J,* vol. 15, pp. 335-72, Apr 1975.
[125] A. F. Huxley, "Muscle structure and theories of contraction," *Prog Biophys Biophys Chem,* vol. 7, pp. 255-318, 1957.
[126] H. E. Huxley, "Past, present and future experiments on muscle," *Philos Trans R Soc Lond B Biol Sci,* vol. 355, pp. 539-43, Apr 29 2000.
[127] H. E. Huxley, "The contraction of muscle," *Sci Am,* vol. 199, pp. 67-72 passim, Nov 1958.
[128] G. I. Zahalak, "A comparison of the mechanical behavior of the cat soleus muscle with a distribution-moment model," *J Biomech Eng,* vol. 108, pp. 131-40, May 1986.
[129] G. I. Zahalak, "The two-state cross-bridge model of muscle is an asymptotic limit of multi-state models," *J Theor Biol,* vol. 204, pp. 67-82, May 7 2000.
[130] C. J. Barclay, "A weakly coupled version of the Huxley crossbridge model can simulate energetics of amphibian and mammalian skeletal muscle," *J Muscle Res Cell Motil,* vol. 20, pp. 163-76, Feb 1999.
[131] M. G. Pandy, "Computer modeling and simulation of human movement," *Annu Rev Biomed Eng,* vol. 3, pp. 245-73, 2001.
[132] M. G. Pandy, B. A. Garner, and F. C. Anderson, "Optimal control of non-ballistic muscular movements: a constraint-based performance criterion for rising from a chair," *J Biomech Eng,* vol. 117, pp. 15-26, Feb 1995.
[133] L. J. Bhargava, M. G. Pandy, and F. C. Anderson, "A phenomenological model for estimating metabolic energy consumption in muscle contraction," *J Biomech,* vol. 37, pp. 81-8, Jan 2004.

[134] W. Herzog, "History dependence of skeletal muscle force production: implications for movement control," *Hum Mov Sci,* vol. 23, pp. 591-604, Nov 2004.
[135] O. Rohrle, J. B. Davidson, and A. J. Pullan, "A physiologically based, multi-scale model of skeletal muscle structure and function," *Front Physiol,* vol. 3, p. 358, 2012.
[136] K. A. Edman, "Mechanism underlying double-hyperbolic force-velocity relation in vertebrate skeletal muscle," *Adv Exp Med Biol,* vol. 332, pp. 667-76; discussion 676-8, 1993.
[137] S. P. Ma and G. I. Zahalak, "A distribution-moment model of energetics in skeletal muscle," *J Biomech,* vol. 24, pp. 21-35, 1991.
[138] J. M. Winters and S. L. Y. Woo, *Multiple muscle systems: biomechanics and movement organization*: Springer-Verlag, 1990.
[139] G. M. Odegard, T. L. Donahue, D. A. Morrow, and K. R. Kaufman, "Constitutive modeling of skeletal muscle tissue with an explicit strain-energy function," *J Biomech Eng,* vol. 130, p. 061017, Dec 2008.
[140] L. A. Spyrou and N. Aravas, *Muscle and Tendon Tissues: Constitutive Modeling and Computational Issues*, 2011.
[141] R. J. Bloch and H. Gonzalez-Serratos, "Lateral force transmission across costameres in skeletal muscle," *Exerc Sport Sci Rev,* vol. 31, pp. 73-8, Apr 2003.
[142] H. Maas, G. C. Baan, and P. A. Huijing, "Intermuscular interaction via myofascial force transmission: effects of tibialis anterior and extensor hallucis longus length on force transmission from rat extensor digitorum longus muscle," *J Biomech,* vol. 34, pp. 927-40, Jul 2001.
[143] M. Van Loocke, C. G. Lyons, and C. K. Simms, "A validated model of passive muscle in compression," *J Biomech,* vol. 39, pp. 2999-3009, 2006.
[144] S. S. Blemker and S. L. Delp, "Three-dimensional representation of complex muscle architectures and geometries," *Ann Biomed Eng,* vol. 33, pp. 661-73, May 2005.
[145] M. Van Loocke, C. G. Lyons, and C. K. Simms, "Viscoelastic properties of passive skeletal muscle in compression: stress-relaxation behaviour and constitutive modelling," *J Biomech,* vol. 41, pp. 1555-66, 2008.
[146] G. B. Gillis and A. A. Biewener, "Hindlimb extensor muscle function during jumping and swimming in the toad (Bufo marinus)," *J Exp Biol,* vol. 203, pp. 3547-63, Dec 2000.
[147] J. M. Olson and R. L. Marsh, "Activation patterns and length changes in hindlimb muscles of the bullfrog Rana catesbeiana during jumping," *J Exp Biol,* vol. 201, pp. 2763-77, Oct 1998.
[148] P. Nardinocchi and L. Teresi, "On the active response of soft living tissues," *Journal of Elasticity,* vol. 88, pp. 27-39, Jul 2007.
[149] C. Paetsch, B. A. Trimmer, and A. Dorfmann, "A constitutive model for active–passive transition of muscle fibers," *International Journal of Non-Linear Mechanics,* vol. 47, pp. 377-387, 3// 2012.
[150] A. M. Wilson, M. P. McGuigan, A. Su, and A. J. van Den Bogert, "Horses damp the spring in their step," *Nature,* vol. 414, pp. 895-9, Dec 20-27 2001.

[151] B. I. Prilutsky, M. G. Sirota, R. J. Gregor, and I. N. Beloozerova, "Quantification of motor cortex activity and full-body biomechanics during unconstrained locomotion," *J Neurophysiol*, vol. 94, pp. 2959-69, Oct 2005.
[152] H. J. Ralston, M. J. Polissar, and et al., "Dynamic features of human isolated voluntary muscle in isometric and free contractions," *J Appl Physiol*, vol. 1, pp. 526-33, Jan 1949.
[153] N. Fritz, M. Illert, S. de la Motte, P. Reeh, and P. Saggau, "Pattern of monosynaptic Ia connections in the cat forelimb," *J Physiol*, vol. 419, pp. 321-51, Dec 1989.
[154] A. Boczek-Funcke, J. P. Kuhtz-Buschbeck, and M. Illert, "X-ray kinematic analysis of shoulder movements during target reaching and food taking in the cat," *Eur J Neurosci*, vol. 11, pp. 986-96, Mar 1999.
[155] A. Hollister, W. L. Buford, L. M. Myers, D. J. Giurintano, and A. Novick, "The axes of rotation of the thumb carpometacarpal joint," *J Orthop Res*, vol. 10, pp. 454-60, May 1992.
[156] A. Leardini, L. Chiari, U. Della Croce, and A. Cappozzo, "Human movement analysis using stereophotogrammetry. Part 3. Soft tissue artifact assessment and compensation," *Gait Posture*, vol. 21, pp. 212-25, Feb 2005.
[157] W. R. Taylor, R. M. Ehrig, G. N. Duda, H. Schell, P. Seebeck, and M. O. Heller, "On the influence of soft tissue coverage in the determination of bone kinematics using skin markers," *J Orthop Res*, vol. 23, pp. 726-34, Jul 2005.
[158] A. Niesche, M. Tettke, D. Hochmann, and M. Kraft, "Numerical evaluation and comparison of instantaneous anatomical knee joint axes and orthotic joint axes using MRI data under weight-bearing condition," in *4th European Conference of the International Federation for Medical and Biological Engineering*. vol. 22, J. Sloten, P. Verdonck, M. Nyssen, and J. Haueisen, Eds., ed: Springer Berlin Heidelberg, 2009, pp. 522-525.
[159] A. Van Campen, F. De Groote, L. Bosmans, L. Scheys, I. Jonkers, and J. De Schutter, "Functional knee axis based on isokinetic dynamometry data: Comparison of two methods, MRI validation, and effect on knee joint kinematics," *J Biomech*, vol. 44, pp. 2595-600, Oct 13 2011.
[160] S. M. Henry, J. Fung, and F. B. Horak, "EMG responses to maintain stance during multidirectional surface translations," *J Neurophysiol*, vol. 80, pp. 1939-50, Oct 1998.
[161] J. A. Leonard, R. H. Brown, and P. J. Stapley, "Reaching to multiple targets when standing: the spatial organization of feedforward postural adjustments," *J Neurophysiol*, vol. 101, pp. 2120-33, Apr 2009.
[162] D. G. Lloyd and T. F. Besier, "An EMG-driven musculoskeletal model to estimate muscle forces and knee joint moments in vivo," *J Biomech*, vol. 36, pp. 765-76, Jun 2003.
[163] E. J. Perreault, R. F. Kirsch, and P. E. Crago, "Effects of voluntary force generation on the elastic components of endpoint stiffness," *Exp Brain Res*, vol. 141, pp. 312-23, Dec 2001.
[164] R. D. Trumbower, M. A. Krutky, B. S. Yang, and E. J. Perreault, "Use of self-selected postures to regulate multi-joint stiffness during unconstrained tasks," *PLoS One*, vol. 4, p. e5411, 2009.

[165] X. Hu, W. M. Murray, and E. J. Perreault, "Muscle short-range stiffness can be used to estimate the endpoint stiffness of the human arm," *J Neurophysiol,* vol. 105, pp. 1633-41, Apr 2011.
[166] K. S. Campbell, "Short-range mechanical properties of skeletal and cardiac muscles," *Adv Exp Med Biol,* vol. 682, pp. 223-46, 2010.
[167] R. F. Kirsch, D. Boskov, and W. Z. Rymer, "Muscle stiffness during transient and continuous movements of cat muscle: perturbation characteristics and physiological relevance," *IEEE Trans Biomed Eng,* vol. 41, pp. 758-70, Aug 1994.
[168] J. Fung and J. M. Macpherson, "Attributes of quiet stance in the chronic spinal cat," *J Neurophysiol,* vol. 82, pp. 3056-65, Dec 1999.
[169] J. M. Macpherson, "The force constraint strategy for stance is independent of prior experience," *Exp Brain Res,* vol. 101, pp. 397-405, 1994.
[170] D. C. Lin and W. Z. Rymer, "Mechanical properties of cat soleus muscle elicited by sequential ramp stretches: implications for control of muscle," *J Neurophysiol,* vol. 70, pp. 997-1008, 1993.